교과목 414.519 강의록

수치선박유체역학

- 보텍스 방법 -

COMPUTATIONAL MARINE HYDRODYNAMICS

-VORTEX METHODS-

2019년 6월 27일

Suh, Jung-Chun
서 정 천
Seoul National Univ., Dept. NAOE
서울대학교 공과대학조선해양공학과

8

VORTEX PARTICLE METHODS

8.1 Introduction

This chapter describes a vortex particle method for the solution of the incompressible Navier-Stokes equations. In the early stages of development of flows around a circular cylinder, a hydrofoil section, a sphere and a rectangular wing undergoing an impulsively started motion, the computational results obtained by the vortex particle method (including the vortex-in-cell method) are compared with those obtained by the Eulerian finite volume method. The comparison is performed separately for the pressure fields as well. The results obtained by these methods give a better understanding of the vorticity-based methods.

The vortex method is based on the Lagrangian description of the vorticity field. Its the main idea is one that a vortical flow field is represented by vortex particles. This representation is very attractive for numerical simulations of viscous flow around a body with complex geometry. It is then possible to avoid the nonlinear convection term of the vorticity transport equation, which involves difficulties associated with numerical diffusion for its discretization in grid-based methods.

We will focus on the two-dimensional formulation but partly some extension of the formulation to three-dimensions will be made.

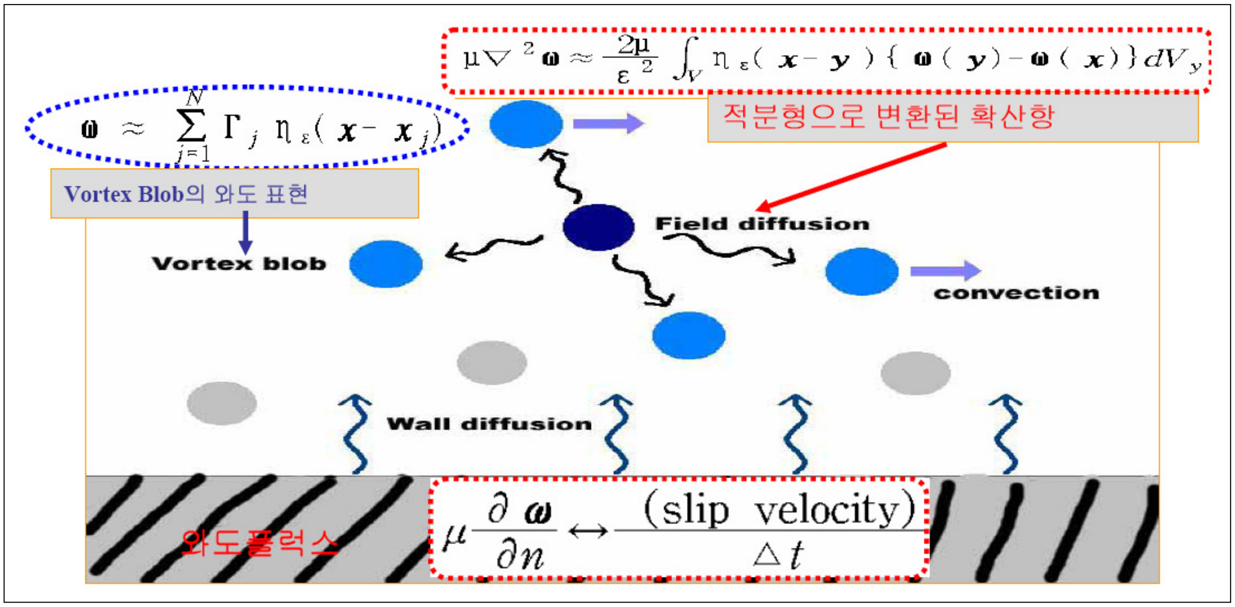

Figure 8.1 Schematic diagram of the vortex particle method in two-dimensions.

8.2 Numerical Implementation

8.2.1 Particle representation of vorticity field

There are several kinds of Lagrangian elements to discretize the vorticity field in vortex methods, such as particles(blobs), sheets, and filaments. In this work, a set of N vortex particles is introduced, of strength $\underline{\alpha}_i$ and position $\underline{x}_i(t)$, to represent the vorticity field

8.2.1.1 Two-dimensions

In the case of two-dimensional flows, a Lagrangian form of Eq. (6.38) is represented as

$$\frac{D\omega}{Dt} = \nu \nabla^2 \omega, \tag{8.1}$$

where ω is the scalar plane component of the vorticity vector ($\underline{\omega} \equiv \omega\,\underline{k}$). The vorticity field is represented by N scalar-valued particles:

$$\omega(\underline{x}, t) = \sum_{i=1}^{N} \zeta_\epsilon(\underline{x} - \underline{x}_i)\, \alpha_i. \tag{8.2}$$

Each particle is characterized by its position, $\underline{x}_i(t)$, and its strength, $\underline{\alpha}_i(t) = \alpha_i(t)\underline{k}$, i.e., its *circulation*, $\alpha_i = \int_{S_i} \omega dS \approx \omega_i S_i$, with S_i the area of fluid associated with the particle *i*. The regularized particle representation of the vorticity field has been used by various researchers (Leonard 1980, Winckelmans 1989,1993). The distribution functions ζ_ϵ associated with each particle are defined by

$$\zeta_\epsilon(\underline{r}) = \frac{1}{{\epsilon_i}^2}\, \zeta\left(\frac{|\underline{r}|}{\epsilon_i}\right), \tag{8.3}$$

where ϵ_i is the smoothing parameter denoting the blob (particle) size which is usually taken as the grid size. In the present study, we choose Gaussian smoothing as the distribution function for its physically appealing properties:

$$\zeta(\rho) = \frac{1}{2\pi} \exp\left(-\frac{\rho^2}{2}\right). \tag{8.4}$$

8.2.1.2 Three-dimensions

In a similar way to two-dimensions, a set of N vortex particles is introduced to represent the vorticity field:

$$\underline{\omega}(\underline{x}, t) = \sum_{i=1}^{N} \zeta_\epsilon(\underline{x} - \underline{x}_i)\, \underline{\alpha}_i, \tag{8.5}$$

where the strength $\underline{\alpha}_i = \int_{V_i} \underline{\omega}\, dV = \underline{\omega}_i V_i$ and V_i is the volume associated with the particle i. The regularization function, ζ_ϵ, associated with each particle is defined by

$$\zeta_\epsilon(\underline{r}) = \frac{1}{\epsilon_i^3}\,\zeta\left(\frac{|\underline{r}|}{\epsilon_i}\right) \tag{8.6}$$

where ϵ_i is the smoothing parameter. The function ζ is usually taken to be radially symmetric with normalization to conserve circulation. The Gaussian distribution can be used, for instance,

$$\zeta(\rho) = \frac{1}{(2\pi)^{3/2}} \exp\left(-\frac{\rho^2}{2}\right) \tag{8.7}$$

8.2.2 Velocity field

In three dimensional flow, Eq. (6.40) is expressed as

$$\underline{q} = \frac{1}{4\pi} \oint_S \left[(\underline{n} \cdot \underline{q}) \frac{\underline{r}}{|\underline{r}|^3} + (\underline{n} \times \underline{q}) \times \frac{\underline{r}}{|\underline{r}|^3} \right] dS + \frac{1}{4\pi} \int_V \underline{\omega} \times \frac{\underline{r}}{|\underline{r}|^3}\, dV, \tag{8.8}$$

where,$\underline{r} = \underline{x} - \underline{y}$. The second integral term of Eq. (8.8) corresponds to the rotational part($\underline{u}_\omega$) of the velocity field induced by the vorticity field.

Vortex particle positions $\underline{x}_i(t)$ are governed by the equation,

$$\frac{d\underline{x}_i}{dt} = \underline{q}(\underline{x}_i, t) \tag{8.9}$$

Recall that the velocity field is based on the Helmholtz decomposition:

$$\underline{q} = \underline{U}_\infty + \nabla\phi + \underline{u}_\omega \tag{8.10}$$

The term $\nabla\phi$ is equivalent to the surface integral of Eq. (6.40) that is the irrotational part of the velocity field. According to Green's scalar identity, the potential ϕ at arbitrary points on the body surface is written as

$$\frac{1}{2}\phi(\underline{x}) = \oint_{S_B} \left\{ \phi(\underline{y})\ \left(\underline{n}(\underline{y}) \cdot \nabla G\right) + \left(\underline{n}(\underline{y}) \cdot \nabla\phi(\underline{y})\right)\ G \right\}\, dl_y. \tag{8.11}$$

The integral equation of Eq. (8.11) is discretized as

$$\frac{1}{2}\phi_i(\underline{x}) = \sum_{j=1}^{M} A_{ij}\,\phi_j + \sum_{j=1}^{M} B_{ij}\,\sigma_j, \tag{8.12}$$

where

$$A_{ij} = \int_{C_j} \underline{n}(\underline{y}) \cdot \nabla G\, dl_y, \qquad B_{ij} = \int_{C_j} G\, dl_y, \tag{8.13}$$

$$\sigma_j \equiv \underline{n} \cdot \nabla \phi_j = \underline{n} \cdot \underline{U}_B - \underline{n} \cdot (\underline{U}_\infty + \underline{u}_\omega)\,. \tag{8.14}$$

By solving the linear system of equations with A_{ij}, B_{ij}, we obtain ϕ_i at collocation points on the surface. Then $\nabla\phi$ on the body surface can be approximated in the sense of the finite difference of ϕ_i. $\nabla\phi$ at field points can be directly computed by using Eq. (3.5) for 3-D and Eq. (3.5) for 2-D.

8.2.2.1 Regularized velocity field

Note that one can view the mollified velocity field as the exact velocity associated with a vorticity $\underline{\omega}$ consisting of vortex particles, in two-dimensions,

$$\begin{aligned}
\underline{u}_\omega &= \int_S \underline{K} \times \left[\sum_{i=1}^{N} \Gamma_i\, \zeta_\epsilon\left(|\underline{x} - \underline{x}_i|\right)\right] dS \\
&= \sum_{i=1}^{N} \left[\int_{S_i} \underline{K}\, \zeta_\epsilon\left(|\underline{x} - \underline{x}_i|\right)\, dS\right] \times \Gamma_i \\
&= \sum_{i=1}^{N} \underline{K}_\epsilon\left(|\underline{x} - \underline{x}_i|\right) \times \Gamma_i
\end{aligned} \tag{8.15}$$

Here, with the smooth function η_ϵ, the kernel $\underline{K}_\epsilon$ in (8.15) is expressed as

$$\begin{aligned}\underline{K}_\epsilon\left(r\right) &= \int_S \underline{K}\left(r\right)\ \zeta_\epsilon(r)\,dS \\ &= \underline{K}(r)\ \int_0^r \int_0^{2\pi}\ \zeta_\epsilon(r)\ r\,dr\,d\theta \\ &= \underline{K}\left(r\right)\left[1-\exp\left(-\frac{r^2}{2\epsilon^2}\right)\right] \qquad (8.16)\end{aligned}$$

where $r = |\underline{x}-\underline{y}|$, $\quad \underline{K} = \nabla G = -\dfrac{1}{2\pi}\dfrac{\underline{r}}{|\underline{r}|^2}$.

$$\underline{K}_\epsilon\left(\underline{x}-\underline{y}\right) = -\frac{1}{2\pi}\frac{\underline{x}-\underline{y}}{|\underline{x}-\underline{y}|^{\ 2}}\left[1-\exp\left(-\frac{|\underline{x}-\underline{y}|^2}{2\epsilon^2}\right)\right] \qquad (8.17)$$

The term $\underline{u}_\omega$ of Eq. (8.10) which is equivalent to the volume integral (Biot-Savart integral) of Eq. (6.40), may be discretized by Eq. (8.2) for 2-D:

$$\underline{u}_\omega(\underline{x},t) = -\frac{1}{2\pi}\sum_{i=1}^{N}\underline{K}_\epsilon \times \left(\alpha_i(\underline{x}_i)\ \underline{k}\right), \quad \text{in 2-D} \qquad (8.18)$$

where

$$\underline{K}_\epsilon = \frac{\underline{r}_i}{|\underline{r}_i|^2}\left[1-\exp\left\{-\underline{r}_i^2/(2\epsilon_i^2)\right\}\right], \quad \text{with} \quad \underline{r}_i = \underline{x}-\underline{x}_i \qquad (8.19)$$

Similarly, the regularized velocity for 3-D can be expressed as:

$$\underline{u}_\omega(\underline{x},t) = -\frac{1}{4\pi}\sum_{i=1}^{N}\underline{K}_\epsilon^{(3D)} \times \underline{\alpha}_i(\underline{x}_i), \quad \text{in 3-D} \qquad (8.20)$$

where

$$\underline{K}_\epsilon^{(3D)} = \frac{\underline{r}_i}{|\underline{r}_i|^3}\left\{\operatorname{erf}\left(\frac{\rho}{\sqrt{2}}\right)-\rho\sqrt{\frac{2}{\pi}}\exp\left(-\frac{\rho^2}{2}\right)\right\}, \quad \rho = |\underline{r}_i|/\epsilon_i \qquad (8.21)$$

where $\mathrm{erf}(x) = \dfrac{2}{\sqrt{\pi}} \displaystyle\int_0^x \exp(-t^2)\, dt$.

The efficiency of vortex particle method is conditioned in particular by the choice of the cutoff function η_ϵ and the location and strength of particles are initially set. The right hand side of Eq. (8.15) is computed using a fast algorithm, proposed by Greengard and Rohklin (1987), that has an operation count of $\mathcal{O}\left(N \log N\right)$ and with active error control based on accurate error bounds. The numerical time-advancing scheme required for solving the location of particles is an additional important factor. In practice it is important to use schemes that are at least second order (Adam-bashforth or Runge-Kutta schemes are commonly used).

Note that the term $\underline{u}_\omega$ has been included when we apply the no-penetration condition $\underline{q} \cdot \underline{n} = \underline{U}_B \cdot \underline{n}$ on the body surface. In fact, the no-penetration condition is numerically imposed by Eq. (8.14).

The vector potential (stream function) corresponding to the 3-D velocity field would be

$$\underline{\psi}(\underline{x}, t) = \frac{1}{4\pi} \sum_{i=1}^{N} \frac{1}{\rho\, \epsilon_i} \mathrm{erf}\left(\frac{\rho}{\sqrt{2}}\right) \underline{\alpha}_i \tag{8.22}$$

A simpler algebraic function can be used rather than such a Gaussian function, especially for the calculation of the stream function at the boundary:

$$\begin{aligned}\underline{\psi}(\underline{x}_B, t) &= \frac{1}{4\pi} \sum_{i=1}^{N} \frac{1}{\epsilon_i} \frac{1}{\sqrt{|\underline{x} - \underline{x}_i|^2/\epsilon_i^2 + 1}} \underline{\alpha}_i \\ &= \frac{1}{4\pi} \sum_{i=1}^{N} \frac{1}{\sqrt{|\underline{x} - \underline{x}_i|^2 + \epsilon_i^2}} \underline{\alpha}_i \end{aligned} \tag{8.23}$$

8.2.3 Field viscous diffusion: PSE scheme

The treatment of the diffusion equation Eq. (8.1) is based on a technique related to the PSE (Particle Strength Exchange) scheme introduced by Degond & Mas-Gallic (1989). The Laplacian operator ∇^2 is approximated by an integral operator, which is discretized over the particles.

$$\nu\nabla^2\omega \approx \frac{2\nu}{\epsilon^2}\int_S \eta_\epsilon(|\underline{x}-\underline{y}|)\,(\omega(\underline{y})-\omega(\underline{x}))\,dS_y. \tag{8.24}$$

Then, the evolution equation for the particle strength becomes

$$\frac{d\alpha_i}{dt} = \frac{2\nu}{\epsilon^2}\sum_{j=1}^{N}(S_i\,\alpha_j - S_j\,\alpha_i)\;\eta_\epsilon(\underline{x}_i-\underline{x}_j), \tag{8.25}$$

where

$$\eta_\epsilon(\underline{x}_i-\underline{x}_j) = \frac{1}{2\pi\,\epsilon^2}\;\exp\left(-\frac{|\underline{x}_i-\underline{x}_j|^2}{2\epsilon^2}\right) \tag{8.26}$$

This function is the same as one given in Eq. (8.4). Herein, ϵ is taken to be constant for all particles.

The three-dimensional version would be

$$\frac{d\underline{\alpha}_i}{dt} = \frac{2\nu}{\epsilon^2}\sum_{j=1}^{N}\left(V_i\,\underline{\alpha}_j - V_j\,\underline{\alpha}_i\right)\;\eta_\epsilon(\underline{x}_i-\underline{x}_j) \tag{8.27}$$

8.2.3.1 Image layer method in two-dimensions

If Eq. (8.25) is used for wall-bounded computations, particles close to the wall are not completely surrounded by other particles. Consequently, a spurious vorticity flux appears at the wall while the total vorticity is conserved (Ploumhans 2000, Cottet 2000).

We use an image particle layer to complete the PSE for particles close to the wall. Solid walls are approximated as discretized panels. The images are placed along a layer inside the body close to the panel, as shown in Figure **8.3** .

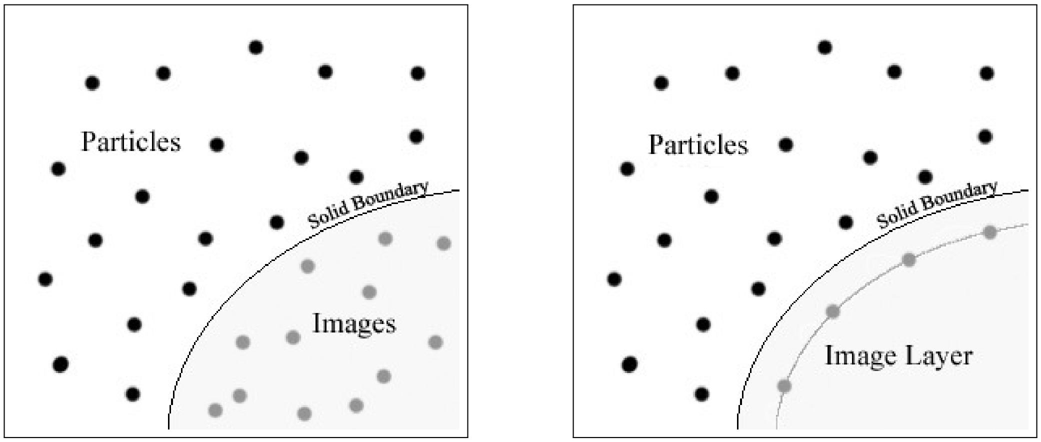

Figure 8.2 Comparison of the image vortex layer of the present method with the image vortex system in Ploumhans & Wickelmans (2000).

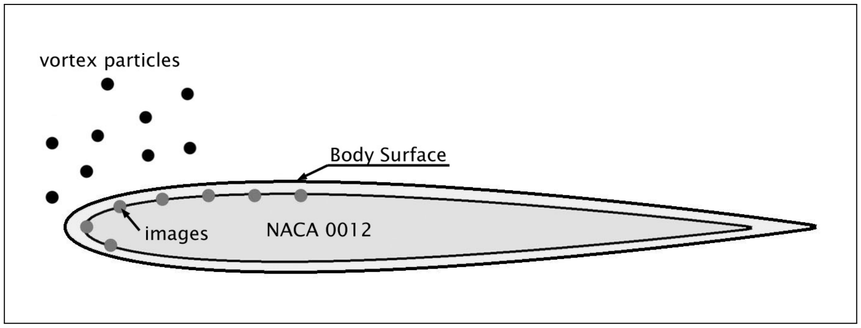

Figure 8.3 Example of the image vortex layer around an NACA 0012 hydrofoil.

The extended vorticity of the image layer adds to the vorticity on the body,

$$\underline{\omega}\left(\underline{x}\right) = \sum_{i=1}^{N} \alpha_i \, \zeta_{\epsilon i}\left(\underline{x} - \underline{x}_i\right) + \sum_{m=1}^{M} \alpha_m^* \, \zeta_{\epsilon m}^*\left(\underline{x} - \underline{x}_m^*\right) \quad \text{for} \quad \underline{x} \in \partial\mathcal{D}, \tag{8.28}$$

where the superscript '$*$' refers to quantities of images. Then the vorticity flux on the body is expressed as

$$\frac{\partial \underline{\omega}}{\partial n} = \sum_{i=1}^{N} \alpha_i \frac{\partial \zeta_{\epsilon i}\left(\underline{x} - \underline{x}_i\right)}{\partial n} + \sum_{m=1}^{M} \alpha_m^* \frac{\partial \zeta_{\epsilon m}^*\left(\underline{x} - \underline{x}_m^*\right)}{\partial n} \quad \text{for} \quad \underline{x} \in \partial\mathcal{D}, \tag{8.29}$$

where $\underline{n}$ is the normal vector of the particle $\underline{x}$ and the zero vorticity-flux condition means $\partial\underline{\omega}/\partial n = 0$ at the body surface. The normal derivative of the smoothing function is found to be

$$\frac{\partial \zeta_{\epsilon i}\left(\underline{r}\right)}{\partial n} = -\frac{1}{2\pi\,\epsilon^4}\exp\left(-\frac{\underline{r}^2}{2\epsilon^2}\right)\left(\underline{r}\cdot\underline{n}\right). \tag{8.30}$$

Denoting the radius of the image blob by ϵ^*, Eq. (8.29) is expressed as

$$\begin{aligned}\frac{\partial \underline{\omega}(\underline{x}_p)}{\partial n} &= \frac{1}{2\pi\epsilon^{*4}}\sum_{m=1}^{M}\alpha_m^*\exp\left(-\frac{\underline{r}^{*2}}{2\epsilon^{*2}}\right)\left(\underline{r}^*\cdot\underline{n}\right)\\ &\quad+\frac{1}{2\pi\,\epsilon^4}\sum_{i=1}^{N}\alpha_i\exp\left(-\frac{\underline{r}^2}{2\epsilon^2}\right)\left(\underline{r}\cdot\underline{n}\right)=0.\end{aligned} \tag{8.31}$$

where $\underline{r} = \underline{x}_p - \underline{x}_i$ and $\underline{r}^* = \underline{x}_p - \underline{x}_m$. With the image layer, Eq. (8.24) is replaced by

$$\begin{aligned}\frac{d\alpha_i}{dt}\frac{1}{S_i} &= \frac{2\nu}{\epsilon^2}\sum_{j=1}^{N}\left[\frac{\alpha_j}{S_j}-\frac{\alpha_i}{S_i}\right]\zeta_\epsilon\left(|\underline{x}_i-\underline{x}_j|\right)\ S_j\\ &\quad+\frac{2\nu}{\epsilon^2}\sum_{m=1}^{M}\left[\frac{\alpha_m^*}{S_m}-\frac{\alpha_i}{S_i}\right]\zeta_\epsilon\left(|\underline{x}_i-\underline{x}_m|\right)\ S_m,\end{aligned} \tag{8.32}$$

where $S_m = \epsilon^{*2}$ for the image. This technique is insensitive to the local shape of a body. That is, because one image layer in the body is used, it may be suitable in the case of a thin body, e.g., foils with cusped trailing edges.

8.2.3.2 Image layer method in three-dimensions

For particle i close to the boundary, the computation of the PSE involves two subsets of particles: $\mathcal{P}_i$(the subset of particles close enough to $\underline{x}_i$) and $\mathcal{P}_i'$ (the set of images of the particles in $\mathcal{P}_i$). The position of image particle $\underline{x}_i'$ is computed using symmetry, the plane of symmetry being the plane tangent to body surface closest to $\underline{x}_i$. The volume and smoothing parameter of an image particle are taken equal to those of the original particle. The two components of the strength ($\underline{\alpha}_i'$) parallel to the tangential plane are taken equal to those of $\underline{\alpha}_i$. The normal component is taken with the opposite sign. If (ξ, η, n) are the local orthogonal coordinates,

$$\underline{\alpha}'_i = (\underline{\alpha}_i \cdot \underline{\xi})\,\xi + (\underline{\alpha}_i \cdot \underline{\eta})\,\eta - (\underline{\alpha}_i \cdot \underline{n})\,n \tag{8.33}$$

Lee (2005) pointed out that the position and strength of an image are not easily determined for a slender body such as NACA0012 hydrofoil, if the technique outlined above is used. He suggested a more general treatment for the image, and applied successfully to the 2-D flow simulation around NACA0012 at arbitrary angles of attack, as well as around a circular cylinder. He positioned images just below the control points of the discretized body panels (the total number of image particles becomes the number of panels). The strength of an image particle can be determined from the zero vorticity flux condition on the control point of a panel,

$$\frac{\partial \underline{\omega}}{\partial n} = \sum_{i=1}^{N} \underline{\alpha}_i \frac{\partial \zeta_\epsilon(\underline{x} - \underline{x}_i)}{\partial n} + \sum_{m=1}^{M} \underline{\alpha}'_m \frac{\partial \zeta'_\epsilon(\underline{x} - \underline{x}'_m)}{\partial n} \tag{8.34}$$

Cottet & Poncet (2003) demonstrated in the immersed boundary VIC method that such particular diffusion formulas are no longer necessary near the boundary. He used plain PSE formulas all over the domain, even near the boundary. The spurious vorticity in the flow, usually introduced with the PSE ignoring the boundary, was supposed to be corrected from the application of vorticity flux formulas, because the evaluation of the slip and the enforcement of the no slip boundary condition are made on the boundary itself. The PSE in this work pursued Cottet's demonstration, but as described in the section 8.4.3 for the potential field calculation, normal flow condition is satisfied on the panel as well as tangential flow. Figure **8.4** compares the differences between the PSE using images and immersed boundary PSE schematically.

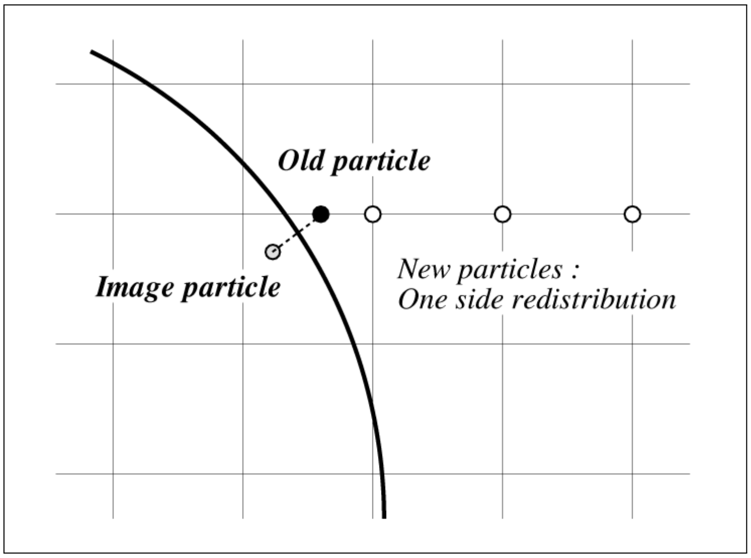

(a) Remeshing and image in vortex method

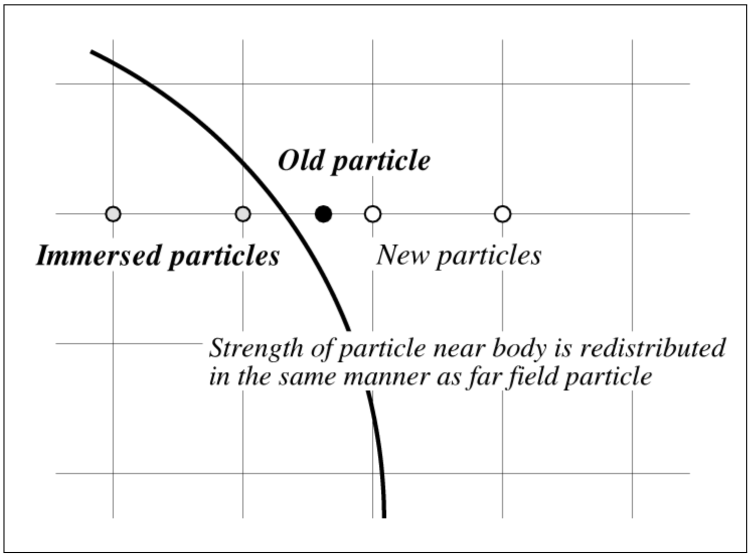

(b) Immersed boundary and particles in VIC

Figure **8.4** Comparison of particle locations between the vortex particle method and the immersed boundary method in VIC.

8.2.4 No-slip condition: Vorticity flux at wall

The solution of the heat equation may be expressed in integral form as: [1]

$$\underline{\omega} \;=\; \nu \int_0^t \int_{\partial \mathcal{D}} H_\epsilon\left(\underline{x}, t; \xi\ ,\ \tau\right) \frac{\partial \underline{\omega}\left(\underline{\xi}, \tau\right)}{\partial n}\, d\xi\, d\tau \tag{8.35}$$

where

$$H_\epsilon \;=\; \frac{1}{4\pi\nu\left(t-\tau\right)}\ \exp\left(-\frac{\left|\underline{x}-\underline{\xi}\right|^2}{4\nu\left(t-\tau\right)}\right)$$

Therefore, the Gaussian smoothing meets all these requirements and is a natural choice since it is the kernel of the heat equation. Its associated η_ϵ is also a Gaussian and with the proper normalization, it is found that $H_\epsilon = \eta_\epsilon$ which be of some computational benefit (Raviart 1987, Pepin 1990),

$$H_\epsilon\left(\left|\underline{x}-\underline{y}\right|\right) \;=\; \frac{1}{2\pi\epsilon^2}\ \exp\left(-\frac{\left|\underline{x}-\underline{y}\right|^{\,2}}{2\epsilon^2}\right) \tag{8.36}$$

where $2\,\nu\, dt \;=\; \epsilon^2$.

A vorticity flux $(\nu\dfrac{\partial\omega}{\partial n})$ may be determined on the boundary in such a way that the no-slip condition is satisfied. Wu *et al.* (1994) introduced a relation between a vorticity flux and spurious slip velocity(V_s). If a vorticity flux is constant over a small interval of time (Δt), the spurious slip velocity(V_s) that would appear at the end of the time step can be regarded as the coupling term corresponding to the tangential gradient of the surface pressure in Eq. (6.48). The newly computed V_s, which can be obtained by the Biot-Savart integral, can then used to absorb the coupling term and consequently to update a vorticity flux:

$$\left(\nu\,\frac{\partial\omega}{\partial n}\right)^{(k+1)} = \left(\nu\,\frac{\partial\omega}{\partial n}\right)^{(k)} + \left(\frac{V_s}{\Delta t}\right)^{(k)} \tag{8.37}$$

wher the superscript notation refers to the iterative step.

The iteration continues until the no-slip condition is satisfied, i.e., until V_s

---

[1] See Friedman (1964).

reduces to a value within a preset allowance. Eq. (8.37) indicates the total flux to be emitted into the flow for the diffusion process during a time Δt. This elegant decoupled scheme was introduced by Wu *et al.* (1994), through which we can efficiently recover the global coupling between the vorticity and the pressure boundary condition instead of the implementation of the fully coupled schemes.

The vorticity flux is distributed to neighboring particles by discretizing the Green's integral for the inhomogeneous Neumann problem corresponding to the diffusion equation. For diffusion within the schemes to work properly, the spatial distribution of the particles must remain as uniform as possible. To re-mesh the distorted particles, we overlaid a uniform rectangular grid. This is necessary in order to accurately interpolate the current vorticity field onto the new grid of initially uniformly spaced particle location that replaces the distorted particle locations (as suggested by Ploumhans and Winckelmans (2000)).

8.2.4.1 Wall viscous diffusion in two-dimensions

The total flux to be emitted into the flow for the diffusion process must be emitted during a time Δt. In effect, the vortex sheet V_s must be distributed to neighboring particles by discretizing the Green's integral for the inhomogeneous Neumann problem corresponding to the diffusion equation. As shown in Figure **8.5** , consider a panel of uniform strength V_s located along the x-axis, and diffusing to the right side. The vortex sheet does not diffuse toward the interior of the body. The amount of circulation, $\Delta\alpha_i$, that will be imposed on the particle located at (x_i, y_i) $(y_i > 0\ ,\ x_i\ (any\ sign))$, is given by

$$\Delta\alpha_i = \int_{x_i-h_i/2}^{x_i+h_i/2} \int_{y_i-h_i/2}^{y_i+h_i/2} \Delta\omega\, dx\, dy \tag{8.38}$$

where ${h_i}^2 = S_i$ is the fluid area associated with particle i. The change in vorticity $\Delta\omega$ is due to the flux from the panel acting over a time Δt, which reduced t.

$$\Delta\omega = \int_0^{\Delta t} \frac{d\omega}{dt}\, dt \tag{8.39}$$

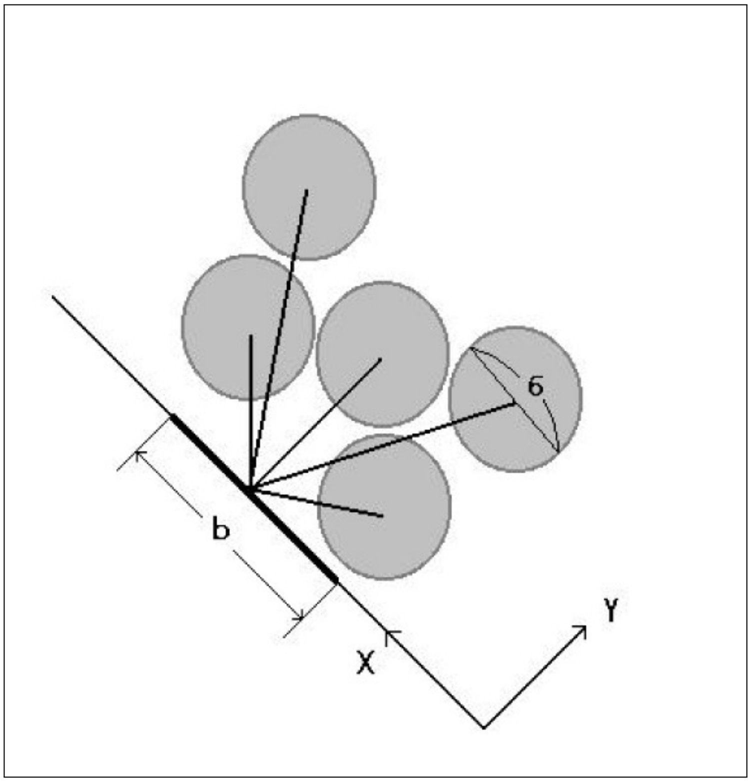

Figure **8.5** Particles with respect to a panel for viscous wall diffusion.

Then,

$$\frac{d\alpha_i}{dt} = \iint \frac{d\omega}{dt}\, dx\, dy \tag{8.40}$$

$$\Delta\alpha_i = \int_0^{\Delta t} \frac{d\alpha_i}{dt}\, dt \approx \frac{d\alpha_i}{dt}\, \Delta t \tag{8.41}$$

Eq (8.41) is integrated numerically using mid-point rule:

$$\begin{aligned} \Delta\alpha_i &= h_i{}^2\, V_s \left(1 - \kappa\sqrt{\pi\nu\Delta t}\right)^{-1} \frac{1}{\sqrt{2\pi\,\nu\,\Delta t}} \times \\ &\times \exp\left(-\frac{y_i{}^2}{2\,\nu\,\Delta t}\right) \left[\mathrm{erfc}(s)\right]_{(x_i+h_i/2)/\sqrt{2\,\nu\,\Delta t}}^{(x_i-h_i/2)/\sqrt{2\,\nu\,\Delta t}} \end{aligned} \tag{8.42}$$

where $\mathrm{erfc}(s) = \dfrac{2}{\sqrt{\pi}} \displaystyle\int_s^{\infty} \exp(-v^2)\, dv = 1 - \mathrm{erf}(s)$. To resolve the non conservation problem caused by numerical integration, the integral of Eq. (8.40) is performed as follows (Ploumhans & Winckelmans 2000)

$$\begin{aligned}\frac{d\alpha_i}{dt} &= \iint \frac{d\omega}{dt}\, dx\, dy = \frac{\Delta\gamma}{\Delta t}\left([\mathrm{erfc}(s)]^{(y_i-h_{i,l}/2)/\sqrt{4\,\nu\, t}}_{(y_i+h_l/2)/\sqrt{4\,\nu\, t}}\right) \times \\ &\times \left\{\sqrt{4\,\nu\, t}\,\frac{1}{2}\left([\mathrm{ierfc}(s)]^{x_i-b/2-h_i/2/\sqrt{4\,\nu\, t}}_{x_i-b/2+h_i/2/\sqrt{4\,\nu\, t}} - [\mathrm{ierfc}(s)]^{x_i+b/2-h_i/2/\sqrt{4\,\nu\, t}}_{x_i+b/2+h_i/2/\sqrt{4\,\nu\, t}}\right)\right\}\end{aligned} \tag{8.43}$$

where $\mathrm{ierfc}(s) = \int_s^{\infty} (u)\, du = \frac{1}{\sqrt{\pi}} \exp(-s^2) - s\, \mathrm{erfc}(s)$, and $h_{i,l}/2 = x_i$ if $0 \le x_i < h_i$ and $h_{i,l}/2 = h_i/2$ otherwise.

If particles are on a regular lattice aligned with the panel, Eq.(8.43) is always conservative. Thus, it could also be used to perform under resolved computations, where the value of $h^2/(4\nu\Delta t)$ would be very high. The large value of $h^2/(4\nu\Delta t)$ is equivalent to $h^2/\sigma^2 \gg 1$, which means the violation of the blob overlap condition($h/\sigma < 1$). In practice, however, the spatial distribution of the particles is not well aligned with the vortex panel. Therefore, in order to enforce conservation, the correction is made as follows (Ploumhans & Winckelmans 2000):

$$\Delta\alpha_{i,conserv.} = \Delta\alpha_i + \frac{(\Delta\alpha_i)^2}{\sum_j (\Delta\alpha_j)^2}\left(b\, V_s - \sum_j \Delta\alpha_j\right), \tag{8.44}$$

where j runs over all particles concerned by the panel V_s. This scheme minimizes

$$\sum_i (\Delta\alpha_i - \Delta\alpha_{i,conserv.})^2/(\Delta\alpha_i)^2 \tag{8.45}$$

with the constraint that $(b\, V_s) - (\sum_i \Delta\alpha_{i,conserv.}) = 0$.

For diffusion with the above schemes to work properly, the spatial distribution of the particles must remain fairly uniform as long as possible. This is one reason why particle redistribution procedure must be performed every 5 to 10 time steps.

8.2.4.2 Wall viscous diffusion in three-dimensions

The process that the vorticity created at the boundary shed on to the particles has been accounted for by the diffusion, and the solution to the diffusion equation for the voricity with homogeneous initial condition and the Neumann type boundary condtion has been implemented in an appropriate discretized form. The solution may be expressed in integral form using Green's function for the diffusion equation.

The 3-D version of the discretization is well explained in Ploumhans (2002). Consider a retangular panel of uniform strength $\Delta\underline{\gamma}(=\underline{n}\times\underline{u}_s)$ and size $b\times f$, located on the XY plane, and diffusing toward the positive Z direction. A particle located at (x_i, y_i, z_i), $(z_i > 0)$, receives, from that panel, an amount of 'vorticity×volume' given by

$$\Delta\underline{\alpha}_i = \int_0^{\Delta t} \frac{d\underline{\alpha}_i}{dt}\, dt \tag{8.46}$$

with

$$\frac{d\underline{\alpha}_i}{dt} = \int_{x_i-h_i/2}^{x_i+h_i/2} \int_{y_i-h_i/2}^{y_i+h_i/2} \int_{z_i-h_i/2}^{z_i+h_i/2} \frac{d\underline{\omega}}{dt}\, dx\, dy\, dz \tag{8.47}$$

The rate of change of the vorticity owing to the panel is equal to

$$\begin{aligned}\frac{d\underline{\omega}}{dt} =& \frac{\Delta\underline{\gamma}}{\Delta t}\frac{1}{2\sqrt{\pi}}\frac{1}{\sqrt{4\,\nu\,t}}\exp\left(-\frac{z^2}{4\,\nu\,t}\right)\times \\ &\times\left[\mathrm{erfc}(s)\right]_{(x-b/2)/\sqrt{4\,\nu\,t}}^{(x+b/2)/\sqrt{4\,\nu\,t}} \times \left[\mathrm{erfc}(s)\right]_{(y-f/2)/\sqrt{4\,\nu\,t}}^{(y+f/2)/\sqrt{4\,\nu\,t}}\end{aligned} \tag{8.48}$$

Equation (8.48) is then integrated exactly, giving

$$\begin{aligned}\frac{d\underline{\alpha}_i}{dt} =& \frac{\Delta\underline{\gamma}}{\Delta t}\left(\left[\mathrm{erfc}(u)\right]_{(z_i+h_i/2)/\sqrt{4\nu t}}^{(z_i-h_{i,l}/2)/\sqrt{4\,\nu\,t}}\right) \\ &\times\left\{\sqrt{\nu\,t}\left(\left[\mathrm{ierfc}(u)\right]_{(x_i-h_i/2-b/2)/\sqrt{4\,\nu\,t}}^{(x_i+h_i/2-b/2)/\sqrt{4\,\nu\,t}} - \left[\mathrm{ierfc}(u)\right]_{(x_i-h_i/2+b/2)/\sqrt{4\,\nu\,t}}^{(x_i+h_i/2+b/2)/\sqrt{4\,\nu\,t}}\right)\right\} \\ &\times\left\{\sqrt{\nu\,t}\left(\left[\mathrm{ierfc}(u)\right]_{(y_i-h_i/2-f/2)/\sqrt{4\,\nu\,t}}^{(y_i+h_i/2-f/2)/\sqrt{4\,\nu\,t}} - \left[\mathrm{ierfc}(u)\right]_{(y_i-h_i/2+f/2)/\sqrt{4\,\nu\,t}}^{(y_i+h_i/2+f/2)/\sqrt{4\,\nu\,t}}\right)\right\}\end{aligned} \tag{8.49}$$

where $\text{ierfc}(s) = \int_s^\infty \text{erfc}(x)\,dx$. Notice that $h_{i,l}/2 = z_i$ if $0 \le z_i < h_i$ and $h_{i,l}/2 = h_i/2$ otherwise. Even though Eq. (8.49) is exact for a rectangular panel of size $b \times f$, the equation is still applicable to triangular panels, if each triangular panel is considered as a square centered at the triangle centroid.

In the intial setting of the vortex particles, the vortex particles with zero strength are first distributed on a regular mesh and several iterations of wall diffusion and slip velocity calculation are carried out to achieve no slip on the surface. The procedure is repeated at the end of each time marching step.

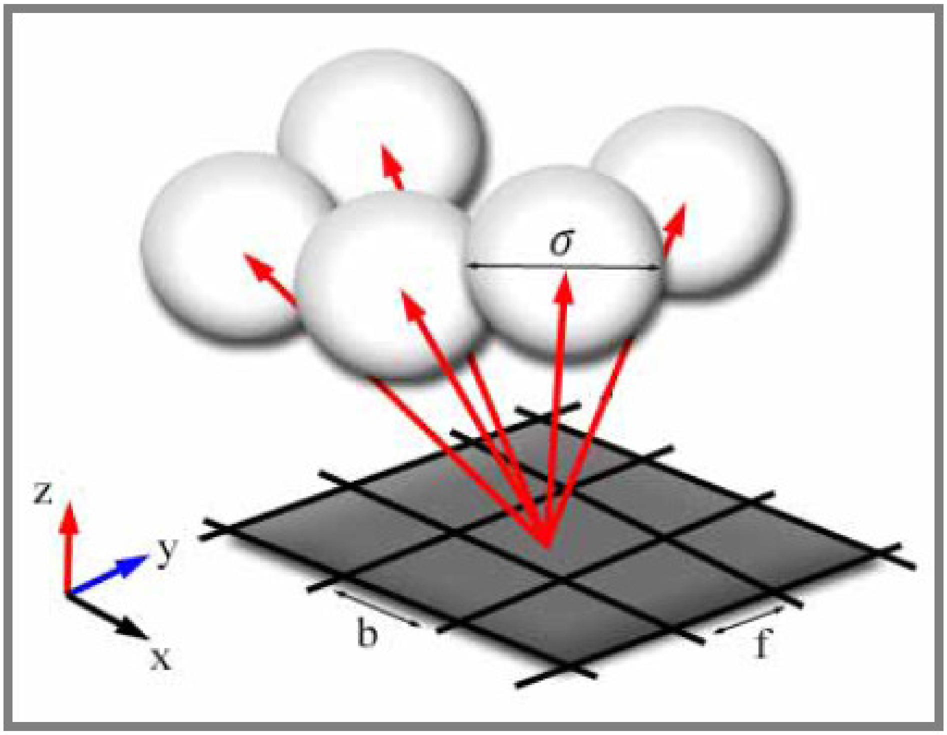

Figure 8.6 Diffusion of vorticity from body boundary. Vorticity correction is performed in the iterative way for satisfying the boundary condition at the surface.

8.2.5 Pressure equation

Once the vorticity and the velocity fields are updated, the integral equation for the total pressure may be solved. Basically, the process for calculating the pressure in a Lagrangian frame is similar to one in an Eulerian frame. Substituting Eq. (6.49) for $\partial H/\partial n$ into Eq. (6.44) yields the limiting form for H as a field point approaches the surface points ($\underline{x}_B$) of a solid body:

$$\begin{aligned}\frac{1}{2}H \;+\; \frac{1}{2\pi}\oint_{C_B} H\,\frac{\partial(\ln r)}{\partial n}\,dl = &\\ -\frac{1}{2\pi}\oint_{C_B}\left[\underline{n}\cdot\frac{\partial\underline{u}}{\partial t}-\underline{n}\cdot(\underline{q}\times\underline{\omega})+\underline{n}\cdot(\nabla\times(\nu\,\underline{\omega}))\right]\ln r\,dl &\\ +\frac{1}{2\pi}\int_S \nabla\cdot(\underline{q}\times\underline{\omega})\,\ln r\,dS, & \qquad (8.50)\end{aligned}$$

where the integrals over C_B are evaluated on the surface of a body in the sense of the Cauchy principal value integral. Using the vector operation for the integrand of the surface integral in Eq. (8.50), namely, $\nabla\cdot(\underline{q}\times\underline{\omega})\,\ln r = \nabla\cdot\left\{(\underline{q}\times\underline{\omega})\,\ln r\right\}-(\underline{q}\times\underline{\omega})\cdot\nabla(\ln r)$ and applying the divergence integral theorem to the resultant expression, yield a Fredholm integral equation of the second kind for H:

$$\begin{aligned}\frac{1}{2}H+\frac{1}{2\pi}\oint_{C_B} H\,\frac{\partial(\ln r)}{\partial n}\,dl \;=\; & -\frac{1}{2\pi}\oint_{C_B}\left[\underline{n}\cdot\frac{\partial\underline{u}}{\partial t}+\underline{n}\cdot(\nabla\times(\nu\,\underline{\omega}))\right]\ln r\,dl\\ & -\frac{1}{2\pi}\int_S(\underline{q}\times\underline{\omega})\cdot\nabla(\ln r)\,dS. \qquad (8.51)\end{aligned}$$

Furthermore, if we assume that the body will be either fixed, or impulsively started, as in the test problem, the equation reduces to a simpler form:

$$\begin{aligned}\frac{1}{2}H+\frac{1}{2\pi}\oint_{C_B} H\,\frac{\partial(\ln r)}{\partial n}\,dl \;=\; & -\frac{1}{2\pi}\oint_{C_B}\nu\,\frac{\partial\omega_B}{\partial s}\ln r\,dl\\ & -\frac{1}{2\pi}\int_S(\underline{q}\times\underline{\omega})\cdot\nabla(\ln r)\,dS. \qquad (8.52)\end{aligned}$$

The two integrals over C_B in Eq. (8.52) may be replaced by the sum of the individual integral form for the contribution of each straight-line body panel. This can then be solved using the panel method in a way similar to that used in potential flow analysis (as mentioned before).

The surface integral term on the right-hand side of Eq. (8.52) may be solved with distorted vorticity particles, unlike the well aligned cell elements in an Eulerian description. The discretization of Eq. (8.52) (except the last surface integral term) is expressed as

$$\begin{aligned}\frac{1}{2}H_i \;+\; \frac{1}{2\pi}\sum_{j=1}^{M} H_j \int_{C_j} \nabla(\ln r)\, dl_j = -\frac{1}{2\pi}\sum_{j=1}^{M}\left\{\underline{n}\cdot(\nabla\times(\nu\,\underline{\omega}))_j\right\}\int_{C_j}\ln r\, dl_j \\ -\frac{1}{2\pi}\int_S(\underline{q}\times\underline{\omega})\cdot\nabla(\ln r)\, dS. \qquad (8.53)\end{aligned}$$

Body vorticities on the body panels may be calculated from the distribution function of Eq. (8.2). The second term on the right-hand side of Eq. (8.53), (source-like strength, $\underline{n}\cdot\nabla\times(\nu\,\underline{\omega})$) is calculated by numerically differentiating the body vorticities in the tangential direction of the body surface panel. With the vorticity field of Eq. (8.2), the last integral term in Eq. (8.53) is discretized as

$$\begin{aligned}\frac{1}{2\pi}\int(\underline{q}\times\underline{\omega})\cdot\nabla(\ln r)\, dS \;&=\; \frac{1}{2\pi}\sum_{k=1}^{N}\left[\underline{q}_k\times(\alpha_k\,\underline{k})\cdot\frac{\underline{r}_k}{|\underline{r}_k|^2}\int_{S_k}\zeta_{\epsilon_k}\, dS\right] \\ &=\; \frac{1}{2\pi}\sum_{k=1}^{N}\left[\frac{(x-x_k)\,q_y\,\alpha_k-(y-y_k)\,q_x\,\alpha_k}{|\underline{r}_k|^2}\right]\times \\ &\qquad\times\left[1-\exp\left(-\frac{|\underline{r}_k|^2}{2\,\epsilon^2}\right)\right] \qquad (8.54)\end{aligned}$$

Consequently, the total pressure H_i $(i = 1, 2, \cdots, M)$ on the body panels is calculated by using the following equation (see Appendix B):

$$\sum_{j=1}^{M}\left(\frac{1}{2}\delta_{ij} \;+\; A_{ij}\right)H_i \;=\; -\left(\sum_{j=1}^{M}C_{ij}+\sum_{k=1}^{N}S_{ik}\right) \qquad (8.55)$$

where

$$\begin{aligned}A_{ij} \;&=\; \int_{C_j}\underline{n}_j\cdot\nabla G\left(|\underline{x}_i-\underline{x}_j|\right)\, dl \\ C_{ij} \;&=\; \int_{C_j}\underline{n}_j\cdot\left(\nabla\times(\nu\,\underline{\omega}_j)\right)G\left(|\underline{x}_i-\underline{x}_j|\right)\, dl \\ S_{ik} \;&=\; \left(\underline{q}_k\times\underline{\Gamma}_k\right)\cdot\underline{K}_\epsilon\left(|\underline{x}_i-\underline{x}_k|\right)\end{aligned}$$

Then the total pressure at the field is explicitly calculated with the total pressure on the body surface :

$$H_i = -\sum_{j=1}^{M} A_{ij}\, H_j - \left(\sum_{j=1}^{M} C_{ij} + \sum_{k=1}^{N} S_{ik} \right) \tag{8.56}$$

where $i = 1, 2, \cdots, N$.

8.2.6 Computational procedure

As shown in Figure 8.7 , the numerical implementation for two dimensional Lagrangian formulation can be summarized in the following sub-steps of the solution of the system of governing equations. The overall procedure is similar to those of Koumoutsakos *et al.* (1994) and Ploumhans *et al.* (2000). In the present method, however, the irrotational (potential field) part of the velocity field is calculated by using the well-established panel method and the iterative process is used for more physically suitable creation of vorticity flux in order to ensure the no slip condition, which was taken on the previous vorticity-based method in the Eulerian description (Suh and Kim 1999). A typical time step, Δt, of the Lagrangian vortex method is divided into two substeps.

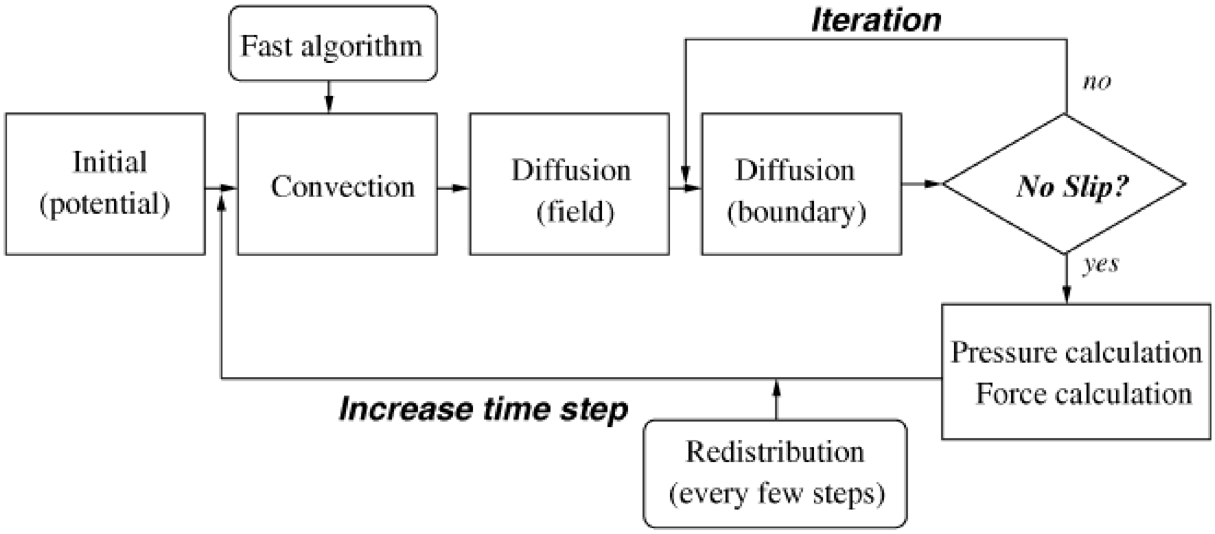

Figure 8.7 Numerical procedure of the vortex particle method.

(1) The local velocity ($\underline{q} = \underline{u}_\omega + \nabla\phi + \underline{U}_\infty$) is computed as follows: $\underline{u}_\omega$ calculated by the Biot-Savart integral (Eq. (8.18)), $\nabla\phi$ calculated by the panel method (Eqs. (8.11)). Then, the velocity is integrated with a second-order Adam-Bashforth scheme (or a second-order Runge-Kutta method immediately after the redistribution process is applied) to convect the particle. Their strengths are updated with the PSE scheme (Eq. (8.32)) that is integrated with an Euler explicit scheme. Algorithmically, this step is expressed as

$$\underline{x}_i^{n+1} = \underline{x}_i^n + \Delta t\left(\frac{3}{2}\underline{q}_i(\underline{x}^n, \underline{\alpha}^n) - \frac{1}{2}\underline{q}_i(\underline{x}^{n-1}, \underline{\alpha}^{n-1})\right) \tag{8.57}$$

$$\underline{\alpha}_i^* = \underline{\alpha}_i^n + \Delta t \left.\frac{d\underline{\alpha}_i}{dt}\right|_{PSE} (\underline{x}^n, \underline{\alpha}^n). \tag{8.58}$$

(2) The vorticity flux $\nu\dfrac{\partial\omega}{\partial n}$ necessary on the body surface to cancel the slip velocity computed by sub-step (1), is computed (Eq. (8.18)). However, recalculation of the slip velocity on the body boundary may reveal that the no slip condition is not satisfied. Vorticity flux due to the remaining slip velocity is then re-calculated. The iteration continues until the no-slip condition is satisfied, i.e., until the spurious slip velocity reduces to a value within a preset allowance. The vorticity strength corresponds to a vorticity flux that must be emitted during a time Δt:

$$\underline{\alpha}_i^{n+1} = \underline{\alpha}_i^* + \Delta t \left.\frac{d\underline{\alpha}_i}{dt}\right|_{wall} (\underline{x}^{n+1}, \underline{\alpha}^*). \tag{8.59}$$

(3) The redistribution scheme is applied every few steps(herein every 5 to 10 time steps) to maintain spatial uniformity of the particle distribution. Once the vorticity and velocity are updated after two substeps are taken, the pressure equation (i.e., Eqs.(8.53) through (8.54)), is solved.

8.2.6.1 Redistribution

Vortex methods have been guaranteed on its convergence by the condition that particle cores overlap at all times. Redistribution is an essential operation to maintain a good representation of the vorticity field. The vortex-in-cell method is characterized by the information exchange between particles and grid, as is explained in section 8.4.2. As a good quality scheme to bring the particles information to grid, and the grid information to the particles, the M_4' scheme was introduced. The formula is also used for the redistribution of every few time steps. The scheme is continuous and so is the first derivative. It is known as a second order scheme. In summary, the M_4' formula is used at three stages of the method. First, when particle vorticity is interpolated on a regular Cartesian grid where velocity are evaluated, second, when the grid values are interpolated back to particles, and finally to redistribute the disorted particles onto uniform rectangular grid. In order to avoid for the number of particles to grow at a too high rate, a newly generated particle having strength $|\underline{\alpha}| < \epsilon_\alpha |\underline{\alpha}|$ and $Re_h = |\underline{\omega}| h^2/\nu < Re_{h,trsh}$ is deleted after redistribution. The particluar choice for the cutoff parameters is different with application.

In order to remesh on the distorted Lagrangian particles, we overlay a uniform rectangular grid as shown in Figure **8.8** . It is necessary to accurately interpolate the current vorticity field onto the new grid initially uniform-spaced particle location ($\tilde{\underline{x}}$) that replaces the distorted particle location ($\underline{x}$). After redistribution, the uniform grid cell centers become the location of the new particles.

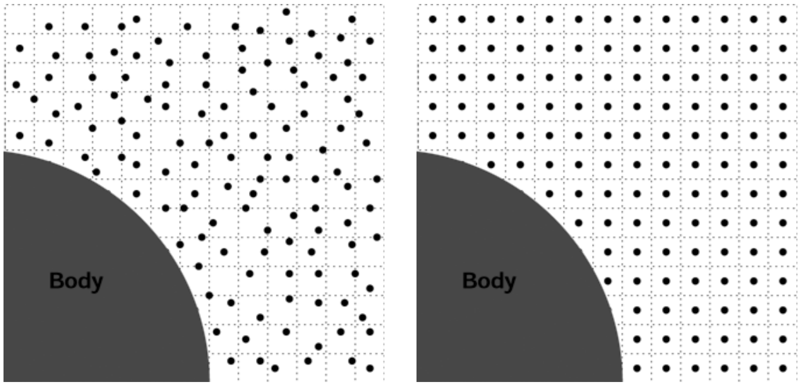

(a) Before redistribution (b) After redistribution

Figure 8.8 Redistribution scheme for a general boundary in two-dimensions.

The new particle strengths are determined using an appropriate interpolation kernel Λ so that:

$$\tilde{\Gamma}_i(\tilde{x}) \approx \sum_{j=1}^{N} \Gamma_j(x_j)\,\Lambda_p(\tilde{x}_i - x_j) \qquad (8.60)$$

where $\tilde{\Gamma}, \Gamma$ denote the new and old particle strength respectively, Λ_p interpolation kernel of p-th order. The process is not of the usual interpolation type as it is complicated by the fact that the particles are disordered. The basic analysis of interpolation of this type is given by Schoenberg (1973).

Consider first the normalized 1-D problem with unit spacing, $u = (x - \tilde{x})/h$. In the $\Lambda_3(u)$ scheme, an old particle located at $-1/2 \leq u \leq 1/2$ gives

$$\Lambda_3(u) = \begin{cases} (3-2u)\,(4u^2-1)/48 & \text{to the new particle located at} \quad -3/2 \\ (1-2u)\,(9-4u^2)/16 & \text{to the new particle located at} \quad -1/2 \\ (1+2u)\,(9-4u^2)/16 & \text{to the new particle located at} \quad 1/2 \\ (3+2u)\,(4u^2-1)/48 & \text{to the new particle located at} \quad 3/2 \end{cases}$$

If a wall is present, the redistribution of particles close to the wall must be modified so that particles are prevented from penetrating the body. This is achieved by using $\Lambda_p{}'$schemes. Two such schemes are detailed here, considering that an old particle is located at $-1/2 \leq u \leq 1/2$ and that the wall is at $u = -\frac{1}{2}$ for the $\Lambda_2{}'$scheme and $u = -1$ for the $\Lambda_3{}'$ scheme:

$$\Lambda_2{}'(u) = \begin{cases} (u-2-1/2)\,(u-1-1/2)/2 & \text{at} \;\; 1/2 \\ (u-1/2)\,(2-u+1/2) & \text{at} \;\; 3/2 \\ (u-1/2)\,(u-1-1/2)/2 & \text{at} \;\; 5/2 \end{cases}$$

$$\Lambda_3{}'(u) = \begin{cases} (1-2u)\,(2u-5)\,(2u-3)/48 & \text{at} \;\; -1/2 \\ (2u-5)\,(2u-3)\,(1+2u)/16 & \text{at} \;\; 1/2 \\ (1-2u)\,(2u-5)\,(1+2u)/16 & \text{at} \;\; 3/2 \\ (1-2u)\,(3-2u)\,(1+2u)/48 & \text{at} \;\; 5/2 \end{cases}$$

In the present approach, a Λ_3 scheme is used for particle located more than $3/2$ from the wall, a $\Lambda_3{}'$ scheme for particles with distance between $1/2$ and $3/2$, and a $\Lambda_2{}'$ scheme for particles less than $1/2$ from the wall (Λ_3, $\Lambda_3{}'$ and

$\Lambda_2{}'$ schemes is suggested by Ploumhans and Winckelmans (2000) for general boundary).

The 2-D redistribution formulas are Cartesian products of their 1-D counterparts. In this case, the interpolation kernel is defined as

$$\Lambda(x, y) = \Lambda(x)\,\Lambda(y)$$

We use two steps. First, an old particle is redistributed in the x-direction and temporary particles are created. This redistribution in the x-direction has created three or four temporary particles. Each temporary particle is then redistributed in the y-direction. Figure 8.9 gives an example of the redistribution scheme.

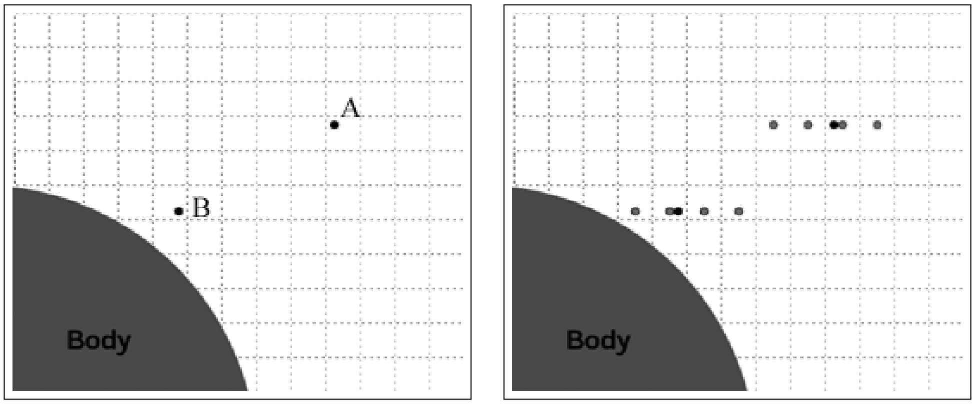

(a) Before redistribution (b) Redistribution in the x-direction

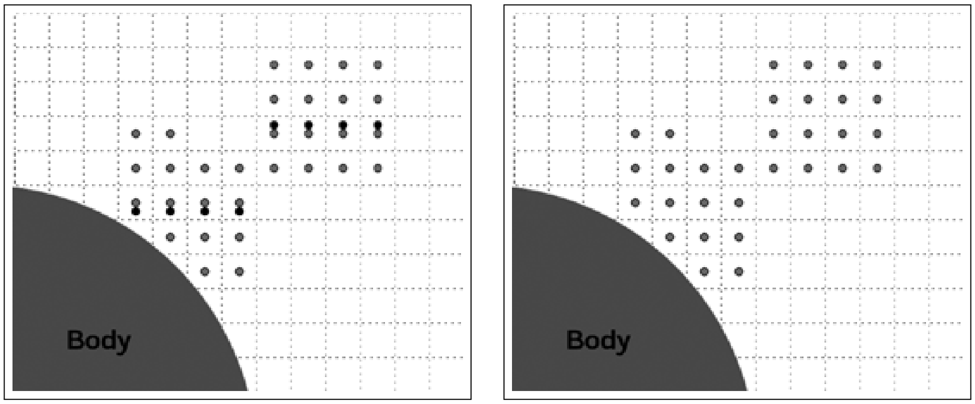

(c) Redistribution in the y-direction (d) After redistribution

Figure 8.9 Two-dimensional redisribution scheme for a particle near a boundary. Λ_3 scheme for point A, and Λ_3 $\Lambda_3{}'$ and $\Lambda_2{}'$ schemes for point B are used.

8.2.6.2 Force calculation

Hydrodynamic forces on the solid bodies can be computed either (1) by integration of the pressures on the boundaries, or (2) from integral expression of the system momentum balance. In vortex method, the second approach is very robust and has an almost zero computational cost. The total force $\underline{F}$ on a solid body can be computed from the time change of the linear impulse in the domain,

$$\underline{F} = -\rho \frac{d\underline{I}}{dt} \tag{8.61}$$

where ρ is the density and $\underline{I}$ is the first order moment of vorticity,

$$\underline{I} = \frac{1}{d-1} \int_V \underline{x} \times \underline{\omega} \, dV \tag{8.62}$$

with d the dimension of the space ($d = 3$ in 3-D, $d = 2$ in 2-D), and V the volume occupied by the fluid. The discretization of the equation is straight forward as it needs just summation running over all particles.

$$\begin{aligned} I_x &= \frac{1}{2} \int_V (y\,\omega_z - z\,\omega_y)\, dV \approx \sum_p (y_p\,\alpha_z - z_p\,\alpha_y) \\ I_y &= \frac{1}{2} \int_V (z\,\omega_x - x\,\omega_z)\, dV \approx \sum_p (z_p\,\alpha_x - x_p\,\alpha_z) \\ I_z &= \frac{1}{2} \int_V (x\,\omega_y - y\,\omega_x)\, dV \approx \sum_p (x_p\,\alpha_y - y_p\,\alpha_x) \end{aligned} \tag{8.63}$$

The coefficient for the drag and lift, when the flow direction generates drag in x direction and lift in y respectively, with the surface area A,

$$C_D = \frac{F_x}{\frac{1}{2}\rho U_\infty^2 A} = -\frac{2}{U_\infty^2 A} \frac{dI_x}{dt} \tag{8.64}$$

$$C_L = \frac{F_y}{\frac{1}{2}\rho U_\infty^2 A} = -\frac{2}{U_\infty^2 A} \frac{dI_y}{dt} \tag{8.65}$$

8.3 Some Comparative Results

8.3.1 Impulsively started cylinder

The time development of an incompressible viscous flow around an impulsively started circular cylinder is a classical problem in fluid mechanics. Despite the simplicity of its geometry, the flow structure is complicated and all possible flow phenomena occur (Ta Phouc Loc and Bouard 1985). In this section, comparative studies of this problem are performed with the results of the Eulerian formulation (Suh and Kim 1999) and other researchers' work, including theoretical (Bar-Lev and Yang 1975), and numerical (Koumoutsakos and Leonard 1995, Ploumhans and Winckelmans 2000) investigations of the validity of the Lagrangian formulation.

Input parameters for the present comparison are as follows: $Re = U_\infty\, D/\nu = 550$, $T = t\, U_\infty/D$, $\Delta t = 0.05$, blob size $\epsilon = 0.005$, surface panel size $d = \pi/600 \approx 0.0052$. These parameters are chosen to satisfy the stability condition $\nu\, \Delta t/h^2 = \mathcal{O}(1)$ for the diffusion term, and to satisfy the stability conditions of the second-order Adam-Bashforth scheme for the convection term, and the explicit Euler scheme for time marching. N particles (or blobs) result in the so-called 'N-body problem' in the evaluation of the Biot-Savart integral. Therefore, the convection and diffusion terms are treated with the fast algorithm (Greengard 1987) to reduce computing time. Computational parameters used for the present comparison are tabulated in Table 8.1.

Figure 8.10 gives the comparison of vortex sheet strength with the results by Ploumhans and Winckelmans (2000).

Table 8.1 Parameters used in the numerical simulation of the flow around an impulsively started circular cylinder.

	Finite Volume Method	Vortex Particle Method
Reynolds number	550	550
Time step, Δt	0.01	0.01
Radius	0.5	0.5
Number of surface panels	600	600
Panel size	about 0.005	about 0.005
Grid meshes	600×40	$\cdot$
Particles	$\cdot$	$9000 \sim 70000$
Computational domain	2.5 × diameter	no limit
Computational time (pentium IV)	about 6 hours (400 time steps)	about 8 hours (400 time steps)

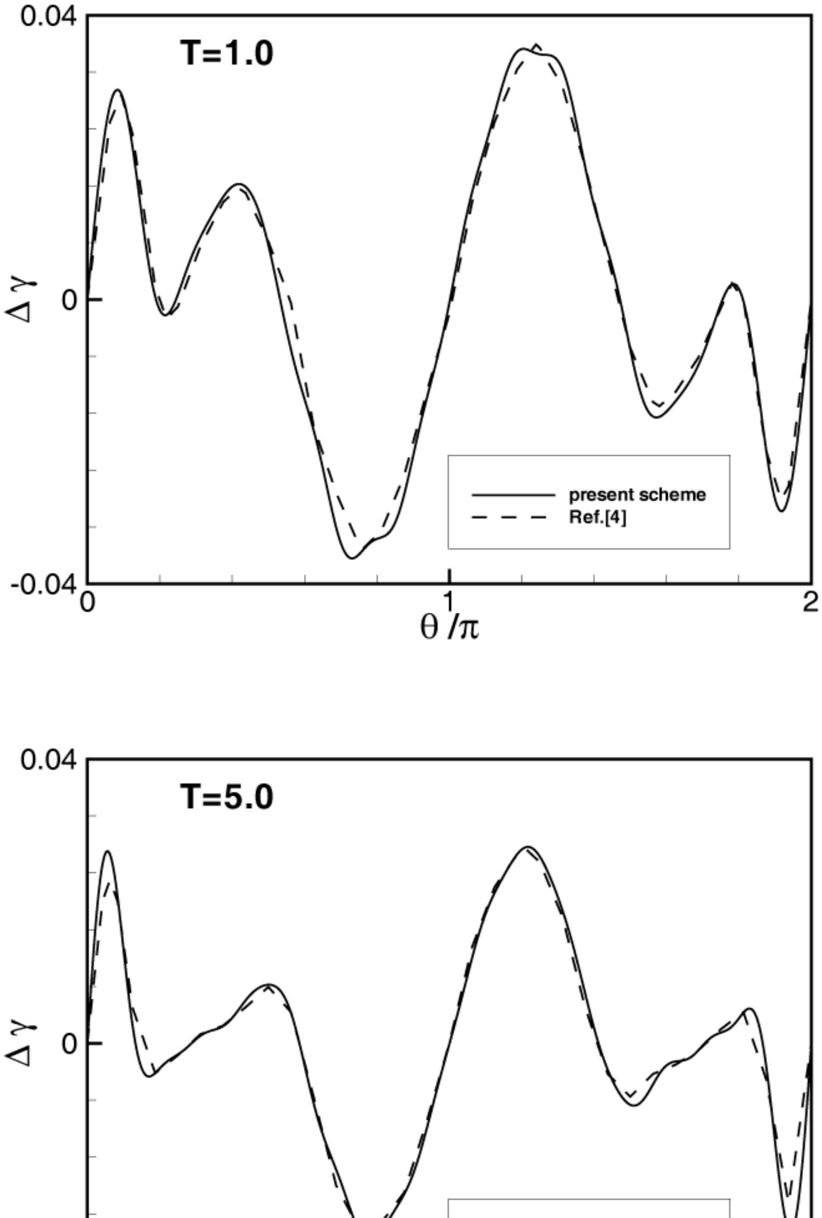

The vortex sheet strength(V_s) is equivalent to the accumulation of spurious slip velocity on the body boundary, which is calculated during the iterative process for the no-slip condition. The results of Ploumhans and Winckelmans are obtained in a manner such that vortex singularities are distributed on the body surfaces, and the no-slip condition is conferred to the interior boundary surfaces, which is equivalent to a no-penetration condition. Figure 8.10 shows that the distribution of V_s is in good agreement, except for some peak values. This implies that the iterative process for the body boundary condition imposed in FVM is also applicable to the vortex particle method.

A comparison is made in Figure 8.11 of I_x as a function of $T = t\,U_\infty/D$ for the x-component of momentum $\left(\underline{I} = \int_S \underline{x} \times \underline{\omega}\, dS\right)$, $I_x = \int_S y\,\omega\, dS = \sum_p y_p\,\alpha_p$, and Figure 8.11 includes the analytical solution for early developing flows $(T < 0.25)$.

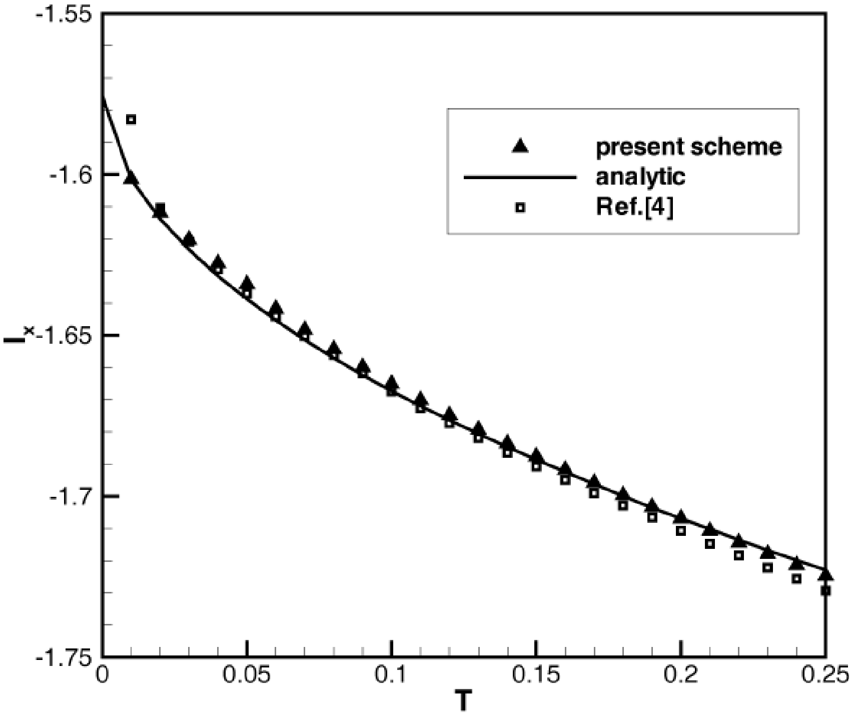

Figure **8.11** Comparison of I_x for the impulsively started cylinder problem $(0 < T < 0.25)$. Solid line (−): analytical solution (Bar-Lev & Yang (1975)); ▲: Lagrangian vortex method (present scheme); □: Lagrangian vortex method (Ploumhans & Winckelmans (2000)).

The numerical and analytical results are in good agreement. As shown in Figure 8.12 , for a longer time interval, the two numerical methods give indistinguishable results.

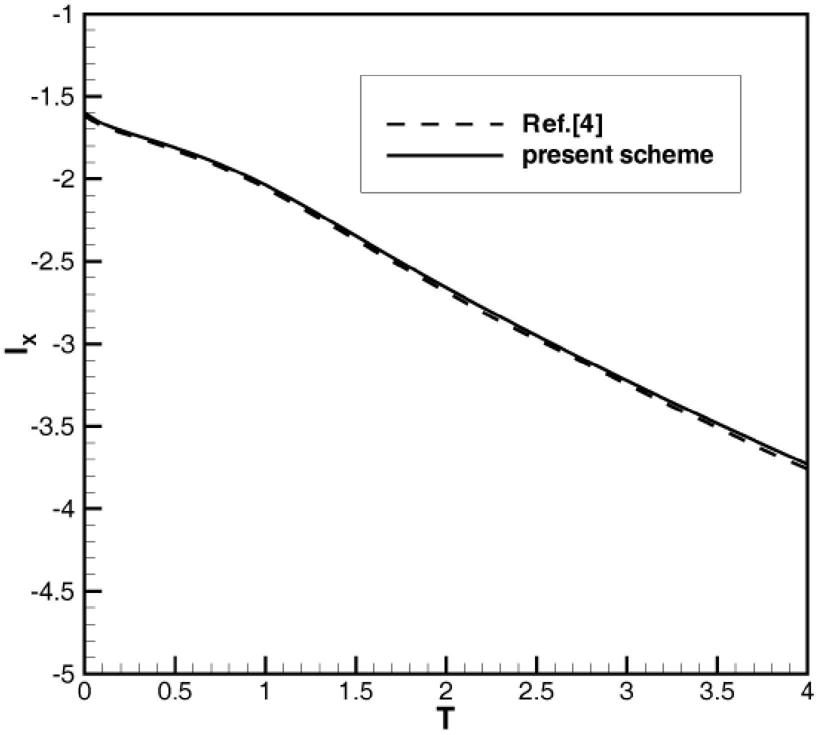

Figure 8.12 Comparison of I_x for the impulsively started cylinder problem ($0 < T < 4$). Solid line (–): Lagrangian vortex method (present scheme); dashed line (– –): Lagrangian vortex method (Ploumhans & Winckelmans (2000)).

The same comparison for the drag coefficient, $C_D = F_x/\frac{1}{2}\rho U_\infty^2 D$ with $F_x = -\rho\, dI_x/dt$, is shown in Figure 8.13 and Figure 8.14 . Here, the result obtained by FVM is included. Figure 8.13 shows that, of the two methods, the present Lagrangian scheme produces results somewhat closer to the analytical results.

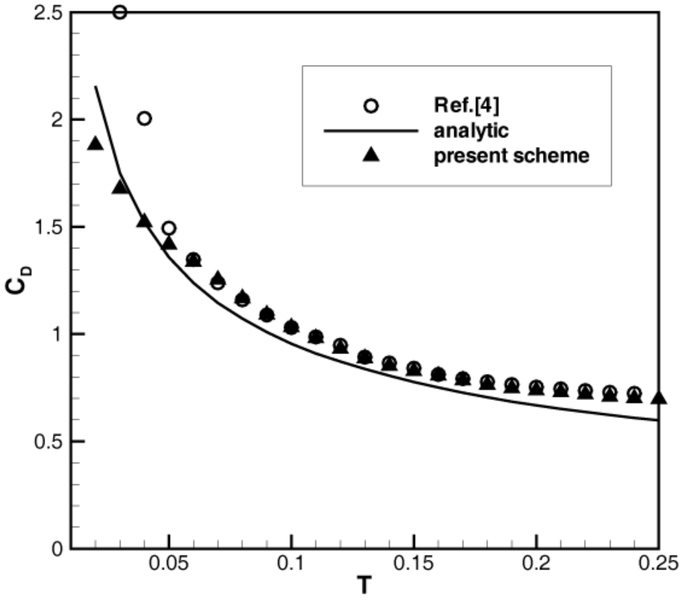

Figure 8.13 Comparison of C_D for the impulsively started cylinder problem ($0 < T < 0.25$). Solid line ($-$): analytical solution (Bar-Lev & Yang (1975)); ▲: Lagrangian vortex method (present scheme); □: Lagrangian vortex method (Ploumhans & Winckelmans (2000)).

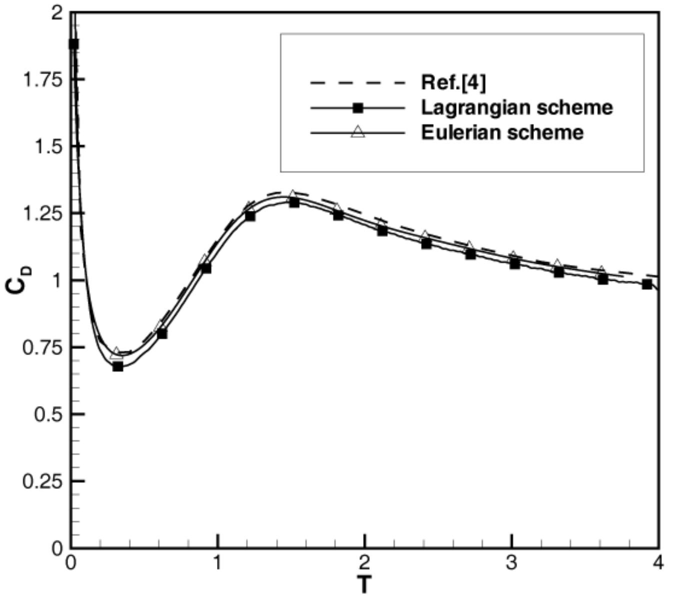

Figure 8.14 Comparison of C_D for the impulsively started cylinder problem ($0 < T < 4$). ■: Lagrangian vortex method; △: Eulerian FVM; dashed line($--$): Lagrangian vortex method (Ploumhans & Winckelmans (2000)).

Figure 8.15 represents the comparison of the body vorticity between the Eulerian FVM and the Lagrangian vortex method.

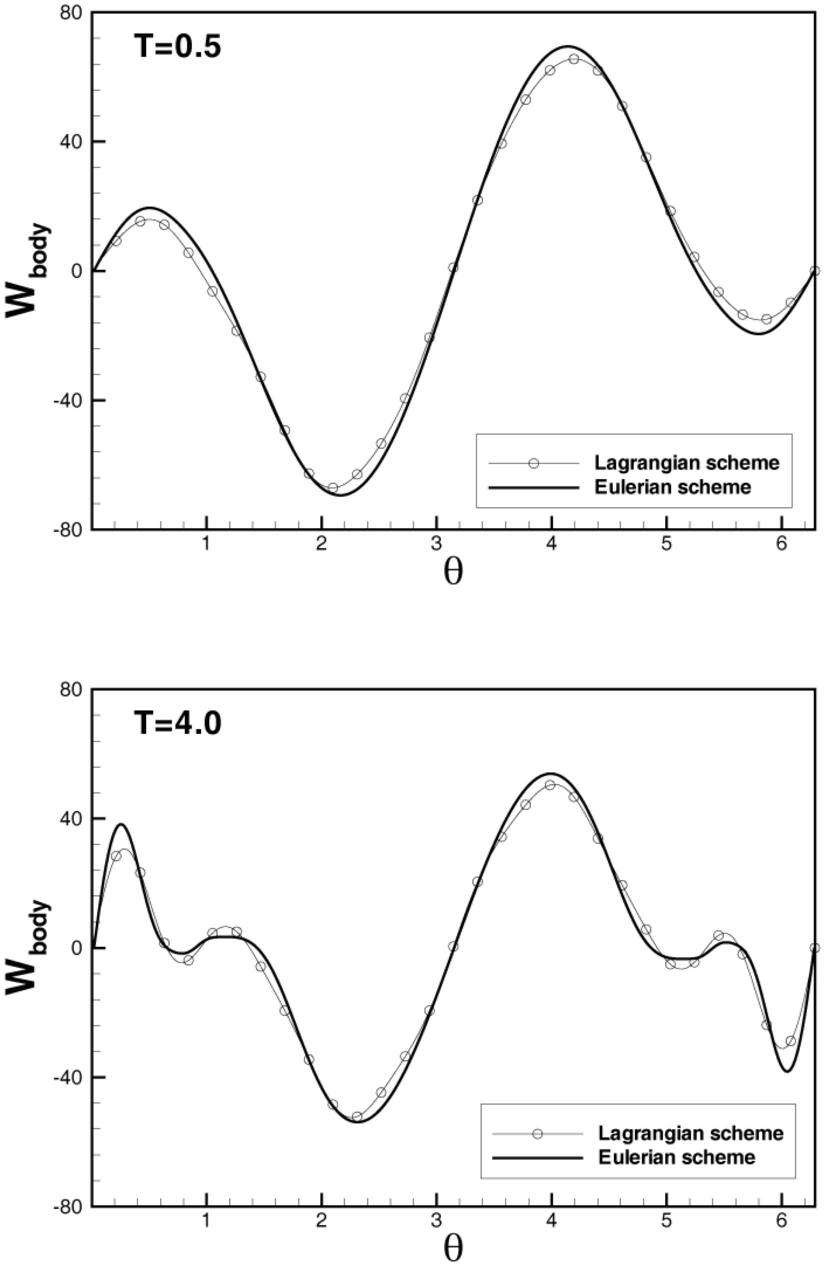

Figure 8.15 Comparison of the surface vorticity for the impulsively started cylinder problem for $Re = 550$ at $T = 0.5$ and $T = 4.0$. Solid line($-$): Eulerian FVM; $\circ$: Lagrangian vortex method.

The front stagnation point of the cylinder corresponds to the angular position of $\theta = \pi$ measured from the positive x-axis. The body vorticity obtained by the

Lagrangian vortex method is the 'filtered' (smoothed) value. The Lagrangian scheme has high-frequency noise in the values due to dispersed particles, so the filtered value is taken by an inverse Fourier transformation of the 16 first modes. The agreement between the two methods is seen to be quite satisfactory, but with small differences at local extrema. It is observed that, as time progresses, the local peaks of body vorticity become large. These local peaks occur at the instant the vortical wake behind the cylinder develops.

Figure 8.16 shows the streamline patterns. It is found that the wake length behind the cylinder is half the diameter of the cylinder at $T = 2$, and almost the same as the diameter at $T = 4$. At $T = 2$, a secondary vortex is generated at a position of about $\theta = 60^\circ$. The results obtained from the Lagrangian vortex method and the Eulerian FVM are found to be almost identical, but the Lagrangian scheme produces short wavelength oscillations at regions where there are few nearby particles.

Figure 8.17 presents a comparison of iso-contours of vorticity between the Lagrangian and Eulerian approaches. The agreement between the two is shown to be very good, except that the minimum and maximum values of ω differ slightly.

Figure 8.18 shows the pressure contours in the computational domain. The results from the two methods are almost identical. As time advances, the pressure distributions are rapidly changed near strong vortical flow structures. It is seen that a low pressure region is formed at the core of the downstream wake.

Figure 8.19 presents a comparison of pressure coefficients $C_P \left(\equiv \dfrac{p - p_\infty}{\rho\, q_\infty^2} \right)$ on the body surface at several instants. It is observed that the agreement between these results is satisfactory.

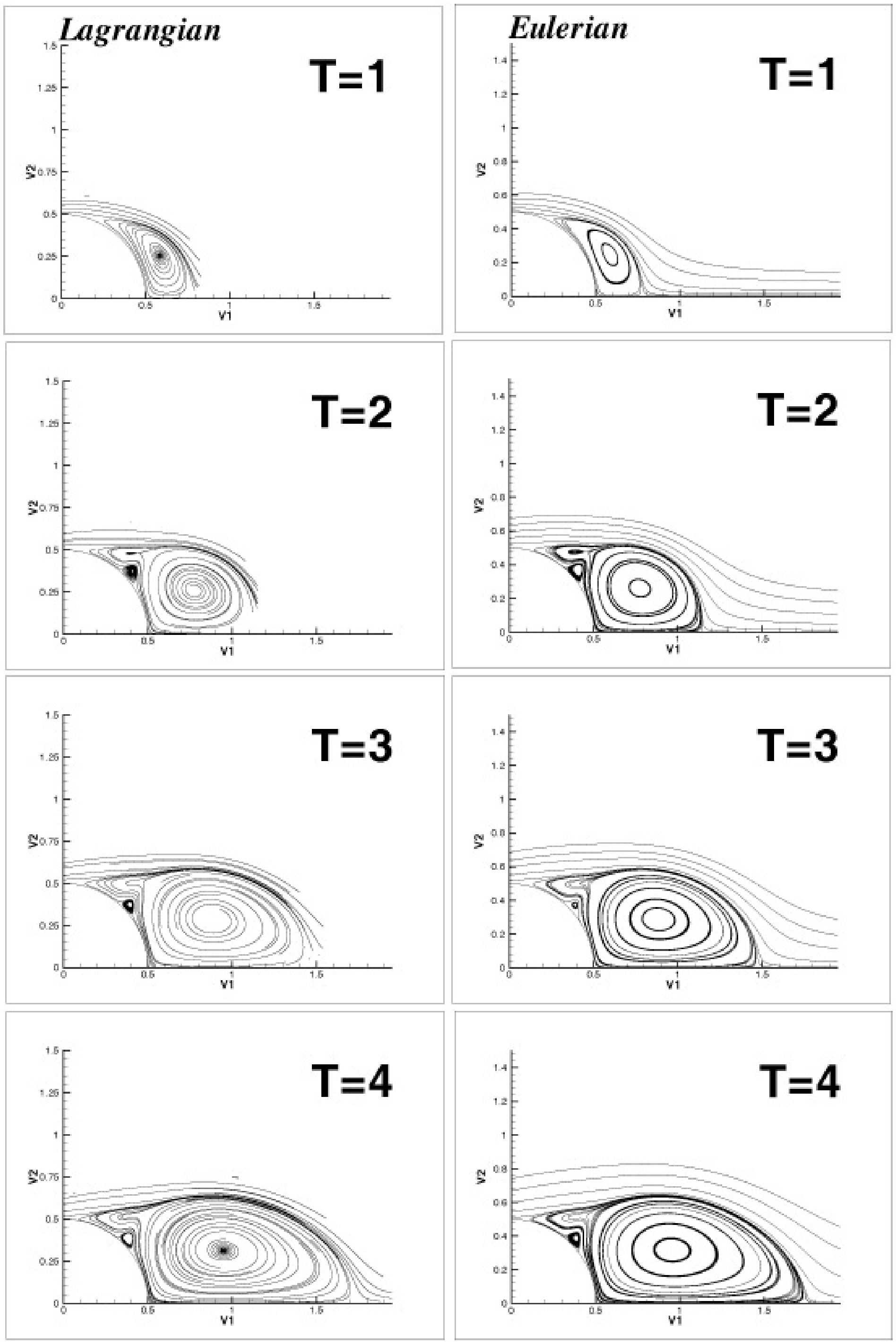

Figure 8.16 Comparison of the streamline patterns for the impulsively started cylinder problem for $Re = 550$ at $T = 1$, $T = 2$, $T = 3$ and $T = 4$. (left) Lagrangian vortex method; (right) Eulerian FVM.

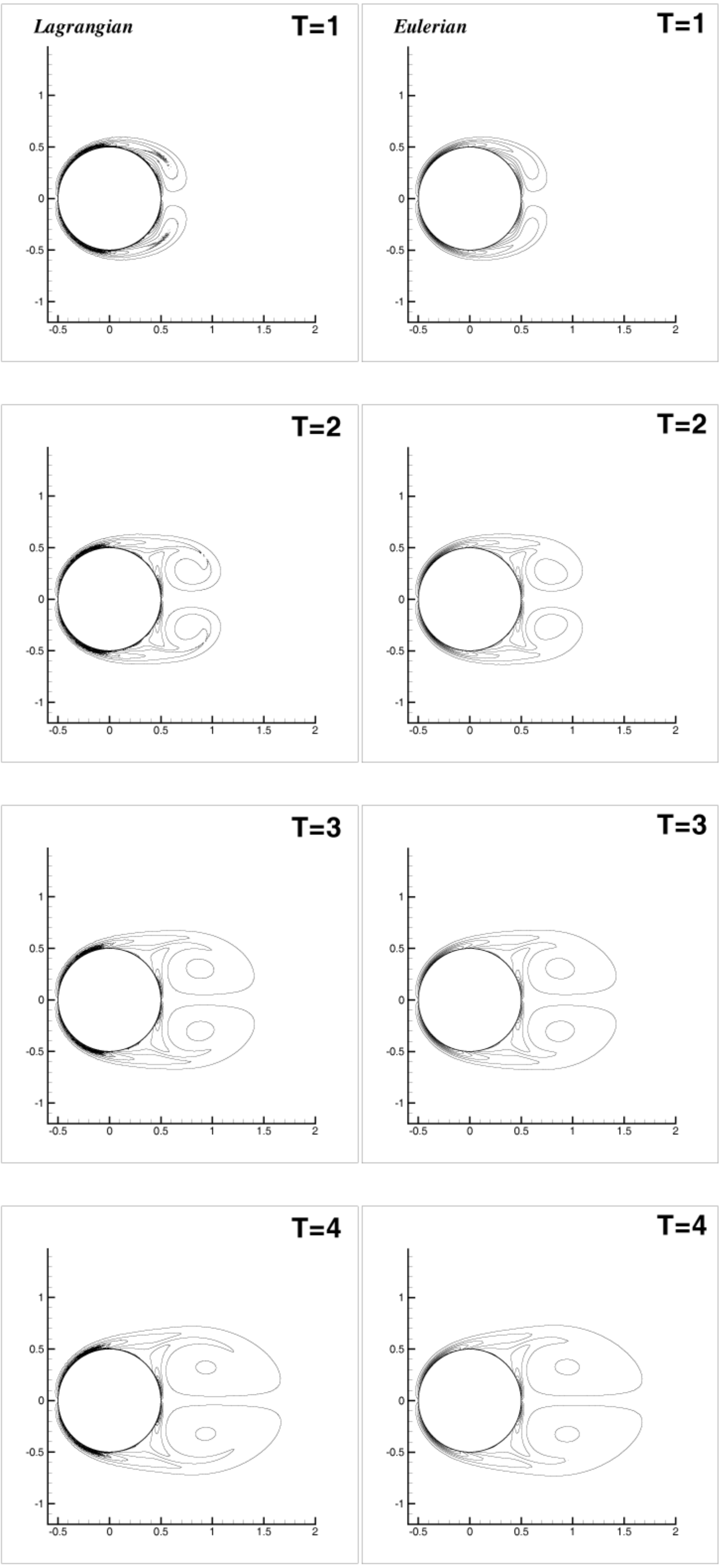

Figure 8.17 Comparison of the vorticity contours for the impulsively started cylinder problem for $Re = 550$ at $T = 1$, $T = 2$, $T = 3$ and $T = 4$. (left) Lagrangian vortex method; (right) Eulerian FVM.

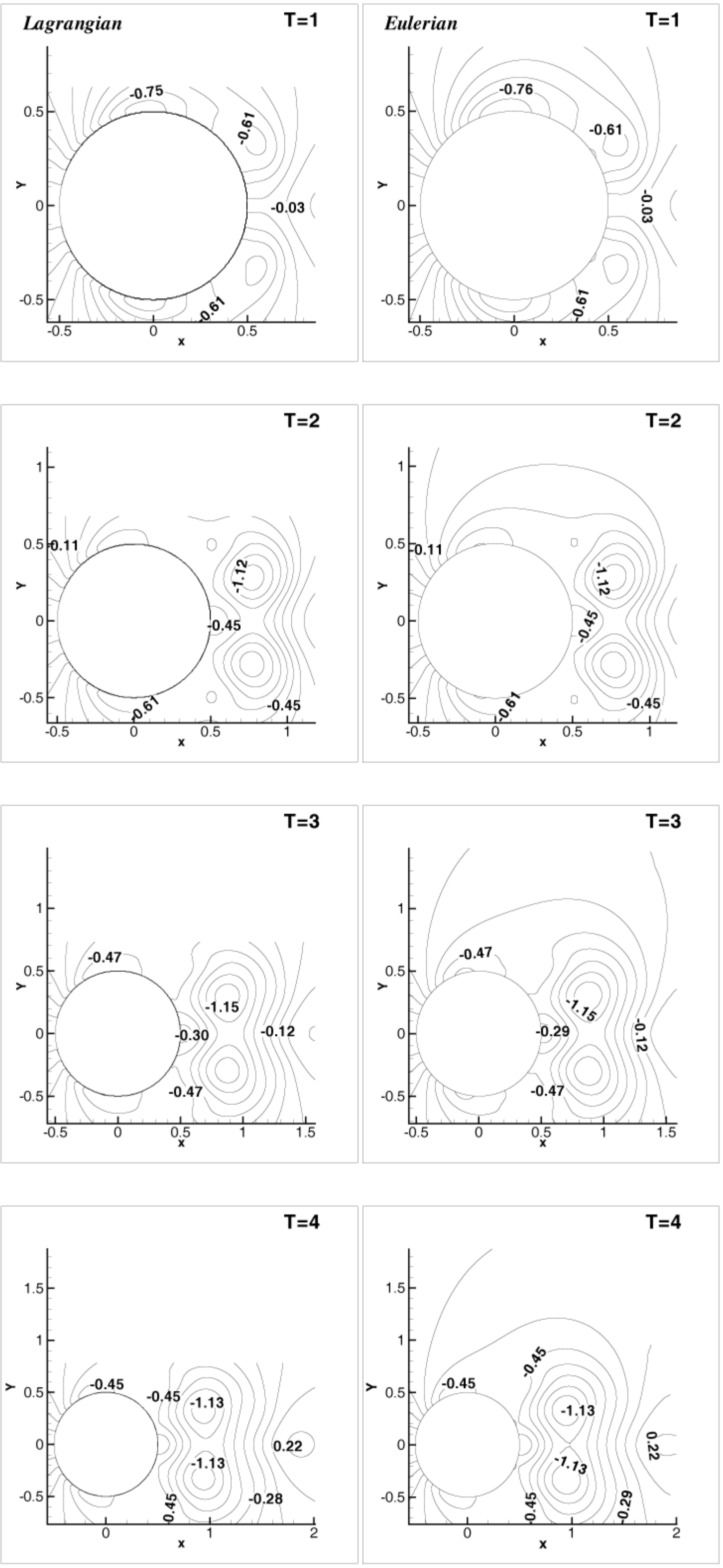

Figure 8.18 Comparison of the pressure contours for the impulsively started cylinder problem for $Re = 550$ at $T = 1.0$, $T = 2.0$, $T = 3.0$ and $T = 4.0$. (left) Lagrangian vortex method; (right) Eulerian FVM.

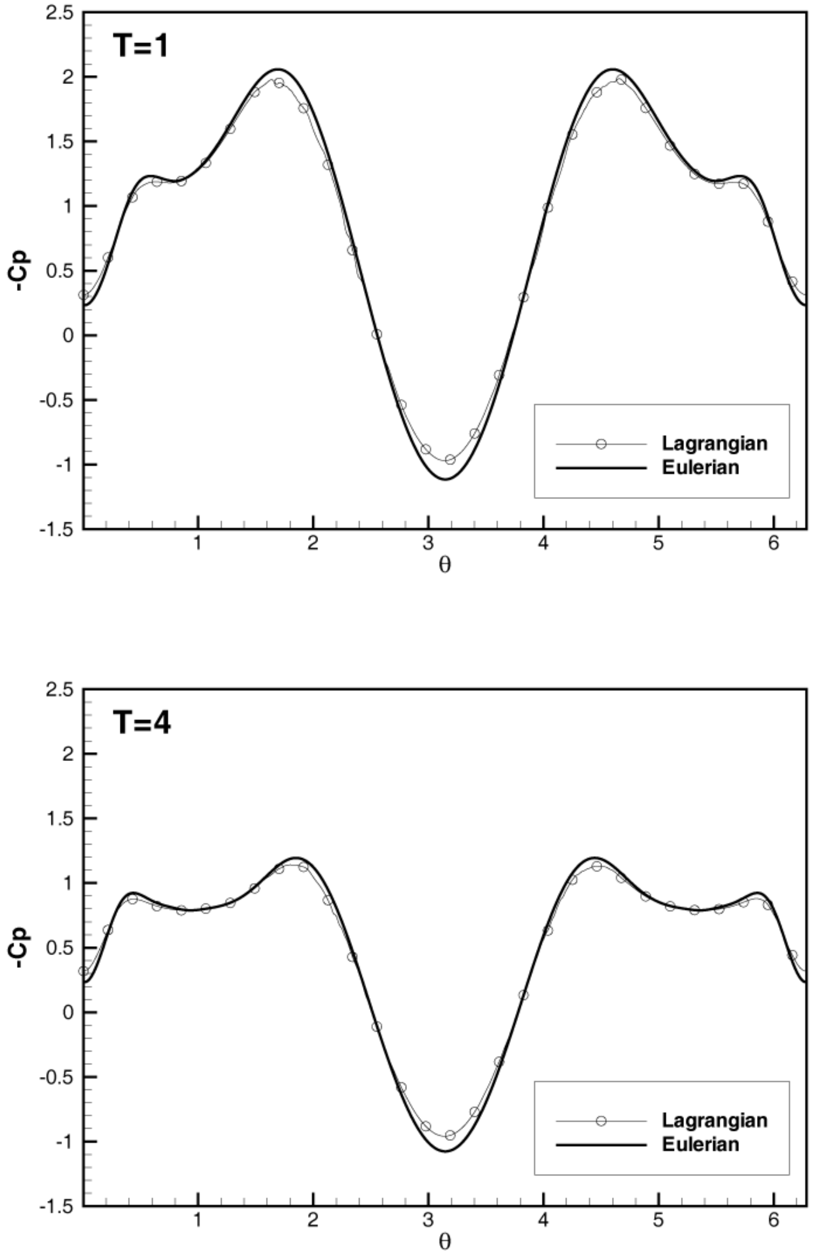

Figure 8.19 Comparison of C_p for the impulsively started cylinder problem for $Re = 550$ at $T = 1$ and $T = 4.0$. Solid line($-$): Eulerian FVM; Circle($\circ$): Lagrangian vortex method.

8.3.2 Impulsively started foil with varying angles of attack

We now take the case of the impulsively started NACA0021 with varying angles of attack. The present image particle layer scheme is suitable for this case. The parameters used in the calculation are similar to the case of the impulsively started cylinder (see Table 8.2).

Table 8.2 Parameters used in the numerical simulation of the flow around an impulsively started NACA 0021 hydrofoil.

	Eulerian FVM	Lagrangian vortex method
Reynolds number	550	550
Time step,Δt	0.01	0.01
Thickness ratio	0.21	0.21
Number of surface panels	408	408
Angle of attack	5°,10°	5°,10°
Grid meshes	408×60	·
Particles	·	$13000 \sim 40000$
Computational domain	3× chord	no limit
Computational time	about 31 hours	about 50 hours
(pentium IV)	(400 time steps)	(400 time steps)

A hydrofoil section of NACA0021 is chosen for the computation. It is a symmetrical hydrofoil whose thickness ratio is 21%. The thickness distribution for the NACA0021 is given in Abbott and Doenhoff (1958).

The parameters used in the simulation are $\Delta T = 0.01$ and $Re = 550$. The Reynolds number is based on the uniform flow velocity and chord length of the hydrofoil. There are 408 panels at body surface. The radius of all vortex particles has used with $\epsilon = 0.0025$. Image particles are located underneath body panels. Redistribution is done every five time steps. If new particle has $|\alpha| < 0.001\,|\alpha|_{max}$, it is deleted and the loss of circulation is redistributed equally among the remaining particles. The integration scheme for convection is a second order Adam-Bashforth (second order Runge-Kutta for the first step just after each redistribution). For diffusion, a first order Euler explicit scheme is used. A fast algorithm proposed by Greengard and Rohklin (1987), is used for both convection and diffusion substeps. After vorticity and velocity are updated through two fractional steps, the pressure equation is solved when needed.

Some experimental results were provided by Huang *et al.* (2001). His experiments were conducted in a towing water tank. The particle tracking flow visualization (PTFV) and the particle image velocimetry (PIV) were used to obtain a picture of vortex evolution on the suction surface of an impulsively started NACA 0012 hydrofoil. Five characteristic vortex evolution regimes are identified in the parameter domain of angle of attack.

The computing time is longer than in the case of the cylinder. The reason may be that the number of iterations required for canceling the spurious slip velocity and generating the vorticity flux on the body boundary is larger than that in the case of the cylinder problem. As the angle of attack is higher, the computing time is much longer. We applied the present scheme to the foil with two angles of attack, $5°$ and $10°$.

Figure 8.20 shows the streamline patterns, the vorticity contours and the pressure contours at Reynolds number 550 around the foil with angle of attack $5°$. The two results are shown to be in good agreement. In the streamline patterns, the reverse flows are captured near the trailing edge of the foil. As observed in the results of the Lagrangian vortex method, the fields of velocity and pressure are confined to the viscous region around the foil, because we consider only the field where the vorticity evolves and exists.

Figure 8.21 shows the streamline patterns, the vorticity contours and pressure contours at Reynolds number of 550 at $T = 4.0$ for the angle of attack of $10°$. This shows aspects similar to those of the previous case.

Figure 8.22 and Figure 8.23 show the comparison of the drag coefficients and the lift coefficients. In the case of angle of attack $5°$, the results of Lagrangian vortex and Eulerian FVM methods are nearly identical.

On the other hand, in the case of angle of attack $10°$, there is a small difference between the results, especially at about $T = 3.0$. This may be due to the strong starting vortex. When the angle of attack of the foil is higher, the strength of the starting vortex is larger. Each scheme may reflect the evolution of the vorticity on the body in a different manner. In fact, we only focus on the unsteady flow simulation at an early stage. We may expect to obtain the same steady-state characteristics.

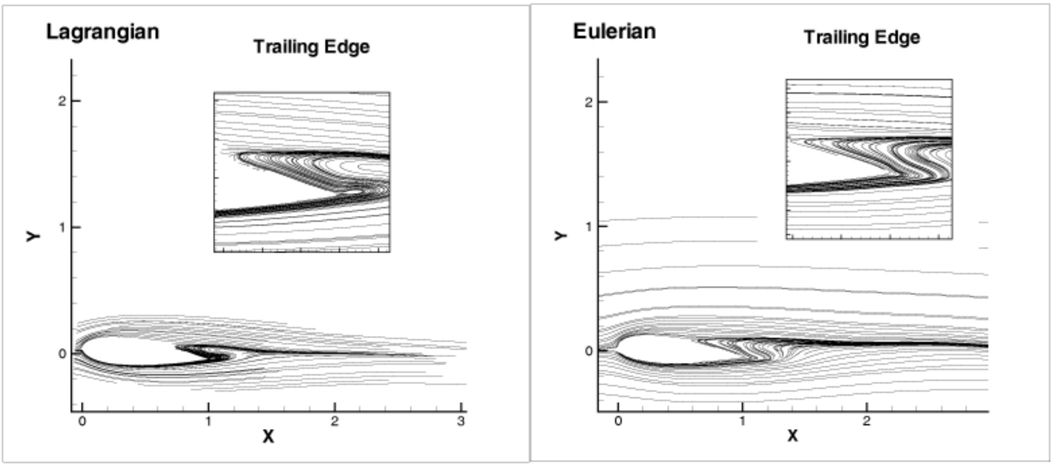

(a) Streamlines

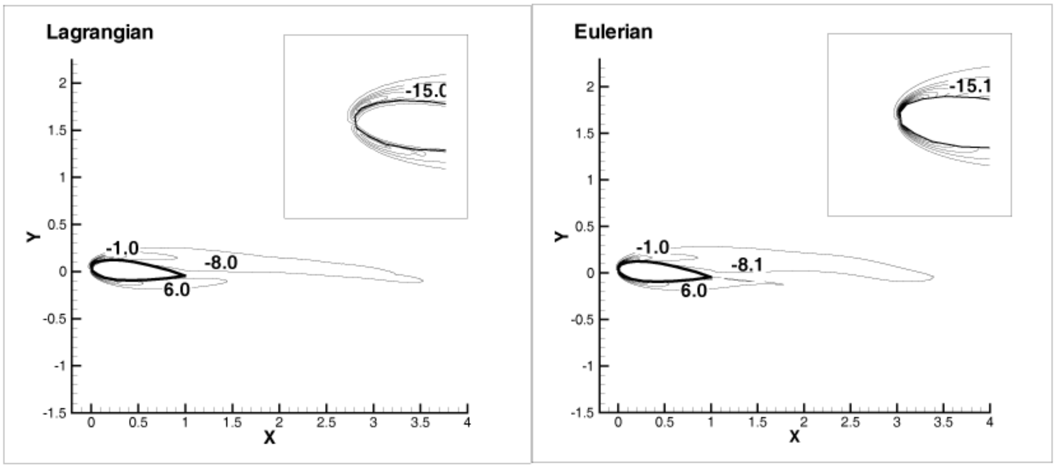

(b) Vorticity

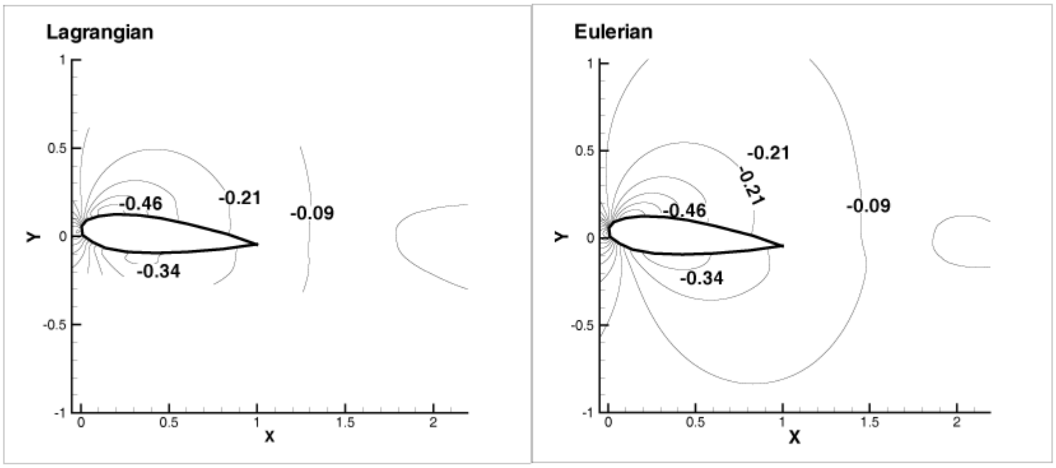

(c) Pressure

Figure 8.20 Streamline patterns, vorticity contours and pressure contours for the impulsively started NACA0021 at $Re = 550$, $\alpha = 5°$ and $T = 4.0$. (left) Lagrangian vortex method; (right) Eulerian FVM.

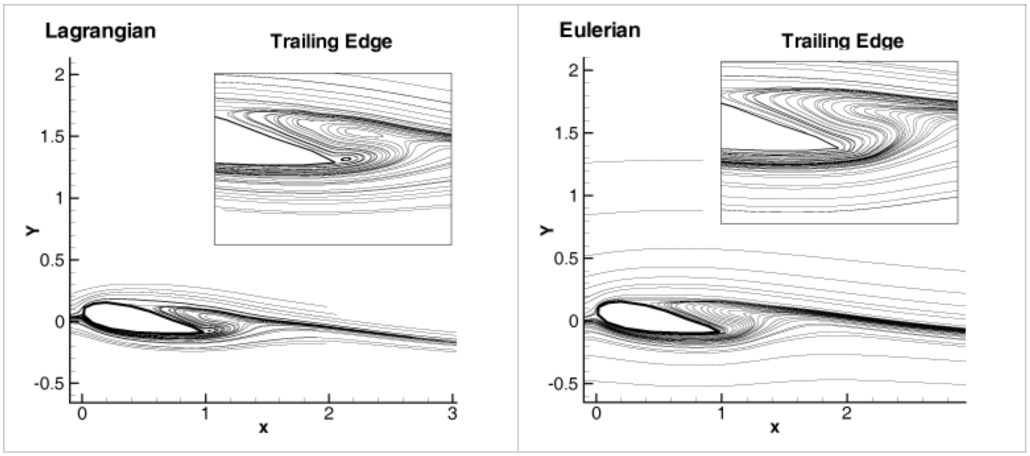

(a) Streamlines

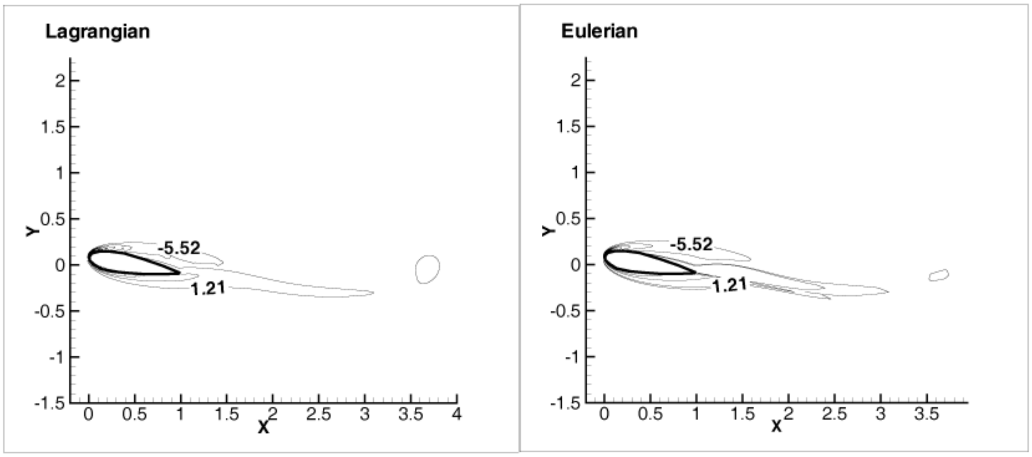

(b) Vorticity

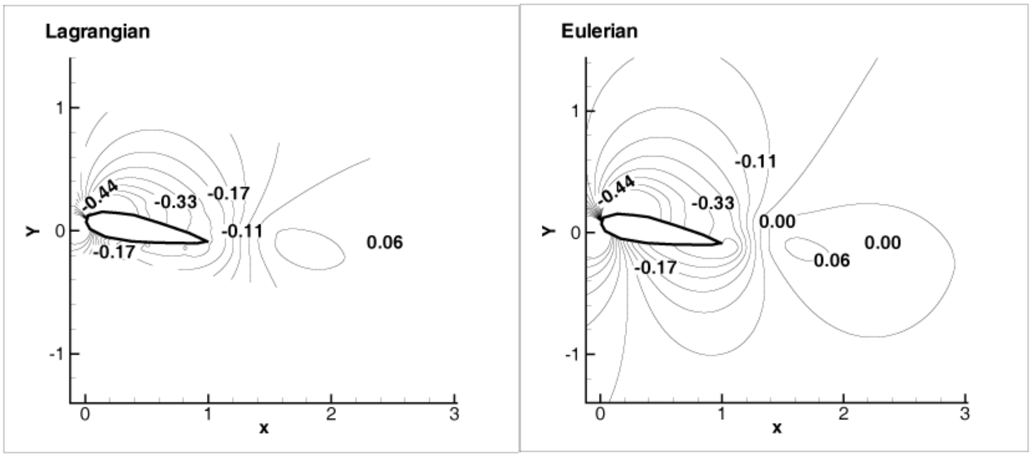

(c) Pressure

Figure 8.21 Streamline patterns, vorticity contours and pressure contours for the impulsively started NACA0021 foil at $Re = 550$, $\alpha = 10°$ and $T = 4.0$. (left): Lagrangian vortex method; (right): Eulerian FVM.

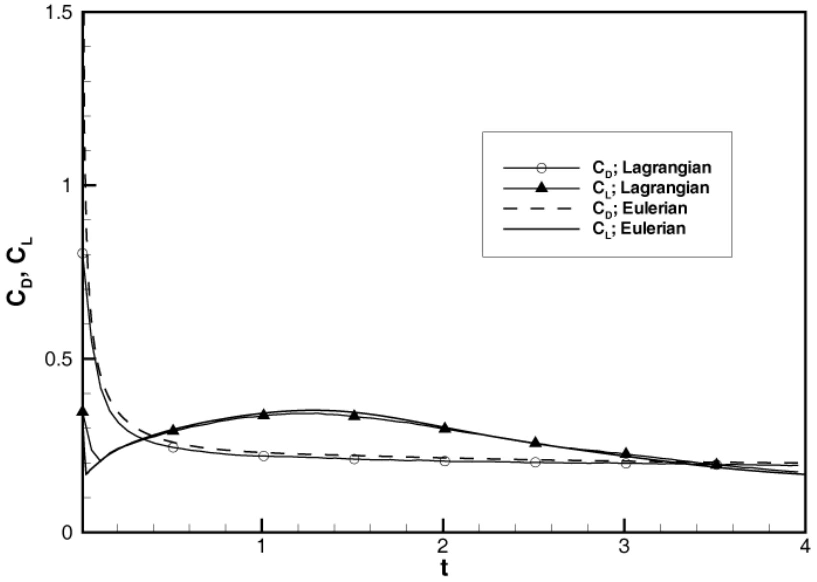

Figure 8.22 Comparison of drag and lift for the impulsively started NACA0021 foil at $Re = 550$ and $\alpha = 5$. ○: C_D by Lagrangian vortex method; ▲: C_L by Lagrangian vortex method; dashed line(−−): C_D by Eulerian FVM; solid line(−): C_L by Eulerian FVM.

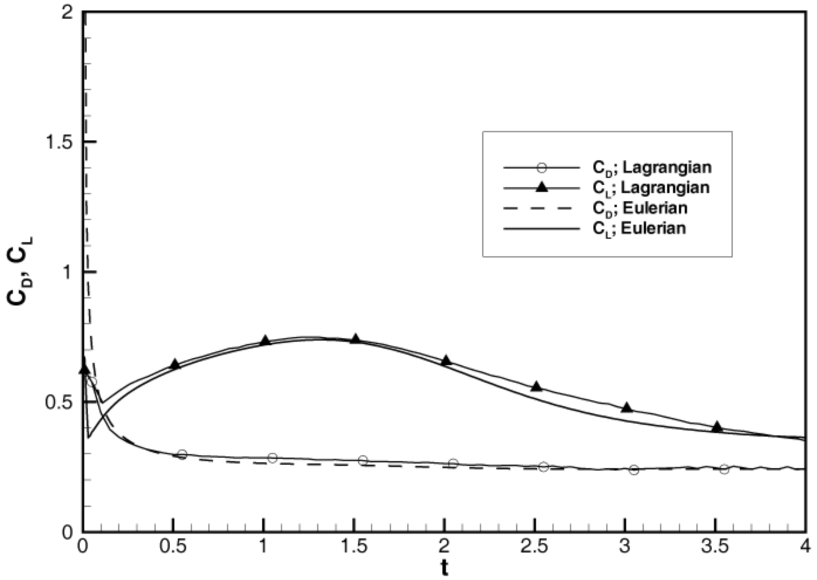

Figure 8.23 Comparison of drag and lift for the impulsively started NACA0021 foil at $Re = 550$ and $\alpha = 10$. ○: C_D by Lagrangian vortex method; ▲: C_L by Lagrangian vortex method; dashed line(−−): C_D by Eulerian FVM; solid line(−): C_L by Eulerian FVM.

8.3.2.1 Angle of attack : 90 deg.

At very large angles of attack, the bluff body effect becomes dominant. The starting vortex is generated from both the leading and the trailing edges. The vortex evolving from the sharp trailing edge appears to be a little larger than one from the leading edge. The corresponding results are shown in Figures **8.24** , **8.25** , and **8.26** .

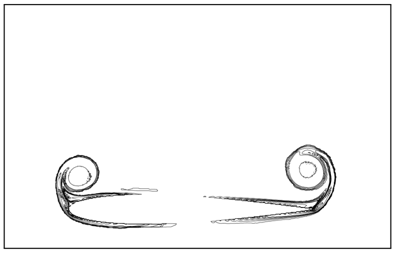

(a) $T = 0.250$

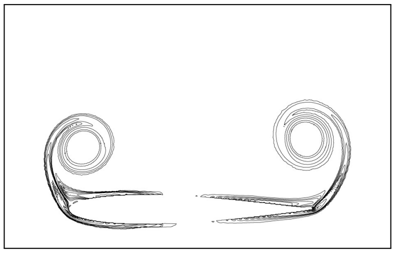

(b) $T = 0.500$

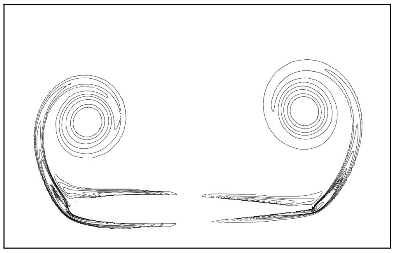

(c) $T = 0.750$

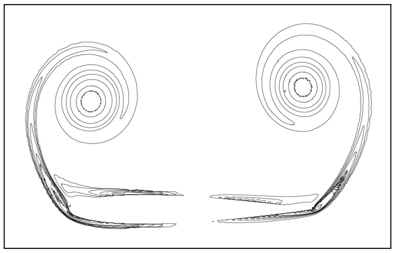

(d) $T = 1.000$

Figure 8.24 Iso-contours of vorticity around NACA 0012 hydrofoil at $\alpha = 90^o$ and $Re = 1200$.

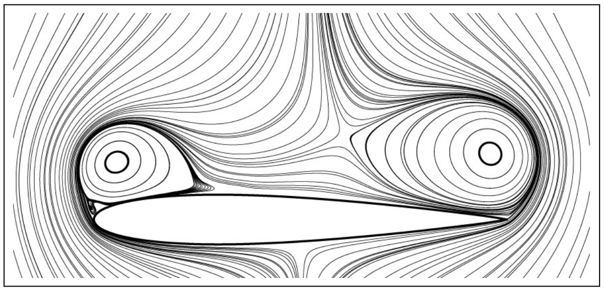

(a) $T = 0.250$

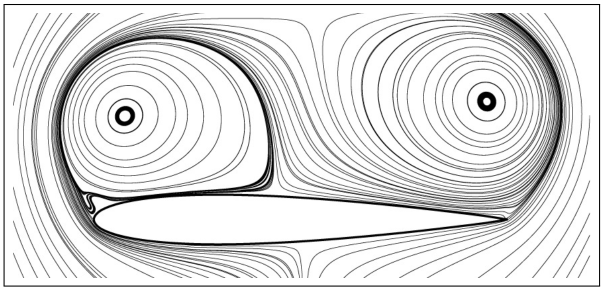

(b) $T = 0.500$

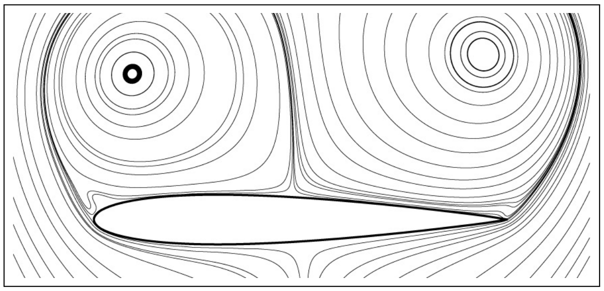

(c) $T = 0.750$

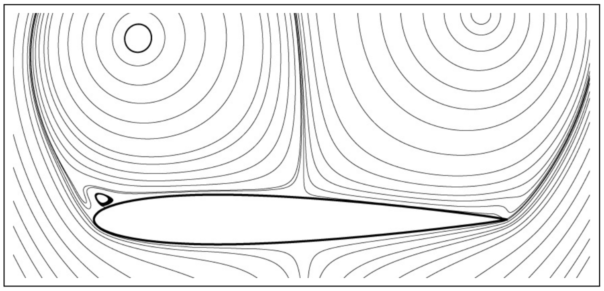

(d) $T = 1.000$

Figure 8.25 Streamlines around NACA 0012 hydrofoil at $\alpha = 90^o$ and $Re = 1200$.

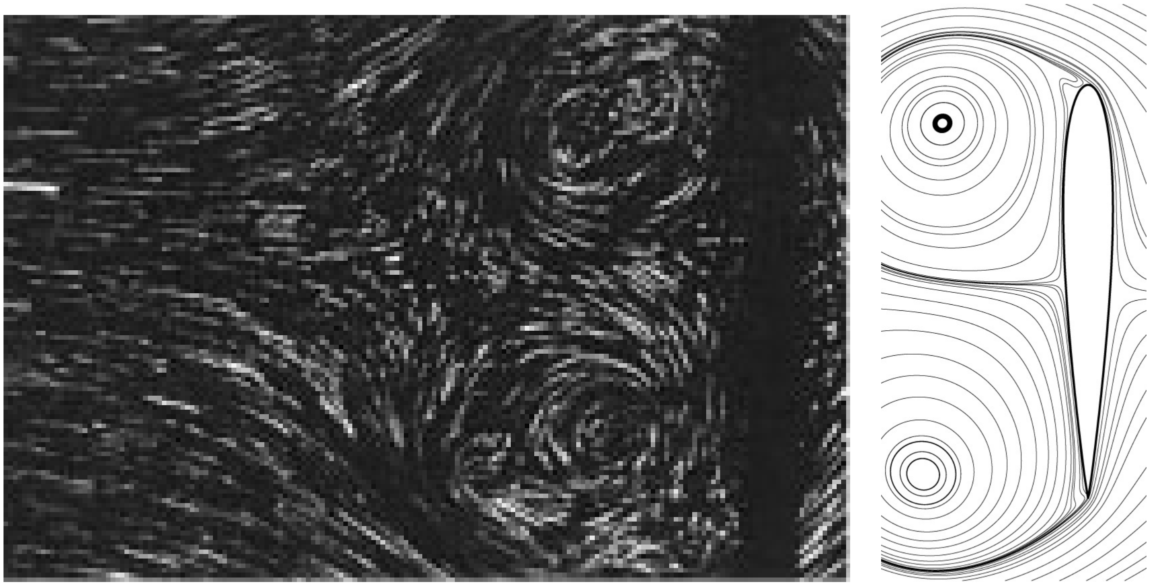

(a) $T = 0.786$ (b) $T = 0.750$

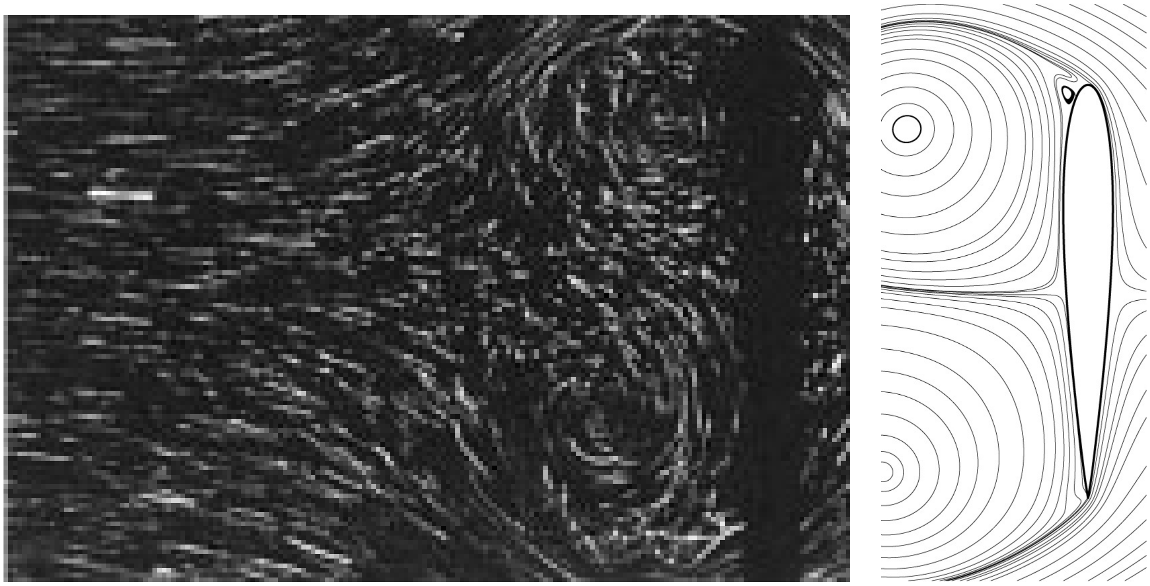

(c) $T = 1.048$ (d) $T = 1.000$

Figure 8.26 Comparison of the streamlines around NACA 0012 hydrofoil with the experimetal result (Huang *et al.* 2001) at $\alpha = 90^o$ and $Re = 1200$.

8.4 Vortex-In-Cell Methods

8.4.1 Introduction

The computation of velocity and stretching is realized through the vector potential and vorticity formulation on the immersed Cartesian grid. The present method is similar to the immersed boundary vortex-in-cell method by Cottet and Poncet (2003) in terms of the use of unified interpolation formulas. But, the use of panel method makes it possible to impose both the no through flow condition and no slip condition on the body surface. The vorticity flux from the panel satisfies the no slip condition and the singularity distribution over the panel does not make the flow across the body surface. The panel method is set up on the triangular discretization of the body surface and linear distribution of the singularities on the panel. The implementation has advantages over constant strength method that eliminates the discontinuities of singularities between panels and reduces the size of matrix elements as well. In the present method, the panel method is also utilized for the calculation of pressure field. The inversion result of the influence coefficient matrix can be adopted without any modification due to the integral equation formulation for the pressure.

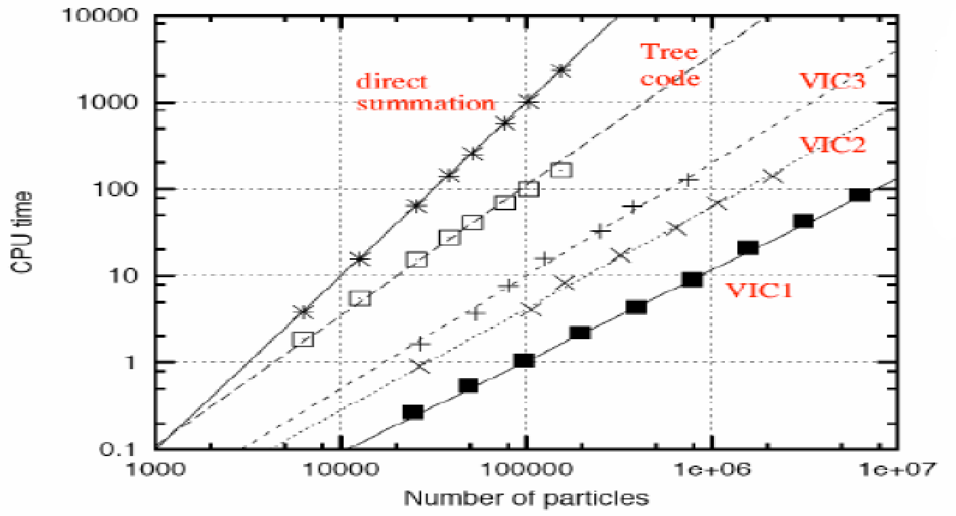

Figure 8.27 Comparison of CPU times for velocity evaluations in 3-D. Krasny tree-code vs. VIC with Fishpack and 64 points interpolation formulas. VIC1: Cartersian grid with 100 % particles; VIC2: Polar grid with 65 % particles; VIC3: Polar grid with 25 % particles. From Cottet (1999).

8.4.2 Rotational velocity component: FFT scheme based on regular grid

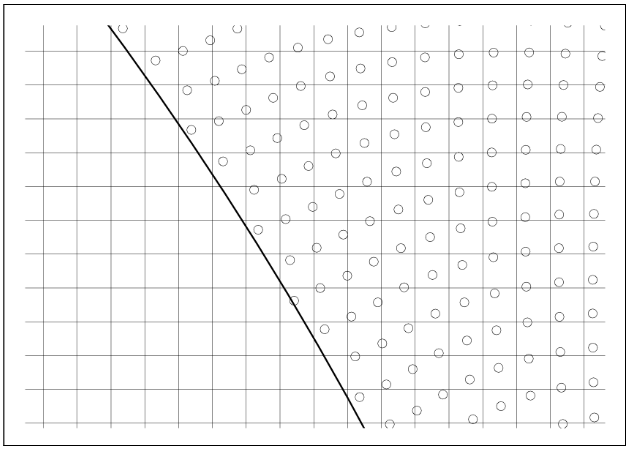

(a) Before particle strength assignment on the grid

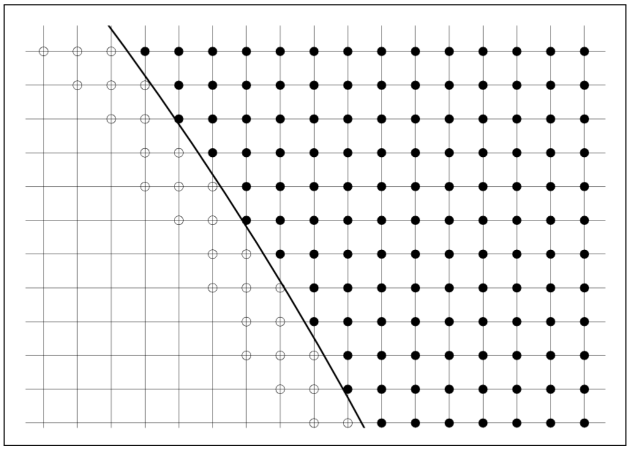

(b) After assignment, strengths assigned onto hollow circle inside body are reserved for PSE

Figure 8.28 Regular immersed grids for FFT.

The present work uses FFT based Poisson solver to calculate rotational velocity field. A regular Cartesian grid is placed so that the grid compactly encloses the vortex particles including the body. The grid is immersed in the body, and the vorticity field is extended so that vorticity has zero value on the grid inside the body. The vorticity of the particles is distributed to the Cartesian grid by the interpolation formula,

$$\underline{\omega}_g = \frac{1}{V_p} \sum_{p}^{N} \underline{\alpha}_p W\left(\frac{x_p - x_g}{h}\right) W\left(\frac{y_p - y_g}{h}\right) W\left(\frac{z_p - z_g}{h}\right) \tag{8.66}$$

where g and p are subscripts for grid and particle quantities, respectively, and $W(x)$ is the interpolation kernel. In the present work the third order M_4' kernel is chosen. The kernel is defined by

$$W(x) = M_4'(x) = \begin{cases} 1 - \frac{5}{2}\,|x|^2 + \frac{3}{2}\,|x|^3, & \text{for} \quad |x| \leq 1 \\ \frac{1}{2}\,(2 - |x|)^2\,(1 - |x|), & \text{for} \quad 1 < |x| < 2 \\ 0, & \text{for} \quad |x| \geq 2 \end{cases} \tag{8.67}$$

The kernel preserves the first three moments of the distribution, the total, linear and angular impulse of the fields, twice continuously differentiable and symmetric. The VIC method needs regridding of particles on regular locations on occasion to preserve the accuracy, and the kernel is also used for the regular distribution of the distorted particles.

After the interpolation step the Poisson equation for vector potential is solved by following the procedure which is introduced as Fourier transform method in the book "*Numerical Recipes in C*". Here the procedure is briefly recited for the two dimensional Poisson equation $\nabla^2\psi = -\omega$ with Dirichlet boundary condition. The finite difference representation of the equation is, approximating the Laplacian via the second order central difference scheme,

$$\frac{\psi_{i+1,j} - 2\,\psi_{i,j} + \psi_{i-1,j}}{h^2} + \frac{\psi_{i,j+1} - 2\,\psi_{i,j} + \psi_{i,j-1}}{h^2} = -\omega_{i,j} \tag{8.68}$$

where $\psi_{i,j}$ represents function value at a point (x_i, y_j) and h is grid spacing. If we substitute the discrete inverse sine transforms,

$$\psi_{i,j} = \frac{2}{IJ} \sum_{m=1}^{I-1} \sum_{n=1}^{J-1} \hat{\psi}_{m,n}\, \sin\frac{\pi i m}{I}\, \sin\frac{\pi j n}{J} \tag{8.69}$$

$$\omega_{i,j} = \frac{2}{IJ} \sum_{m=1}^{I-1} \sum_{n=1}^{J-1} \hat{\omega}_{m,n}\, \sin\frac{\pi i m}{I}\, \sin\frac{\pi j n}{J} \tag{8.70}$$

in the finite difference equation (8.68), we can get the relation between Fourier coefficients,

$$\hat{\psi}_{m,n} = \frac{h^2\,\hat{\omega}_{m,n}}{2\left(\cos\dfrac{\pi m}{I} + \cos\dfrac{\pi n}{J} - 2\right)} \tag{8.71}$$

We can get $\psi_{i,j}$ on the regular grid by the inverse sine transform (8.69).

In 3-D, the inverse sine transform has one more term and the relation between Fourier coefficients becomes similar form,

$$\hat{\psi}_{l,m,n} = \frac{h^2\,\hat{\omega}_{l,m,n}}{2\left(\cos\dfrac{\pi l}{I} + \cos\dfrac{\pi m}{J} + \cos\dfrac{\pi n}{K} - 3\right)} \tag{8.72}$$

Above procedure was explained for homogeneous Dirichlet condition at boundary. As the grid is set up so that it tightly includes the particles, the values of $\underline{\psi}$ on the sides of the VIC grid become non trivial. When the boundary values of $\underline{\psi}$ are known, the procedure can be simply modified by taking them over to the right-hand side. If we write the solution as $\psi = \psi' + \psi^B$, where $\psi' = 0$ on the boundary, while ψ^B has nonzero values only on the boundary, which is the given boundary value, the finite difference equation (8.68) becomes equivalent to the case of zero boundary condition. The equation for a boundary takes the form, say for $i = I - 1$,

$$\psi'_{I,j} + \psi'_{I-2,j} + \psi'_{I-1,j+1} + \psi'_{I-1,j-1} - 4\,\psi'_{I-1,j} = h^2\,\omega_{I-1,j} - \psi^B_{I,j} \tag{8.73}$$

so whenever the boundary value is non-zero, the source term $h^2\,\omega_{I-1,j}$(be careful that one grid inside from boundary) is replaced by

$$h^2\,\omega_{I-1,j} - \psi^B_{I,j} \tag{8.74}$$

The values on the boundary is evaluated using the expression (8.23) by fast algorithm developed by Kim (2003). If the boundary is located far from the particle positions, the homogeneous boundary condition may be used, but this approach involves too much grid and the advantage of using compact grid cannot be taken.

The velocity on the grid is computed by fourth order finite difference method from the definition $\underline{u}_\omega = \nabla \times \underline{\psi}$, for example, the component u is

$$\begin{aligned} u &= \frac{\partial \psi_z}{\partial y} - \frac{\partial \psi_y}{\partial z} \\ &= \frac{\psi_{z_{i,j-2,k}} - 8\,\psi_{z_{i,j-1,k}} + 8\,\psi_{z_{i,j+1,k}} - \psi_{z_{i,j+2,k}}}{12\,h} \\ &\quad - \frac{\psi_{y_{i,j,k-2}} - 8\,\psi_{y_{i,j,k-1}} + 8\,\psi_{y_{i,j,k+1}} - \psi_{y_{i,j,k+2}}}{12\,h} \end{aligned} \tag{8.75}$$

The velocity on the particle position is then interpolated from the velocities of the grid. The same interpolation formula M_4' is used. The velocity on the grid very close to the body can have singular behavior since sub-grid scale can have a significant effect when applying finite difference formula. The velocity at such a point is directly evaluated using the Biot-Savart formula. The points are found by a criteria that the distance from the body is less than half of the grid size.

8.4.3 Potential velocity component: Panel method with linearly varying singularity distribution

For the solution of the Laplace equation $\nabla^2 \phi = 0$, the identity with a distribution of singularities on the surface is applied to the discretized surface so that the strengths of them determined by the boundary condition. This technique is known as the popular 'panel method'. The no through flow condition is employed to points on the surface, unlike Cottet & Poncet (2003)'s method. Figure 8.29 shows the difference between Cottet & Poncet (2003) and the present work in handling no through flow condition.

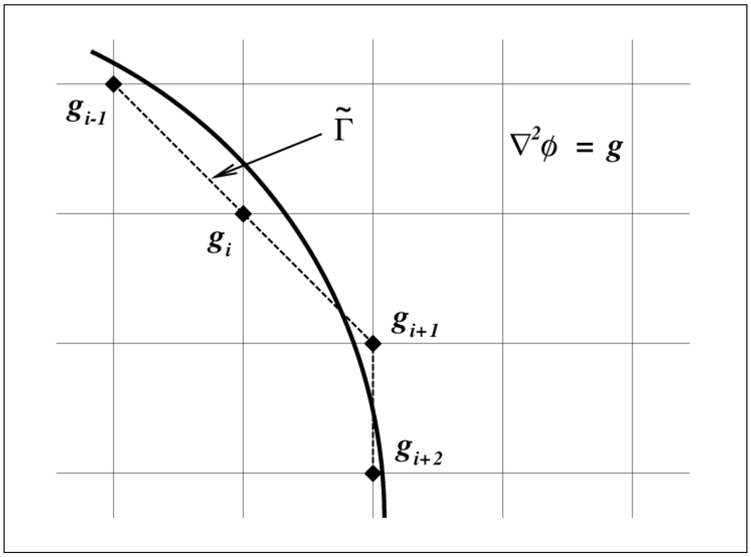

(a) Immersed boundary VIC, Cottet & Poncet (2003)

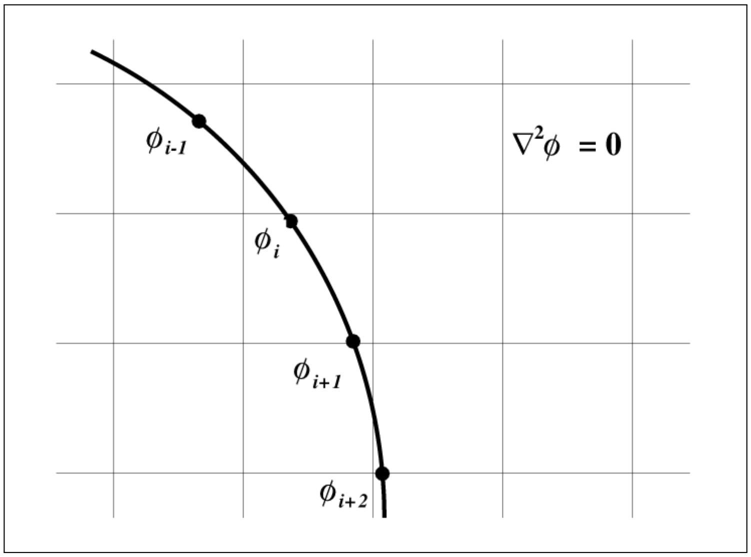

(b) Present work

Figure 8.29 Two types for enforcement of the no-penetration flow condition in the regular grid system.

The present method is extended in the context of the VIC of this work to a linear distribution of singularities on a triangular panel. This choice is more flexible, since surface of a complex geometry can be more uniformly discretized with triangular elements. Furthermore, the discontinuity of the singularities, which is present between panels in constant strength panel method, can be avoided with the linear variation. And, as the number of panels becomes approximately twice that of the vertices, it would be a great benefit that the unknowns in the resulting system of linear equations can be notably decreased with the unknowns defined on the panel vertices.

The Green's scalar identity expresses the potential ϕ within the fluid domain as a sum of each contribution in terms of the surface value of ϕ and its normal derivative $\underline{n} \cdot \nabla\phi$ on each panel of the discretized boundary surface S_i,

$$\phi(\underline{x}) = -\frac{1}{4\pi}\sum_i \iint_{S_i} \left\{ \frac{1}{r}\, \underline{n} \cdot \nabla_\xi \phi - \phi(\underline{\xi})\, \underline{n} \cdot \nabla_\xi \left(\frac{1}{r}\right) \right\} dS_\xi \tag{8.76}$$

where $\phi(\xi)$ is the surface distribution of doublets, and $\underline{n} \cdot \nabla_\xi$ is that of sources. The strength of source σ corresponds to the no through flow boundary condition,

$$\sigma = \underline{n} \cdot \nabla_\xi \phi = -\underline{n} \cdot (\underline{\mathrm{U}}_\infty + \underline{u}_\omega) \tag{8.77}$$

If the equation (8.76) is discretely applied for each vertex with the surface integrals evaluated assuming that the source and doublet are linearly distributed on each panel, we can get the linear system of algebraic equations.

$$(1 + D_{kk})\,\phi_k - \sum_{m=1}^{N-(k)} \phi_m\, D_{km} = \sigma_k\, E_{kk} + \sum_{m=1}^{N-(k)} \sigma_m\, E_{km} \tag{8.78}$$

$$D_{km} = \sum_{n=1}^{L_m} \frac{1}{4\pi} \iint_{S_m} \underline{n} \cdot \nabla \left(\frac{1}{r}\right) dS_\xi$$

$$E_{km} = \sum_{n=1}^{L_m} \frac{1}{4\pi} \iint_{S_m} \frac{1}{r}\, dS_\xi$$

where L_m is the number of panels which have the vertex m in common. D_{kk} and E_{kk} are the special case that the field point coincides with the source point. Due to the linear distribution of the singularities, it should sum up all the contributions from each panel when the surface integral is calculated. As shown in Figure **8.30** , when the induced potential is calculated at the point k by the unit strength on m, all the panels filled with gray should be involved with the other nodes having value zero.

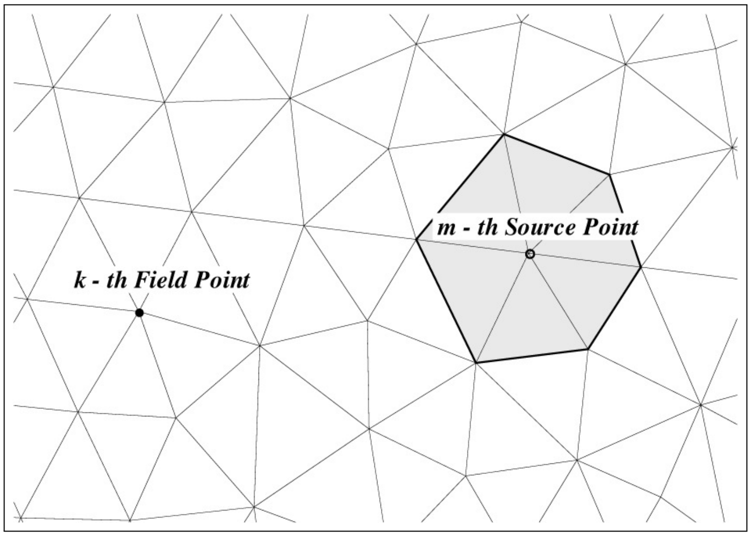

Figure **8.30** Schematic arrangement of a field point k due to a singularity distribution element composed of several triangular panels. There is a linear variation of the singularity density over each panel with unit strength at a source point m and zero strength on other neighboring points of the element.

The surface integrations are evaluated using explicit simple analytic expressions for the linear distributions derived by Suh (1992). The expressions are line integrals along the contour of the panel, which can be easily evaluated with global coordinates.

The slip velocity induced by the singularity distribution exist on the surface of the body. This component equivalently becomes the strength of the vortex sheet, which will be diffused in the field for the satisfaction of the no slip condition.

$$\Delta\underline{\gamma} = \underline{n} \times \underline{q}_s = \underline{n} \times (\underline{U}_\infty + \underline{u}_\omega + \nabla\phi) \tag{8.79}$$

The velocity field is finally corrected by superimposing the potential component, $\underline{u}_\phi(\underline{x}) = \nabla\phi(\underline{x})$, which can be calculated by the similar integration formula, with the solution of linear system (8.78),

$$\underline{u}_\phi(\underline{x}) = \frac{1}{4\pi}\sum_i \iint_{S_i} \left\{ \phi(\underline{\xi}) \left(\frac{\underline{n}}{r^3} - 3\,\frac{\underline{n}\cdot\underline{r}}{r^5}\,\underline{r} \right) + (\underline{n}\cdot\nabla_\xi\phi)\,\frac{\underline{r}}{r^3} \right\} dS_\xi \tag{8.80}$$

One advantage can be obtained that the pressure field can be computed with the similar procedure when the panel method is selected as a method to satisfy no through flow condtion. As it will be described in the subsequent section, the integral equation for pressure Eq. (6.41) is very similar to the scalar identity, except with the one additional term that involves a volume integral of the cross product of velocity and vorticity. In system of the resulting linear equations, the right hand side only would be different, so we can directly use the inversion result of the same matrix.

8.4.4 Stretching term in 3-D

In a VIC method the grid values of velocities and vorticities can be directly used for finite differencing in the stretching when they are interpolated onto the grid. Furthermore, a VIC method can have an advantage of being conservative on the grid, if the conservative form $\nabla \cdot (\underline{\omega}\, \underline{u})$ of the stretching term is implemented.

In order to treat the stretching term, the vorticity and velocity are first multiplied on the grid, the divergence is then computed by 4th order finite difference formula and interpolated on the particle locations along with the velocity.

8.4.5 Stability issue

Although the vortex method demands more loose stability condition than classical CFL type condition due to the Lagrangina advection of the particle, there exist stability criteria constrained by the explicit diffusion solver with PSE ($\nu\, \delta t \leq C\, h^{-2}$) and by the strain of the flow ($\Delta t \leq C\, |\nabla u|^{-1}$). Even though these conditions are fulfilled, the current study experienced an unstable behavior of solution, when the method is applied to the simulation of flow past a rectangular wing, if the particle core size(smoothing parameter) or time step does not meet the condition for the conservation of vortex strength in wall diffusion,

$$\epsilon < \sqrt{2\, \nu\, \Delta t} = \sqrt{\frac{2\Delta t}{Re}}, \tag{8.81}$$

where $Re = \dfrac{UL}{\nu}$ $(U = L = 1)$. The particle size should be made small as the Reynolds number of the flow increases. Figure **8.31** shows the behavior of the maximum residual slip when the vortex sheet diffusion to the initial particle layer is iterated with the change of the particle strength. The vortex sheet is firstly evaluated from the potential flow of the impulsive start. As shown in the figure, the residual slip increases with the parameters $\epsilon = 0.008633$, $\Delta t = 0.005$ when the Reynolds number is $Re = 200$. This choice of paramters resulted eventually in unstable solution, as $0.008633 > \sqrt{2 \times 0.005 \times 0.005} = 0.007071$. The computations of flow past a rectangular wing are performed with the appropriate selection of the parameters. However, the condition does not necessarily need to be satisfied for the simulation of flow past a sphere.

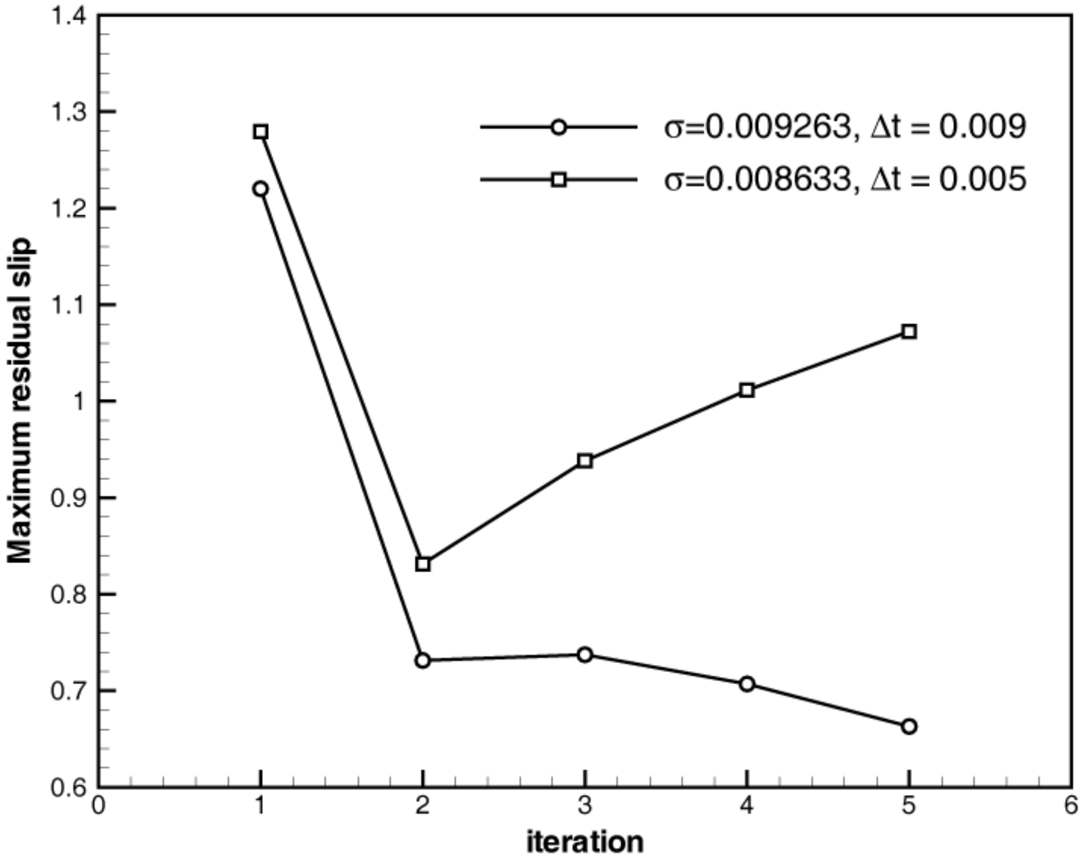

Figure 8.31 Behavior of the maximum residual slip velocity during the iteration. Here $\sigma = \epsilon$.

8.4.5.1 Stability criterion

To gauge the quality of a numerical simulation, one has to consider the *mesh* Reynolds number. In vortex methods, it is natural to use the mesh Reynolds number based on vorticity:

$$Re_h = \frac{|\underline{\omega}|\, h^2}{\nu}$$

A well-resolved simulation is one such that

$$Re_h = \mathcal{O}(1). \tag{8.82}$$

as this ensures that the relevant viscous scales presented in the flow are resolved. To accurately resolve the diffusion phenomena, it is required to have

$$\frac{\nu\, \Delta t}{h^2} = \mathcal{O}(1). \tag{8.83}$$

Multiplying (8.82) by (8.83), one finds that (Ploumhans & Winckelmans 2000)

$$|\underline{\omega}|\ \Delta t \ = \ \mathcal{O}\,(1)$$

Also, in the PSE the algorithm is stable under the condition (Cottet & Koumoutsakos 2000)

$$\frac{\nu\, \Delta t}{\epsilon^2} < \frac{1}{\lambda}$$

It was done by an analysis of the stabiblity of the PSE by Ploumhans and Winckelmans (2000). For the Gaussian smoothing function, one finds $1/\lambda = 0.595$ for the Euler explicit scheme.

8.4.6 Outline of the VIC scheme

With each building block of the VIC scheme described in the previous sections, one time step of the algorithm can be outlined as follows.

1. Create the grid used to solve the Poisson equation. It is chosen so that it tightly includes the vortex particles, and has regular Cartesian shape immersed in the body. The maximum and minimum particle position are first located and the VIC grid boundary is set up at several grid size apart from the extreme particle positions to ensure that the grid is not changed too often.

2. Interpolate the strengths of the particles onto the grid, to obtain the vorticity field $\underline{\omega} = \underline{\alpha}/V$ on the grid. The M_4' high order interpolation scheme was introduced for this purpose. The vorticity field is extended into the body, inside which the vorticity value is assigned by zero. The vorticity values replaced by zero are saved at another array for the PSE to be performed with including them.

3. Obtain the Dirichlet boundary condition for $\underline{\psi}$ on the sides of the VIC grid, using the fast algorithm by Kim (2003).

4. Solve the Poisson equation $\nabla^2 \underline{\psi} = -\underline{\omega}$ on the VIC grid using an FFT Poisson solver. The solver uses the grid with $\underline{\psi}$ provided on the boundaries and with $\underline{\omega}$ known inside. From the manipulation of the Fourier coefficients $\hat{\underline{\psi}}$ and $\hat{\underline{\omega}}$, the $\underline{\psi}$ field on the grid is constructed.

5. Evaluate the rotational velocity field, $\underline{u}_\omega$, from $\underline{\psi}$, using finite differences (the fourth order scheme used here). Evaluate the potential field with the resulting residual normal component of the rotational velocity plus free stream plugged into the boundary condition for the integral equation(no through flow condition). Superimpose the potential velocity field on the rotational field. Finally, the grid values are interpolated on to the particle locations.

6. Evaluate the stretching term, $\nabla \cdot (\underline{q}\ \ \underline{\omega})$, using finite differences on the grid. The conservative form leads to better results than the other form like $(\nabla \underline{q}) \cdot \underline{\omega}$. The stretching on the mesh is also sent back to particle positions.

7. Update the vortex strengths due to the stretching and diffusion. The particle strength exchange for diffusion includes the strengths interpolated into the grid inside the body.

$$\frac{\underline{\alpha}_i^{n+1} - \underline{\alpha}_i^{n}}{\Delta t} = h^3\, \nabla \cdot (\underline{\omega}\, \underline{q}) + \left. \frac{d\underline{\alpha}_i}{dt} \right|_{PSE}$$

8. Convect the particle with the interpolated velocity information on it. The

time integration of the ordinary differential equation

$$\frac{D\underline{x}_i}{Dt} = \underline{\mathrm{U}}_\infty + \nabla \times \underline{\psi} + \nabla \phi$$

is treated differently according to whether the particles are redistributed on regular location or not. In the case particle redistribution has been done prior to the time step, the second order Runge-Kutta scheme is used to convect particles.

$$\underline{x}_i^{*,n+1} = \underline{x}_i^n + \Delta t\, \underline{q}_i(\underline{x}^n,\, \underline{\alpha}^n)$$
$$\underline{x}_i^{n+1} = \underline{x}_i^n + \frac{1}{2}\Delta t \left(\underline{q}_i(\underline{x}^n,\, \underline{\alpha}^n) + \underline{q}_i(\underline{x}^{*,n+1},\, \underline{\alpha}^{*,n+1})\right)$$

After the first explicit Euler step, the velocity field is evaluated once more with the induced residual slip and wall diffusion due to the location change. In the case particle redistribution has not been done prior to the time step, as we have the velocity of a particle from the previous time step, the second order Adams-Bashforth scheme is used for update of particle positions.

$$\underline{x}_i^{n+1} = \underline{x}_i^n + \Delta t \left(\frac{3}{2}\underline{q}_i(\underline{x}^n,\, \underline{\alpha}^n) - \frac{1}{2}\underline{q}_i(\underline{x}^{n-1},\, \underline{\alpha}^{n-1})\right)$$

9. After the convection substep, a slip velocity comes to be present at the body boundary. The slip velocity $\underline{q}_s$ is translated into vortex sheet by $\Delta\gamma = \underline{n} \times \underline{q}_s$, and the vortex sheet is diffused by the wall diffusion formula to cancel the slip velocity. This algorithm is an immersed boundary method. Its schematic diagram is shown in Figure **8.32** . The normal component of the residual slip makes up the source strength in the integral equation for the potential field correction.

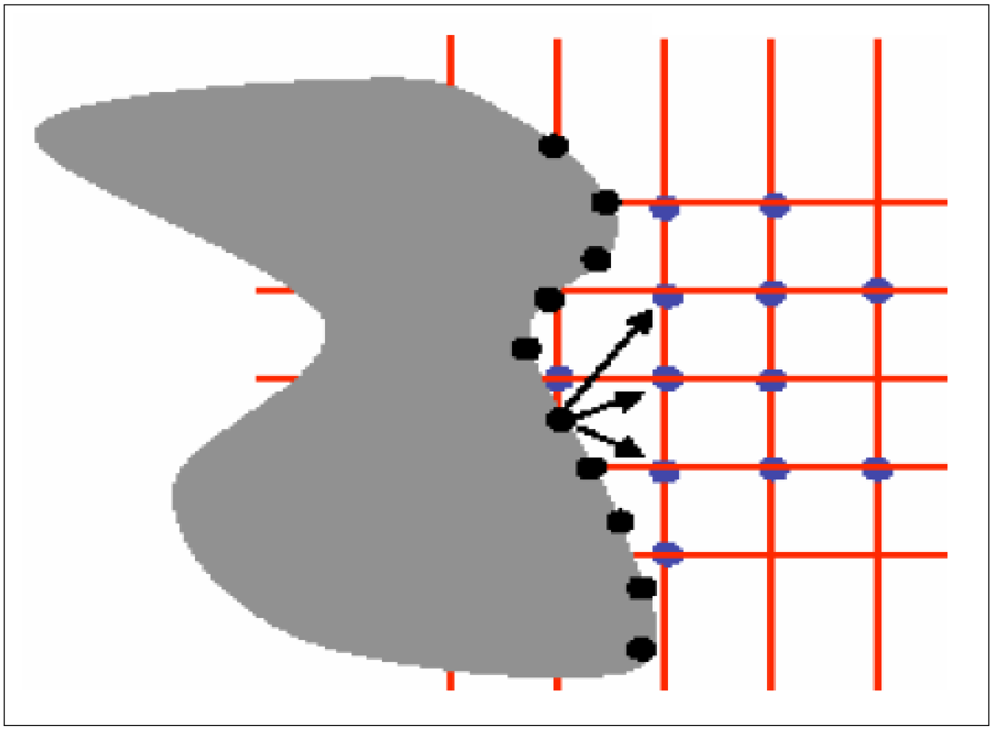

Figure 8.32 Diffusion of vorticity on a regular Cartesian grid in VIC methods. Vorticity correction is performed in the iterative way for satisfying the boundary condition at the surface. From Cottet & Poncet (2003).

8.4.7 Pressure calculation by panel method with a linearly varying singularity

The method of solving the pressure equation (6.26) with the boundary condition (6.35), when the integral equation (6.41) is formulated, is very similar to the procedure of finding potential field for the no through flow correction. The surface integral term can be discretized in the exactly same manner as the distribution of the potential on the triangular panel. The volume integral term, which is similar in form to Biot-Savart integral, must be manipulated with the Lagrangian particle representations.

$$\frac{\partial H}{\partial n} = -\frac{1}{Re}\underline{n}\cdot(\nabla\times\underline{\omega}) = -\frac{1}{Re}\left(\underline{t}\cdot\nabla\omega\right) = -\frac{1}{Re}\frac{\partial\omega}{\partial t} \tag{8.84}$$

where $\underline{t}$ is the unit tangential vector along the axis of symmetry on the body surface in axisymmetric flow. The source term can be evaluated in a general case by using the Stokes's theorem,

$$\int_S \underline{n} \cdot (\nabla \times \underline{\omega})\, dS = \int_C \underline{\omega} \cdot d\underline{l} \tag{8.85}$$

The value of $\underline{n} \cdot (\nabla \times \underline{\omega})$ for the node point i, is obtained by the approximation of the line integral,

$$\underline{n} \cdot (\nabla \times \underline{\omega})_i \approx \frac{1}{S} \sum_j \underline{\omega}_j \cdot d\underline{l}_j \tag{8.86}$$

where $\underline{l}_j$ is the line connecting the center of the panels, which has node i as one of their vertices. $\underline{\omega}_j$ is the mean value of the vorticities at the ends of a line, and S is the area of the polygon made up by the lines. Figure 8.33 illustrates the polygon for the evaluation of the source term. The surface value of the vorticity is obtained by just switching a surface point into the particle representation of the vorticity field. The value of vorticity at the center of each panel is computed from applying the inverse distance weight to the vorticity at the vertices of the panel.

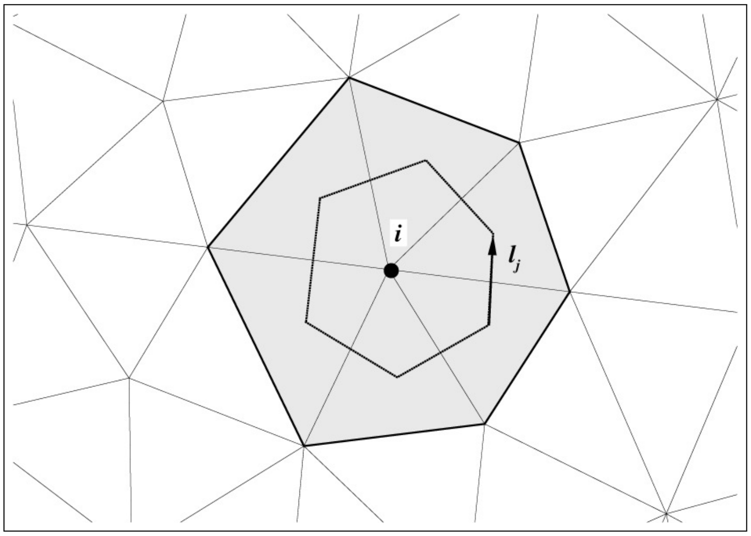

Figure **8.33** Schematic arrangement for boundary condition of the pressure head H.

By using the vector relation $\nabla \cdot (\underline{u} \times \underline{\omega})\; G = \nabla \cdot ((\underline{u} \times \underline{\omega})\, G) - (\underline{u} \times \underline{\omega}) \cdot \nabla G$, the integrand of the volume integral can be modified as

$$\int_V \nabla \cdot (\underline{u} \times \underline{\omega})\, G\, dV = \oint_S \underline{n} \cdot (\underline{u} \times \underline{\omega})\, G\, dS - \int_V (\underline{u} \times \underline{\omega}) \cdot \nabla G\, dV \tag{8.87}$$

The first integral in the right-hand side vanishes because the velocity on the body boundary is zero and the vorticity becomes zero at far field. Substituting the particle representation of the vorticity field for $\underline{\omega}$ in the above equation, we can get the discretized volume integral as follows.

$$\begin{aligned}\int_V \nabla \cdot (\underline{u} \times \underline{\omega})\, G\, dV &= -\int_V (\underline{u} \times \underline{\omega}) \cdot \nabla G\, dV \\ &= -\sum_{k=1}^{N} \underline{u}_k \times \underline{\alpha}_k \cdot \nabla G \int_{V_k} \zeta_k\, dV \\ &= -\sum_{k=1}^{N} (\underline{u}_k \times \underline{\alpha}_k) \cdot \frac{\underline{x} - \underline{x}_k}{|\underline{x} - \underline{x}_k|^3}\, q\left(\frac{\underline{x} - \underline{x}_k}{\epsilon_k}\right)\end{aligned} \tag{8.88}$$

where

$$q(\rho) = \left\{ \operatorname{erf}\left(\frac{\rho}{\sqrt{2}}\right) - \rho\sqrt{\frac{2}{\pi}} \exp\left(-\frac{\rho^2}{2}\right) \right\} \tag{8.89}$$

The use of cutoff function can avoid the singularity in the gradient of the Green function. The final form of the discretization reduces to the similar one in (8.78) with the volume integral having on the right hand side.

8.5 Numerical Results by VIC Methods

In this section, the present VIC method is applied to the flow simulation around several 2-D and 3-D bodies. The flow field around impulsively started two dimensional bodies are firstly simulated, for a circular cylinder and a NACA0012 hydrofoil section. For 3-D, the flow around a sphere is simulated as a typical example of wake flow behind a bluff body. The VIC algorithm then is also applied to the rectangular wing of finite span.

8.5.1 Two dimensional flows

In the case of two dimensional flow the vorticity is a scalar variable and the governing equation for it does not carry the stretching term,

$$\frac{D\omega}{Dt} = \nu\nabla^2\omega \tag{8.90}$$

The diffusion is the only process to change strengthes of particles. Moreover, the vector potential becomes scalar field known as stream function. The Poisson equations for the vector potential and the vorticity reduce to one component,

$$\nabla^2\psi = -\omega \tag{8.91}$$

The velocity components (u, v) are given by,

$$u = \frac{\partial\psi}{\partial y}, \quad -v = \frac{\partial\psi}{\partial x} \tag{8.92}$$

The stream function can be obtained on the boundaries using two dimensional Green's function

$$\psi = -\frac{1}{2\pi}\int \omega \, \ln r \, dS \tag{8.93}$$

8.5.1.1 Impulsively started circular cylinder

In this section the result of computation is provided for the flow over a circular cylinder impulsively set into motion with a constant speed U_∞ in the direction negative x coordinate. For this problem, a large number of experimental and numerical results has been available in the literature. The Reynolds number is defined as $Re = DU_\infty/\nu$, where D is the diameter of the cylinder and ν is the kinematic viscosity. The computational results are presented for a Reynolds number 550.

The computational parameters are given in the Table 8.3. The cylinder surface is discretized by 600 line panels with even length. The particle size is balanced with the panel size and, at the same time, is chosen to meet the stability restriction.

Table **8.3** Parameters used in the numerical simulation of the flow around an impulsively started circular cylinder.

Reynolds number	550
Number of panels	600
Blob size, σ	0.00521
Time step, Δt	0.01
Cutoff parameter, ϵ_Γ	0.001

Figure 8.34 shows a comparison between the analytical expression of impulse I_x for short times by Bar-Lev and Yang (1975) and I_x computed by the present scheme. The comparison includes the result computed by Ploumhans and Winckelmans (2000). The present scheme gives slightly different values for the very earlier time ($t < 0.10$).

The time history of the drag coefficent is compared in Figure 8.35 for short times and 8.36 for longer times. For the early developed flows, the present scheme predicts the drag coefficients close to the analytical results. The comparison for longer times with Ploumhans and Winckelmans (2000) in Figure 8.36 does not show distinguishable results, while the impulse shows slightly different longer time behavior as presented in Figure 8.34 . This means that the absolute values of the impulses are slightly different between the two method, but the changes of the impulse are revealed to have similar time rates. The difference seems to be caused by the parameters chosen by each scheme.

The profiles of streamwise centerline velocity in the wake is shown in Figure 8.37 with the experimental results by Bouard & Coutanceau (1980). Their results are provided with the time nondimensinalized by the radius of cylinder, whereas the present scheme uses the diameter as the characteristic length. The time in the figure represents nondimensional time by the diameter of the cylinder. There is good qualitative agreement, but the length of the wake(distance to the point the velocity profile crosses the x axis) is computed somewhat shorter than the experiment. Due to the use of compact grid for velocity computation, the profiles of the present scheme are not presented beyond the extent of the grid.

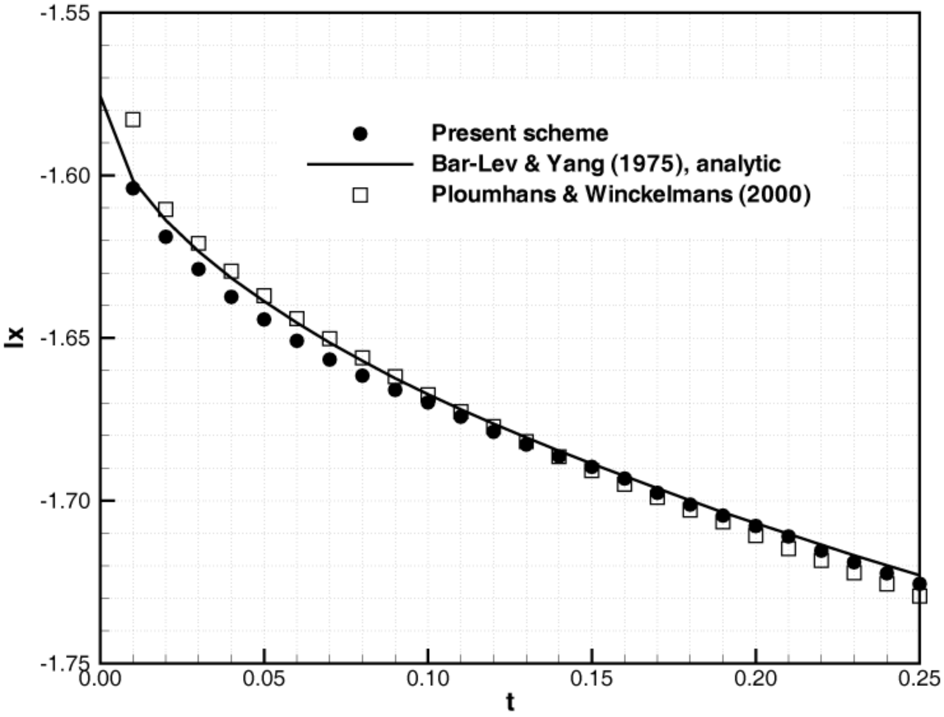

(a) Short time

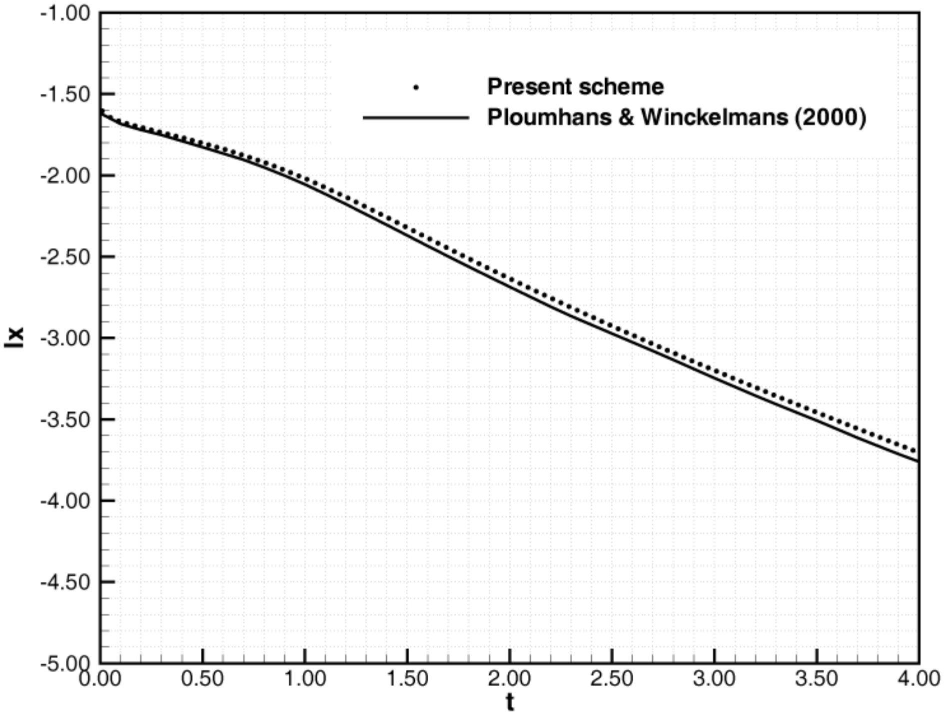

(b) Long time

Figure 8.34 Comparison of I_x for an impulsively started circular cylinder at $Re = 550$.

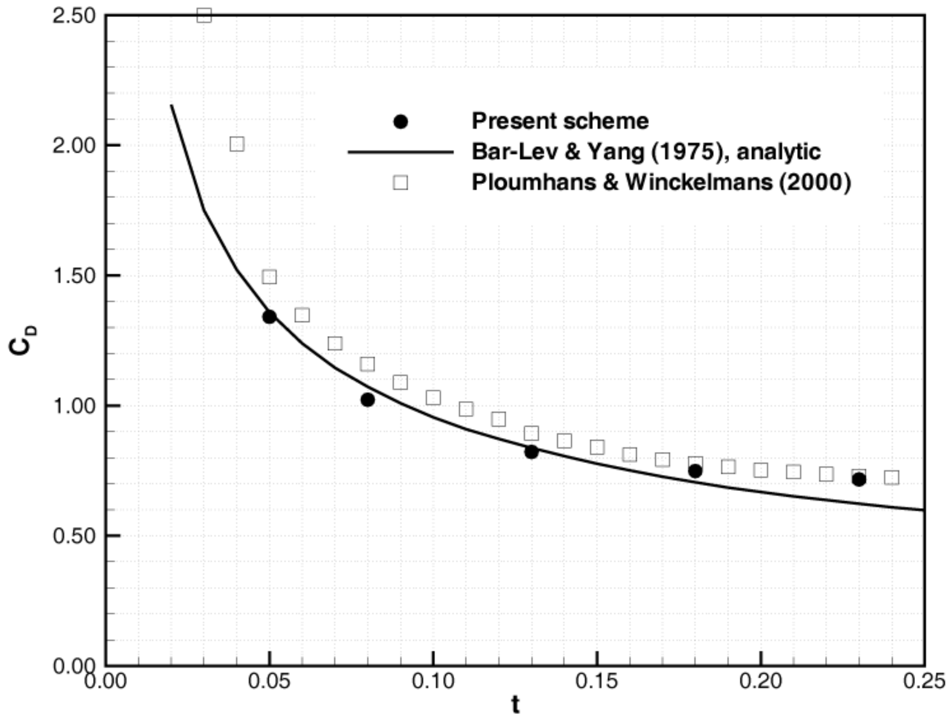

Figure 8.35 Drag coefficient of an impulsively started circular cylinder at early stage of times for $Re = 550$.

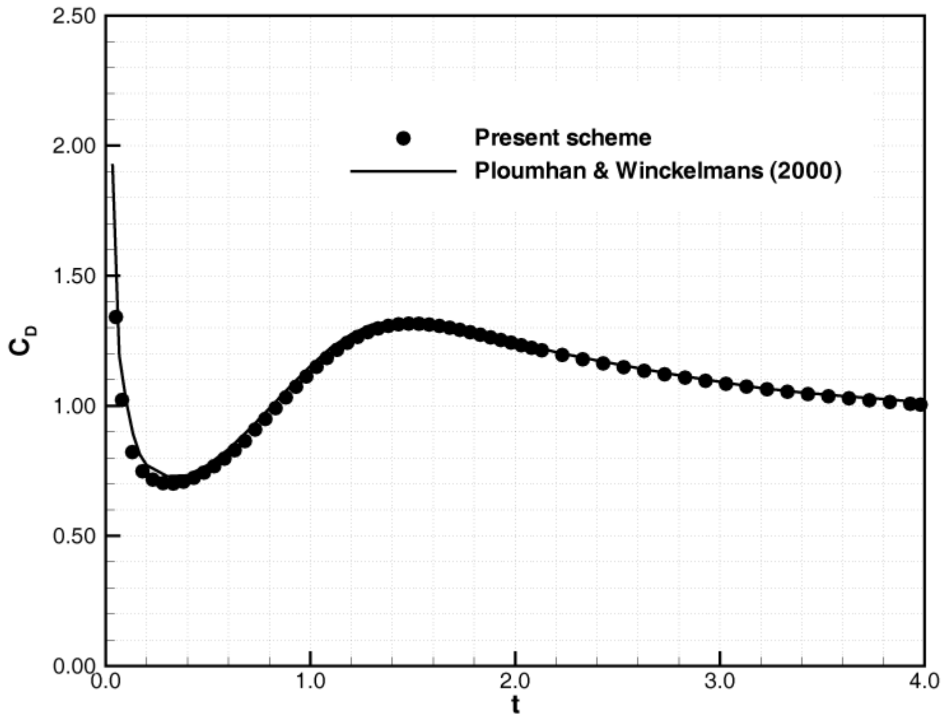

Figure 8.36 Drag coefficient of an impulsively started circular cylinder for $Re = 550$.

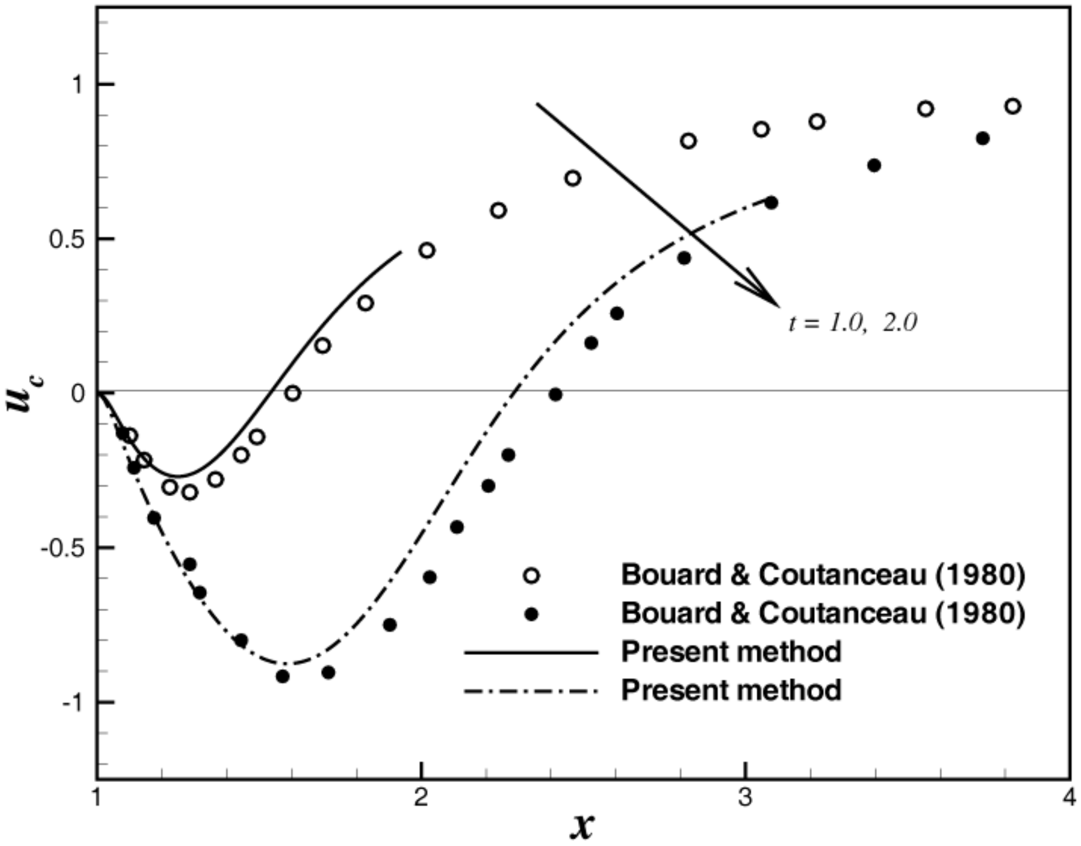

Figure 8.37 Velocity distribution along wake centerline for an impulsively started circular cylinder for $Re = 550$.

Computed streamlines are shown in Figure 8.38 . Note that the cylinder moves to the left. A large recirculating flow region of closed streamlines is clearly captured behind the cylinder. The streamwise length of this recirculating region grows in time. The region is also called as the separation bubble.

The streamline at $t = 3.0$ is compared with the results obtained in the experiment of Bouard and Coutanceau (1980) in Figure 8.39 . The computed streamline in the large recirculating flow region are in good visual agreement with those of the experiment. Along with the large recirculating regions, smaller secondary recirculation zones between rear half of the cylinder and the separation bubbles are observed in the computation, as well as in the experiment.

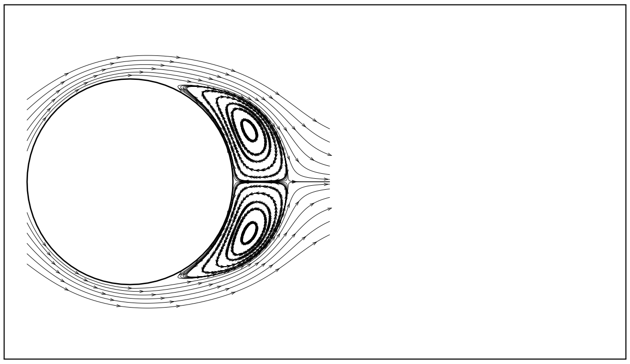

(a) $t = 1.0$

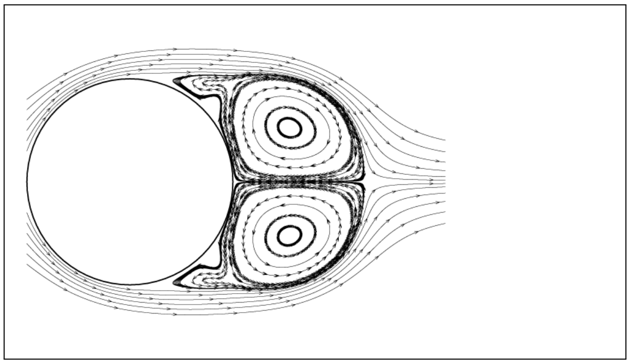

(b) $t = 2.0$

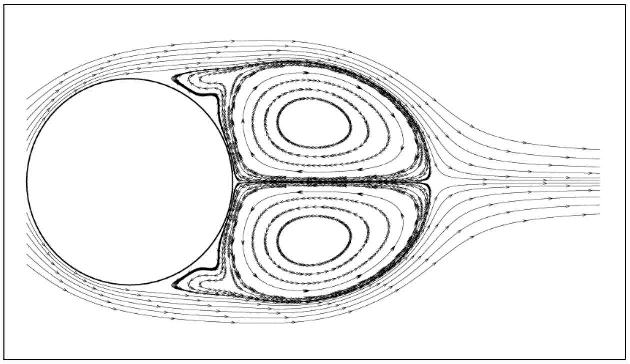

(c) $t = 3.0$

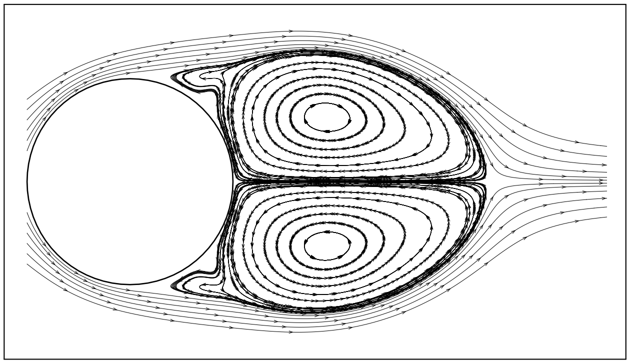

(d) $t = 4.0$

Figure 8.38 Instantaneous streamlines around impulsively started circular cylinder at $Re = 550$.

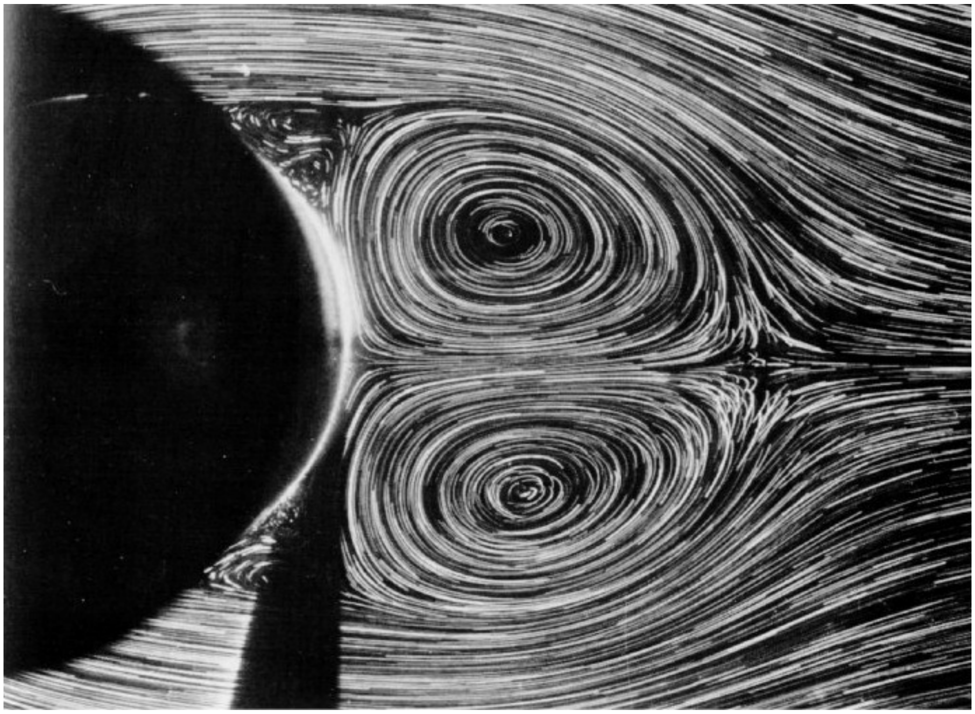

(a) Streamlines from experiment, Bouard & Coutanceau

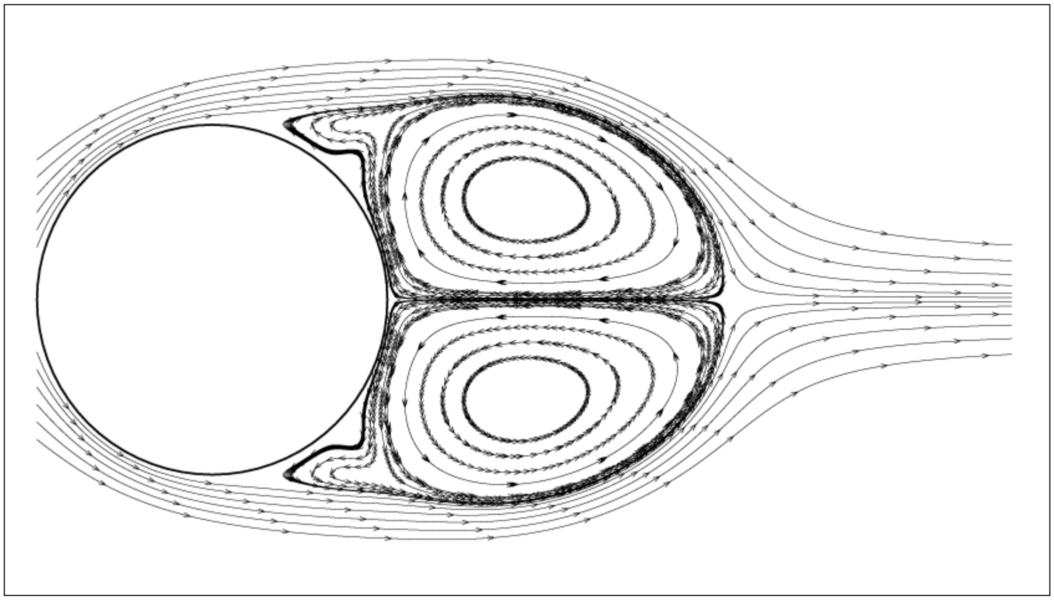

(b) Streamlines from the present method

Figure 8.39 Comparison of streamlines for an impulsively started circular cylinder for $Re = 550$.

8.5.1.2 Impulsively started NACA0012 hydrofoil

As a second representative for simulation in two dimension, an impulsively started NACA0012 section hydrofoil is selected in order to examine suitability of the method for the analysis of thin streamlined body with sharp edge. The Reynolds number is 1200, based on the chord length of the section. The parameters used in the simulation are listed in Table **8.4**. The computations are performed at two angles of attack, $\alpha = 0^\circ$ and 30°.

Table 8.4 Parameters used in the numerical simulation of the flow around an impulsively started NACA 0012 hydrofoil.

Reynolds number	1200
Number of panels	800
Blob size, σ	0.00249
Time step, Δt	0.005
Cutoff parameter, ϵ_Γ	0.001

Figure **8.40** compares impulse I_x with the result of Lee (2005) for zero angle of attack. In his vortex method, a fast algrithm is used for the convection velocity and image particles are located underneath body panels to correct PSE diffusion. As shown in the figure, the impulses are in good agreement for long times as well as for short times.

The method is applied next to the flow at angle of attack $\alpha = 30^\circ$. After the impulsive start, the starting vortex is formed from the trailing edge and shed into the wake as shown in Figure **8.41** . At the same time, the flow is separated from the leading edge and a vortex is generated. The leading edge vortex rolls downstream along the suction side and convects slowly near the surface. Two secondary vortices can be seen to have been formed upstream of the separated vortex. The computed streamlines are compared with the experimental results by Huang et al. (2001). Figures **8.42** and **8.43** show the observation results using the particle tracking flow visualization along with the streamlines from the present scheme. The large separation vortex from leading edge and the two secondary vortices are clearly seen in the figures.

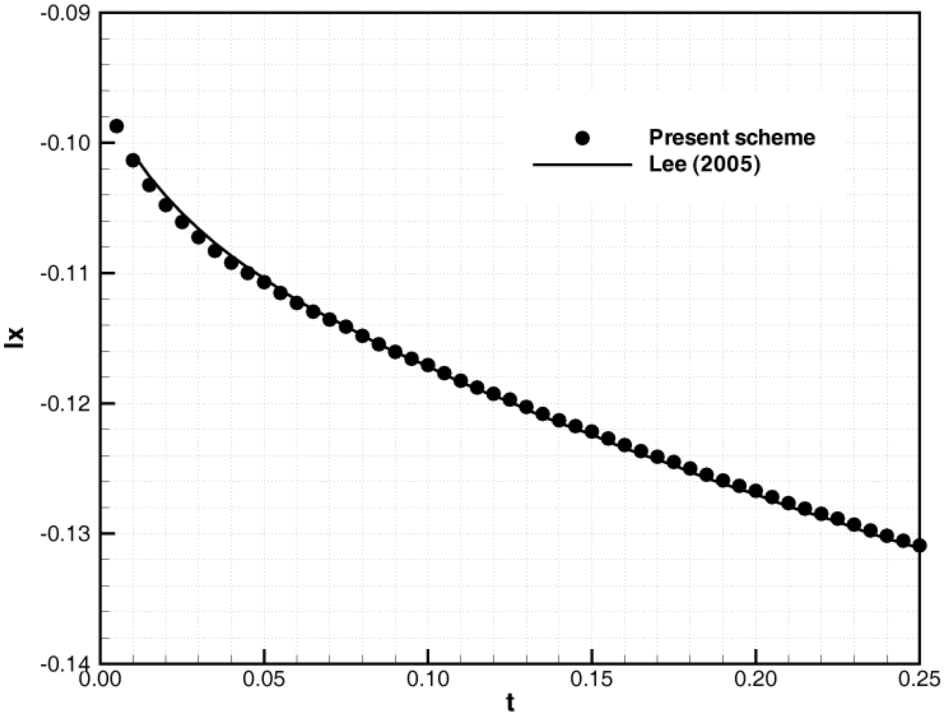

(a) Short time

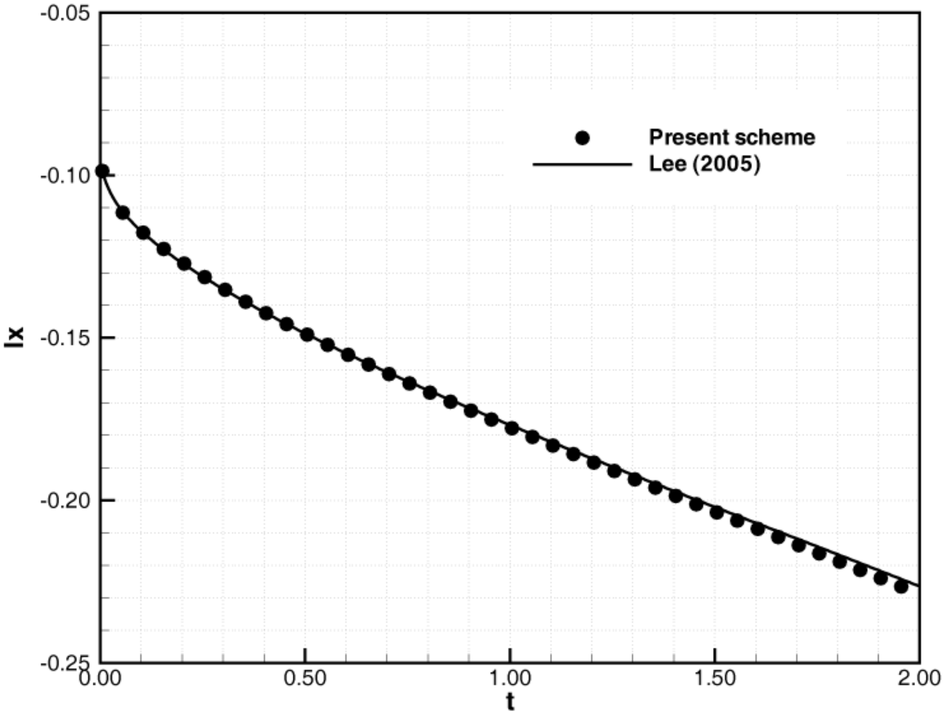

(b) Long time

Figure 8.40 Comparison of I_x for an impulsively started NACA0012 hydrofoil at zero angle of attack for $Re = 1200$.

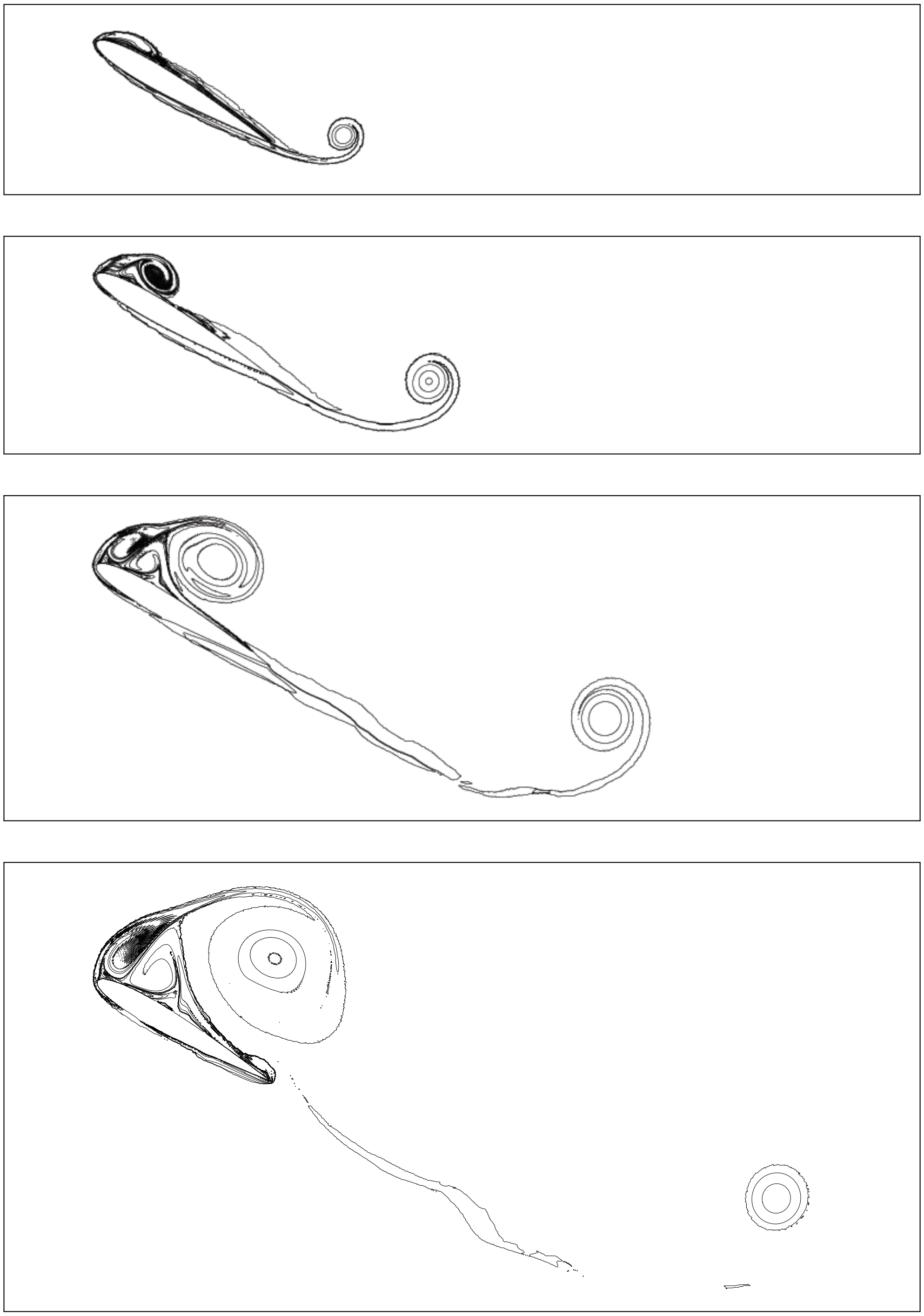

Figure 8.41 Vorticity contours for an impulsively started NACA0012 hydrofoil for $\alpha = 30^\circ$ and $Re = 1200$. The time is at $T = 0.5, 1.0, 2.0, 3.0$ from top.

(a) Streamlines from experiment, Huang et al (2001), $t = 1.043$

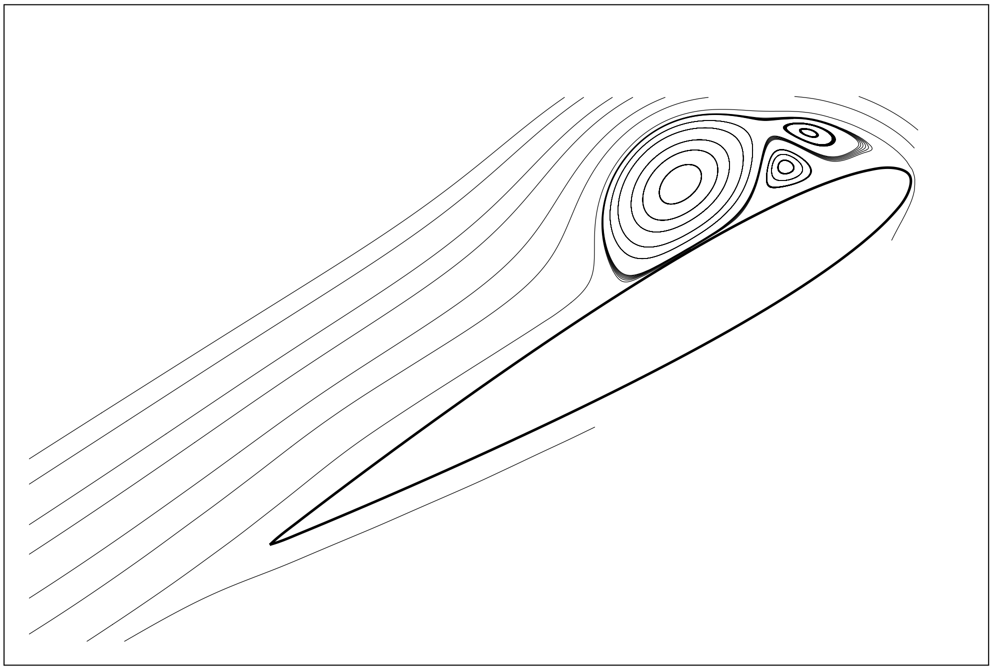

(b) Streamlines from the present method, $t = 1.0$

Figure 8.42 Comparison of streamlines at $T = 1.0$ with the experimental snapshot for an impulsively started NACA 0012 hydrofoil at $\alpha = 30°$ for $Re = 1200$.

(a) Streamlines from experiment, Huang et al (2001), $t = 2.348$

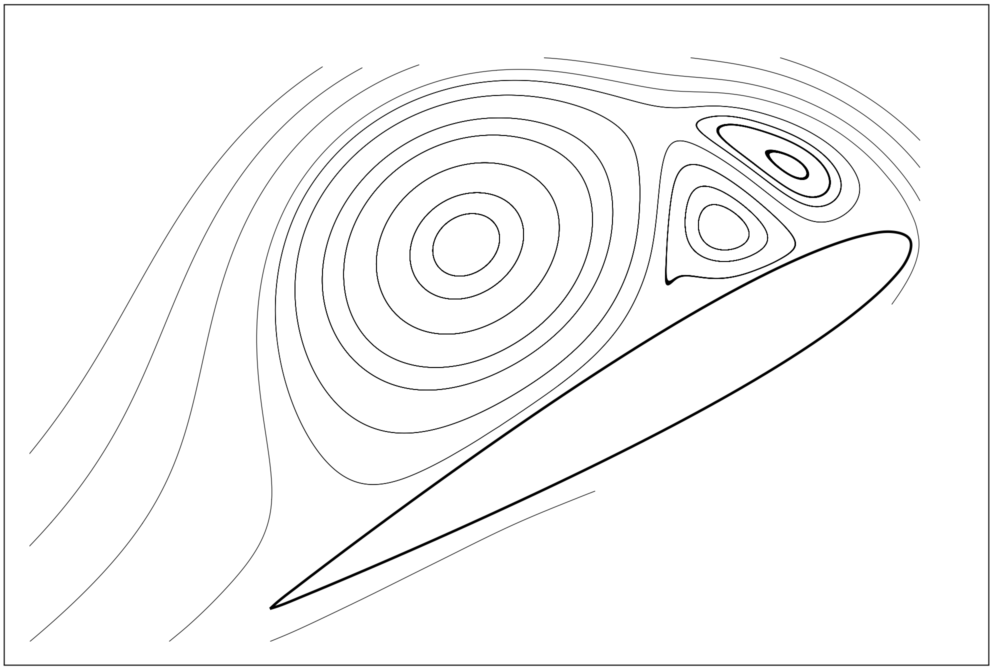

(b) Streamlines from the present method, $t = 2.0$

Figure 8.43 Comparison of streamlines at $T = 2.0$ with the experimental snapshot for an impulsively started NACA 0012 hydrofoil at $\alpha = 30°$ for $Re = 1200$.

8.5.2 Three dimensional flows

8.5.2.1 Sphere

The flow past a sphere is considered as an example for three dimensional bluff body flow analysis. It has been investigated numerically and experimentally at Reynolds number $Re = U_\infty D/\nu$ between about 0.5 and several thousand by many authors. From the experimental work of Taneda (1956), it is found that a recirculating zone develops close to the rear stagnation point at about $Re = 30$. This recirculating zone or wake expands toward streamwise direction as well as along the surface of the sphere with further increase in the Reynolds number. The flow remains steady and axisymmetric up to ***Re*** = 210 $\sim$ 212. Defining locations on the surface by the angle from the front stagnation point, the separation point moves forward from about $130°$ at $Re = 100$ to about $115°$ at $Re = 300$.

In this work, the flows at $Re = 50, 100$ are simulated and compared with the numerical solution of Johnson & Patel (1999). The sphere of radius 0.5 is discretized into triangular panels, and the number of panels is 10,008. Figure 8.44 shows the discretization of the sphere.

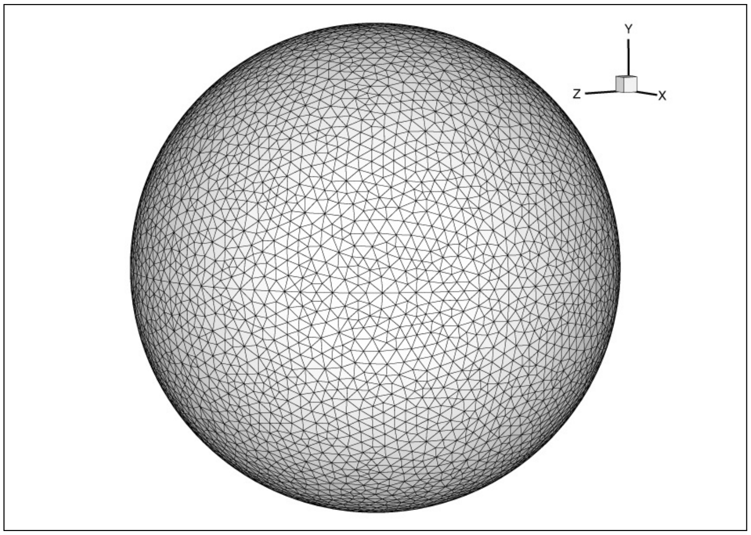

Figure 8.44 Surface panel discretization of a sphere.

The number of vertices is about half of the panels. The grid size h is selected to be square root of mean area of the panels $h = \sqrt{A_{mean}}$, where $A_{mean} =$

$\sum A_i/N$. The time step for the simulation is $\Delta t = 0.02, 0.015$ for the Reynolds number of 50, 100, respectively. The value of $\epsilon_\alpha = 10^{-4}$ and $Re_{h,trsh} = 10^{-4}$ are used.

The drag coefficients from the derivative of the linear impulse are plotted in Figure **8.45** along with the classical curve of $C_d = C_d(Re)$ for the flow past a sphere. The drag coefficient C_d is calculated at the final stage of the computation when the change of the linear impulse is thought to come into a steady phase and shows good agreement with the curve. The drag coefficients are made further comparison with the computation by Johnson & Patel (1999) in Figure **8.46** , and also show good agreement with their results.

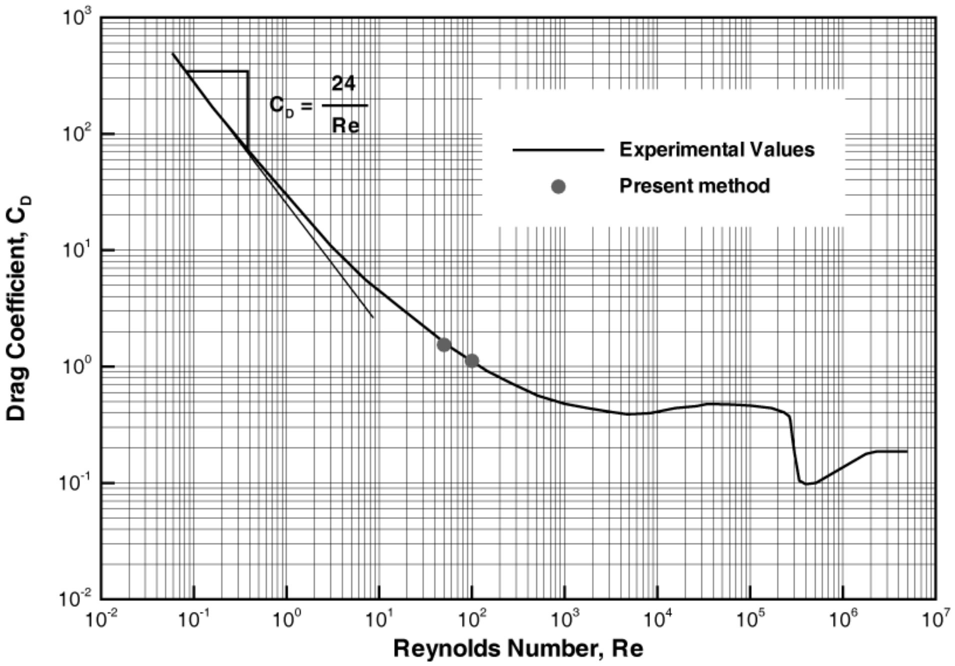

Figure **8.45** Comparison of drag coefficient of a sphere with experiments.

The streamline patterns, vorticity contours and pressure fields at several early moments for $Re = 100$ are provided in Figures **8.47** , **8.48** , and **8.49** , respectively.

The streamlines, vorticity contours and contours of pressure coefficients are also compared with the numerical results of Johnson & Patel (1999), in Figures **8.50** $\sim$ **8.53** . The length of the separation bubble in the flow direction(left to right) seems to be in good agreement.

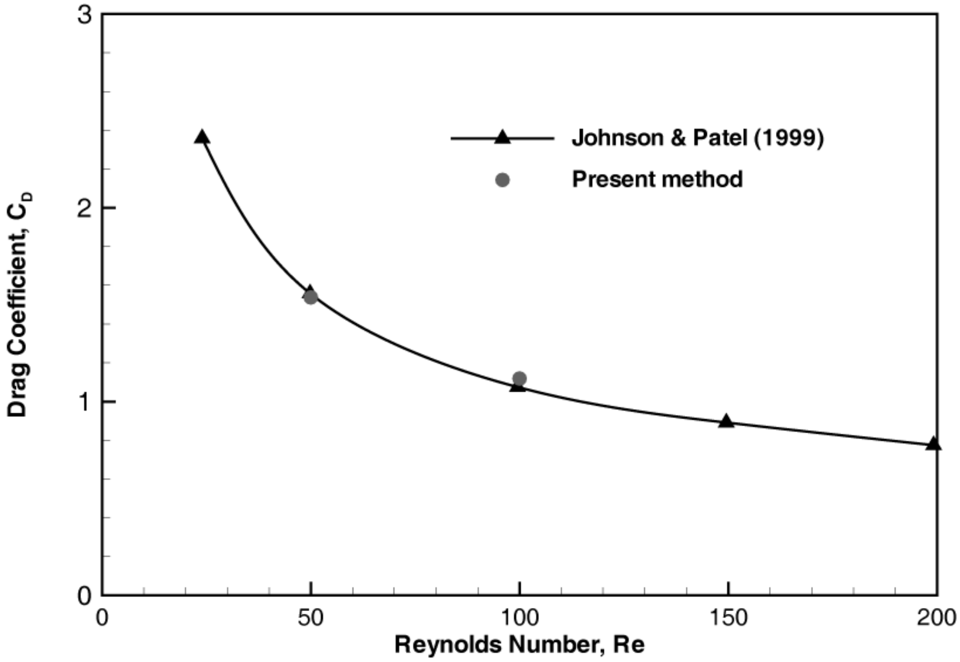

Figure **8.46** Comparison of drag coefficient of a sphere with the numerical one by Johnson & Patel (1999).

Figure 8.51 compares the length and position of the vortex center, and shows good agreement with the results of Johnson & Patel. The downstream extensions of vorticity contour of ± 0.5 from the present method show slightly shorter than the results by Johnson & Patel. Figure 8.54 compares the streamline of the present scheme with the visualization by Taneda (1956). As the Reynolds number of the expmeriment is 118, which is larger than the present computation, the recirculating zone expands more downstream. But, the general appearance of the flow including separation point looks very similar to the computed result.

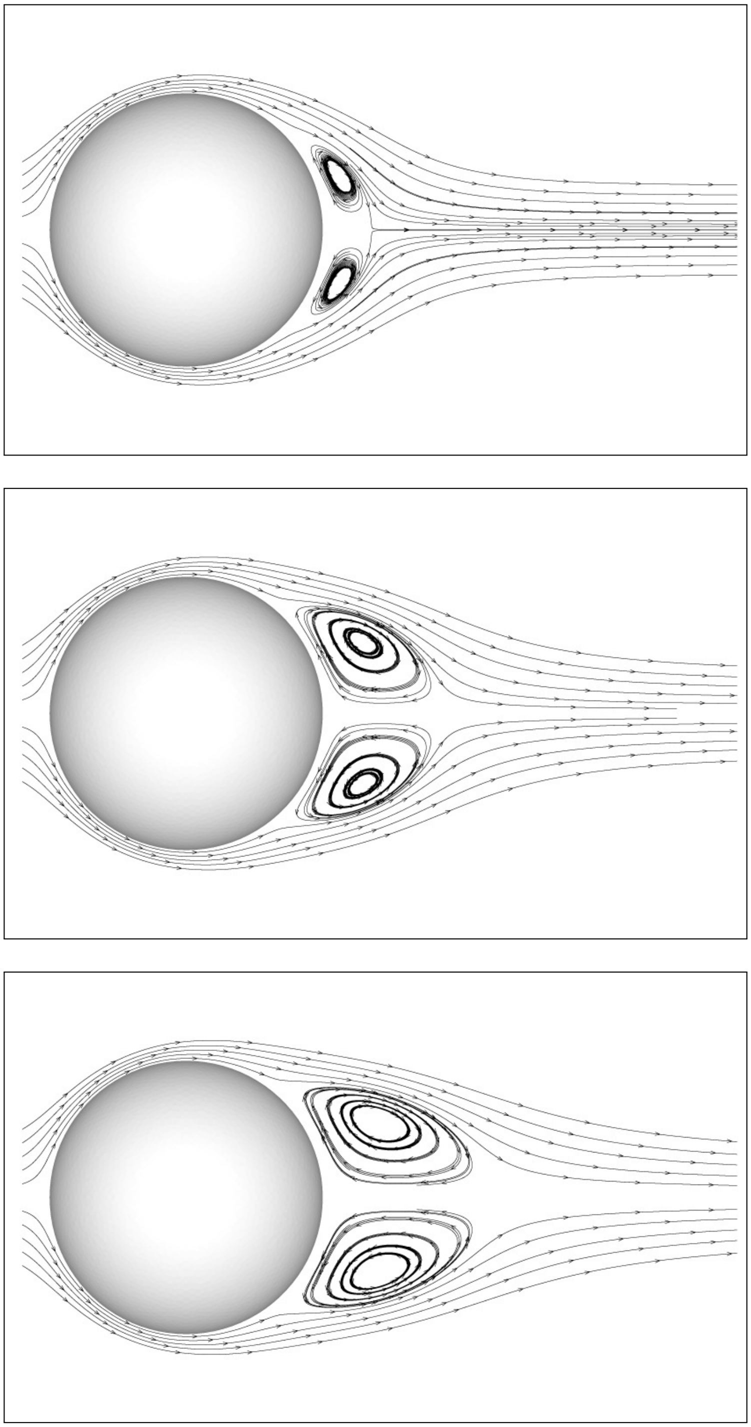

Figure 8.47 Streamlines about an impulsively started sphere for $Re = 100$. The time is at $T = 1.0, 2.0, 3.0$ from top.

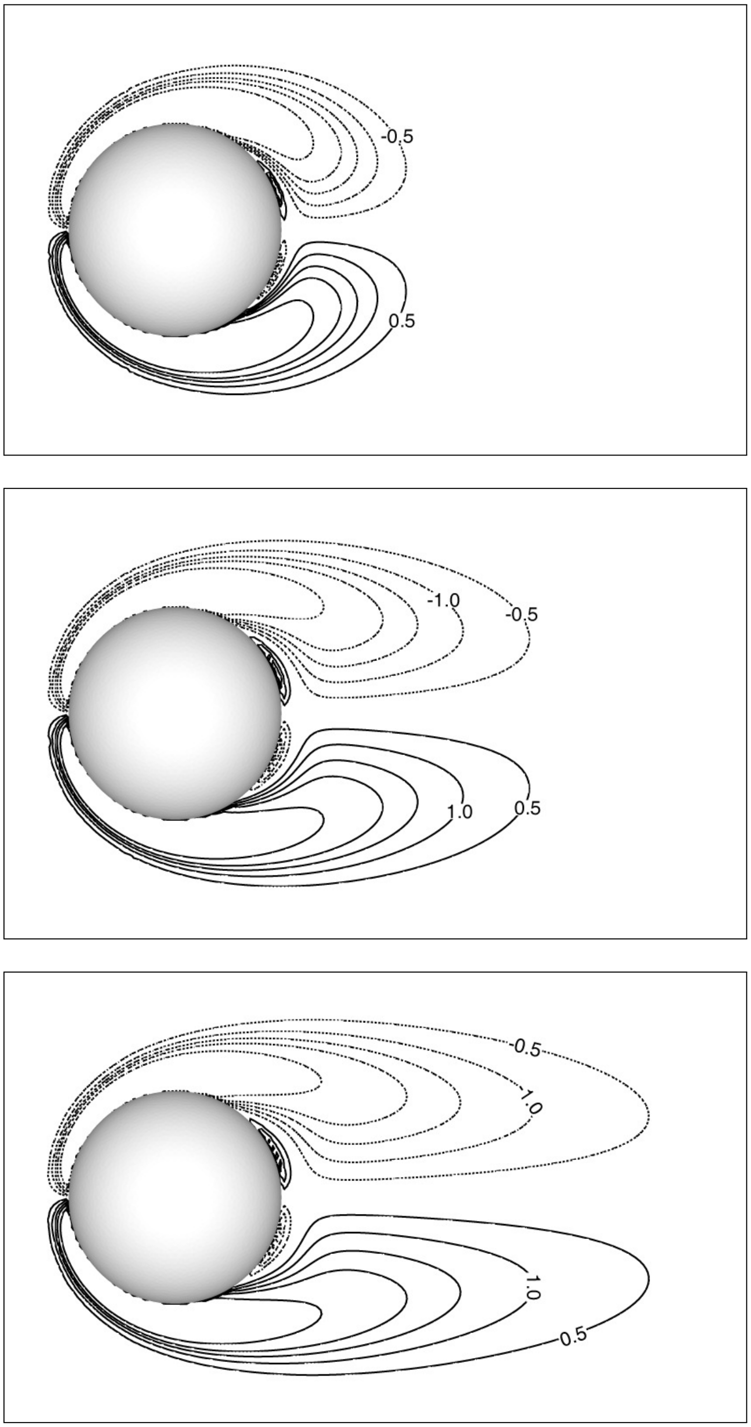

Figure 8.48 Vorticity contours for an impulsively started sphere for $Re = 100$. The time is at $T = 1.0, 2.0, 3.0$ from top.

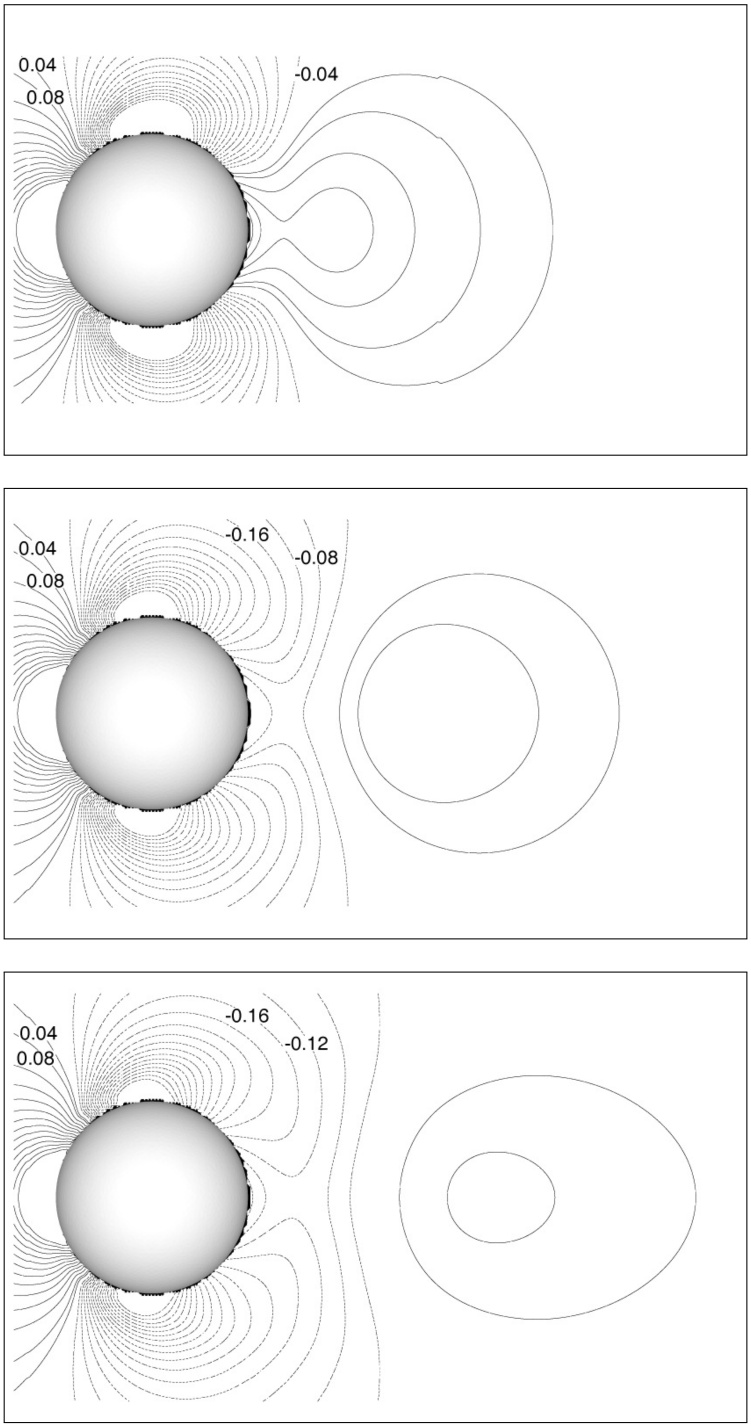

Figure 8.49 Pressure coefficient contours for an impulsively started sphere for $Re = 100$. The time is at $T = 1.0, 2.0, 3.0$ from top.

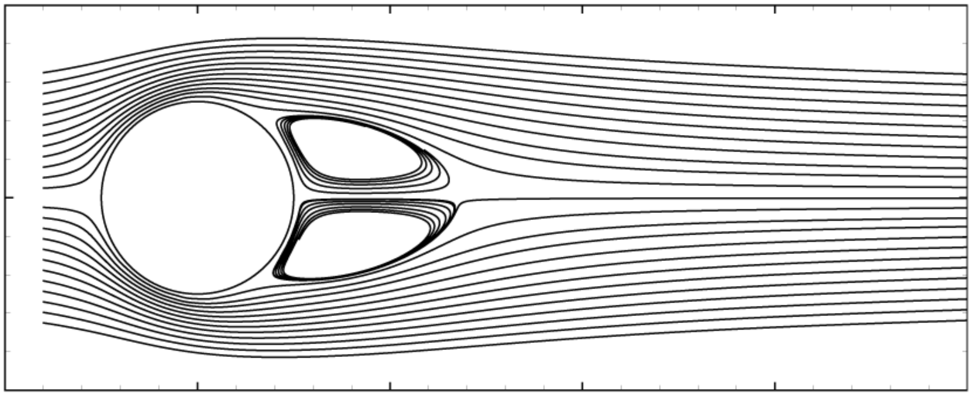

(a) Streamlines from the present method ($t = 7.5$)

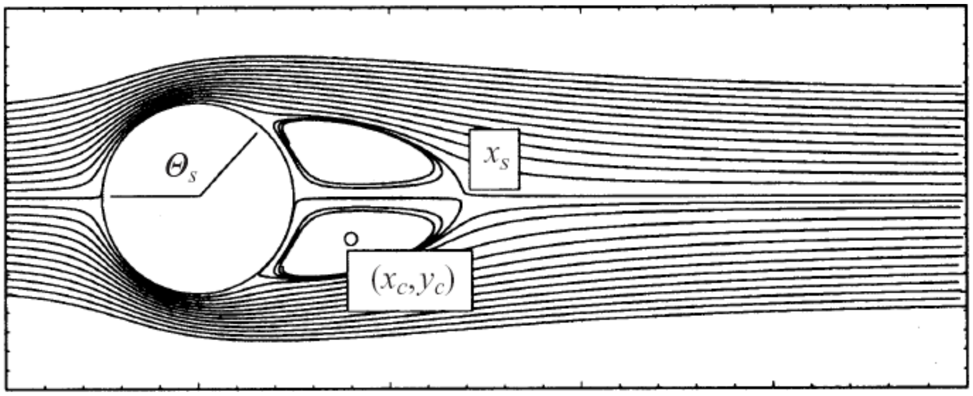

(b) Streamlines computed by Johnson & Patel (1999)

Figure 8.50 Comparison of streamlines about a sphere for $Re = 100$ with the numerical ones by Johnson & Patel (1999).

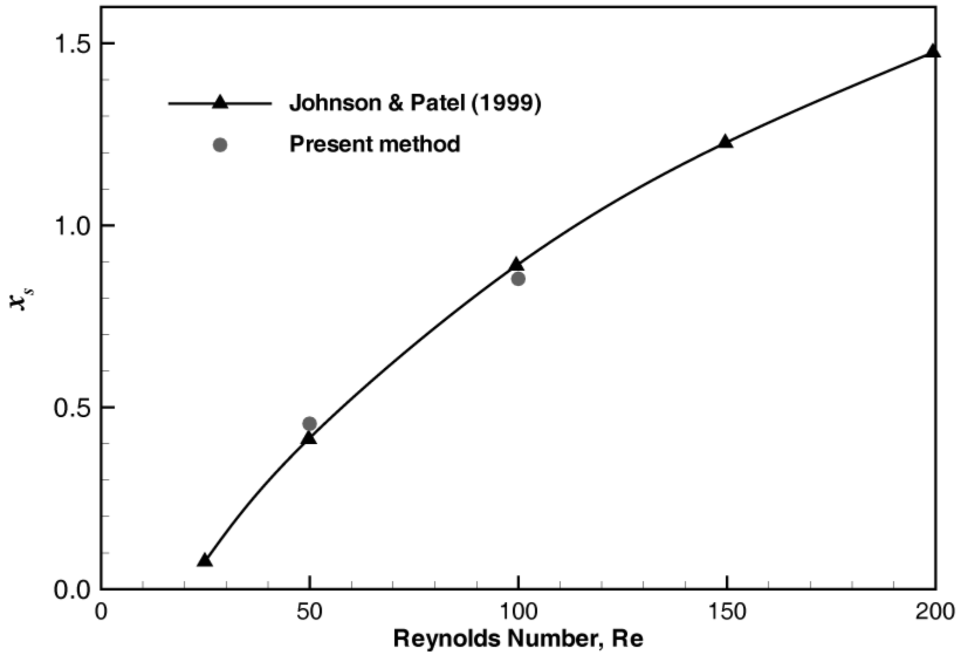

(a) Separation length, x_s

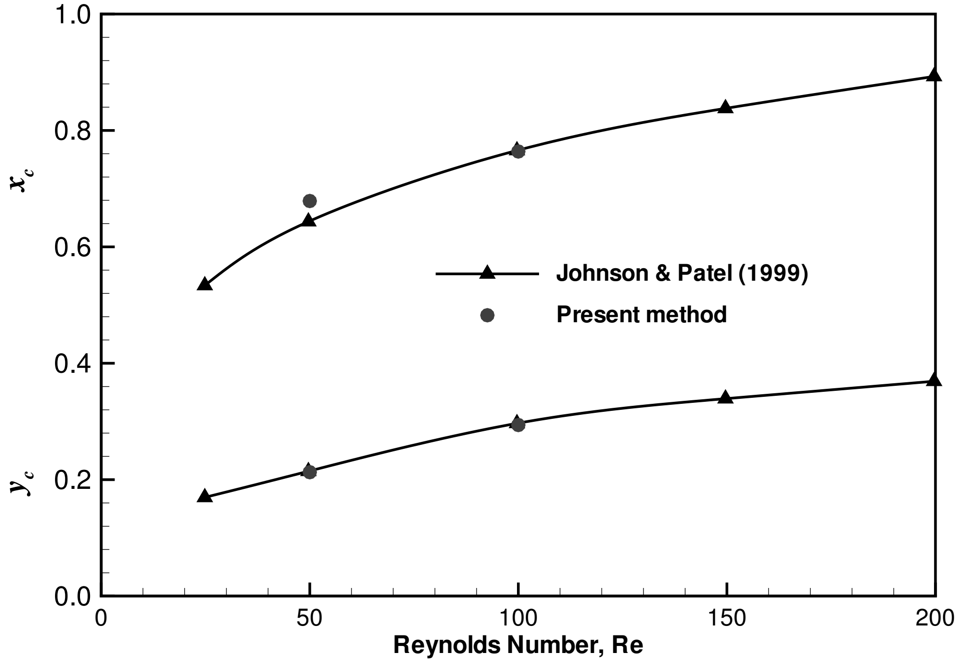

(b) Vortex position, (x_c, y_c)

Figure **8.51** Comparison of wake pattern for a sphere with the numerical one by Johnson & Patel (1999). x_s denotes the distance from the sphere of the end point of the wake. x_c and y_c are the center position of the vortical shedding wake.

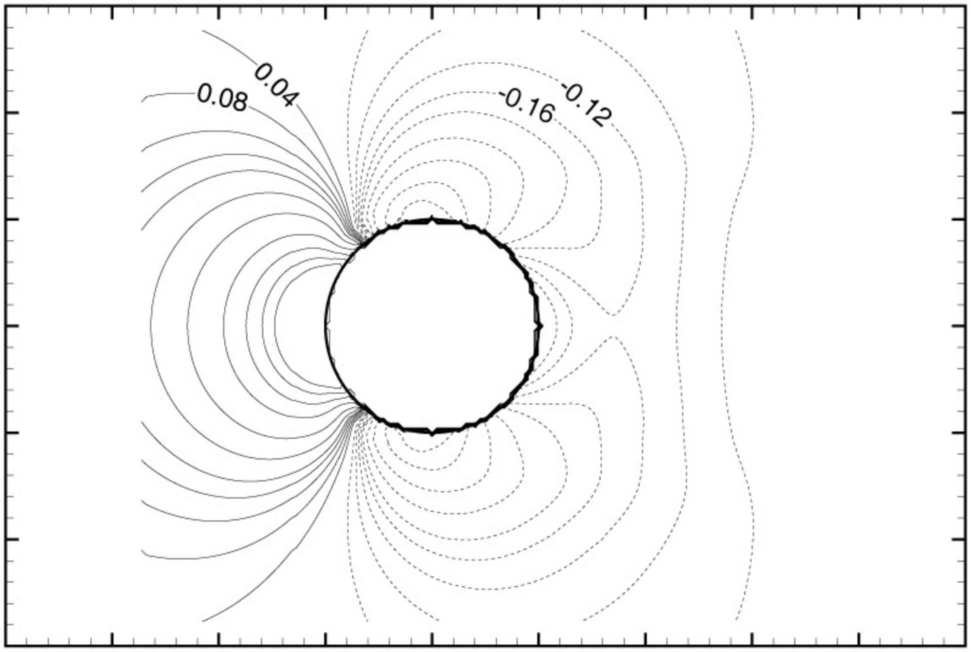

(a) C_p from the present method ($t = 7.5$)

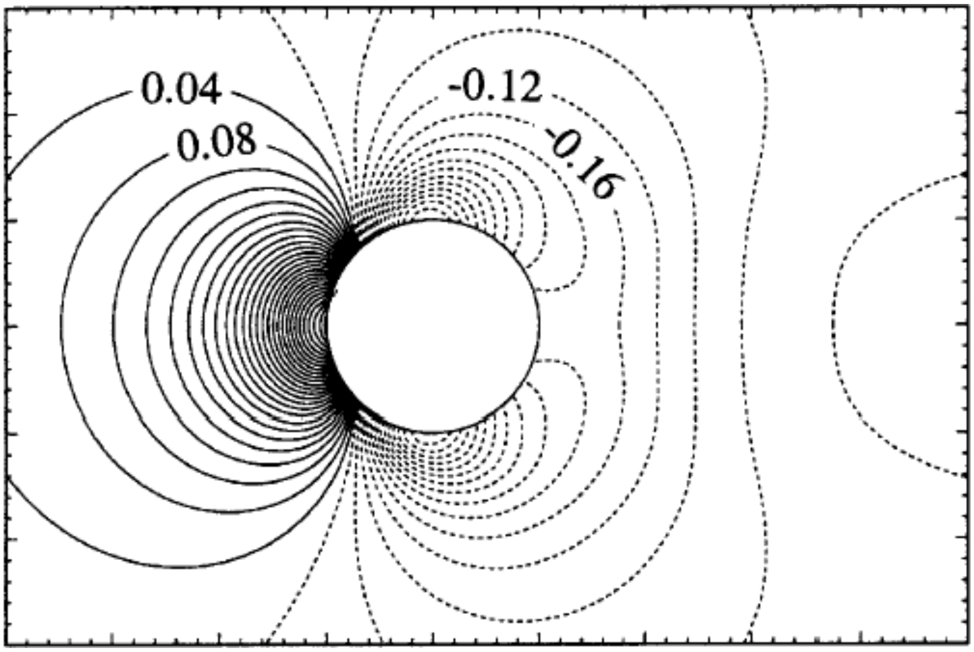

(b) C_p computed by Johnson & Patel (1999)

Figure 8.52 Comparison of pressure contours for a sphere for $Re = 100$ with the numerical one by Johnson & Patel (1999).

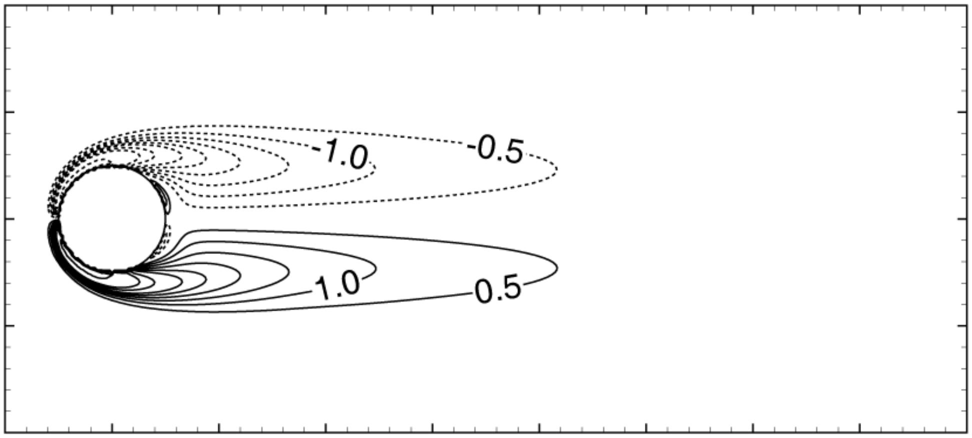

(a) Contours from the present method ($t = 7.5$)

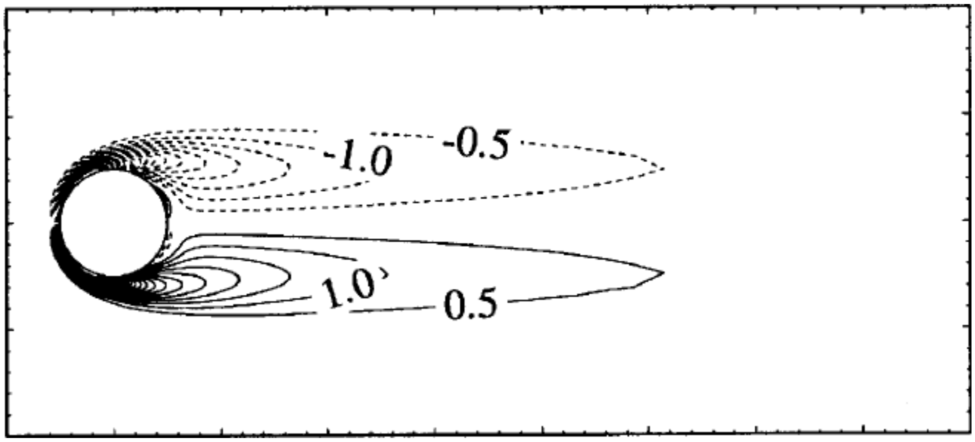

(b) Contours computed by Johnson & Patel (1999)

Figure 8.53 Comparison of vorticity contours for a sphere for $Re = 100$ with the numerical one by Johnson & Patel (1999).

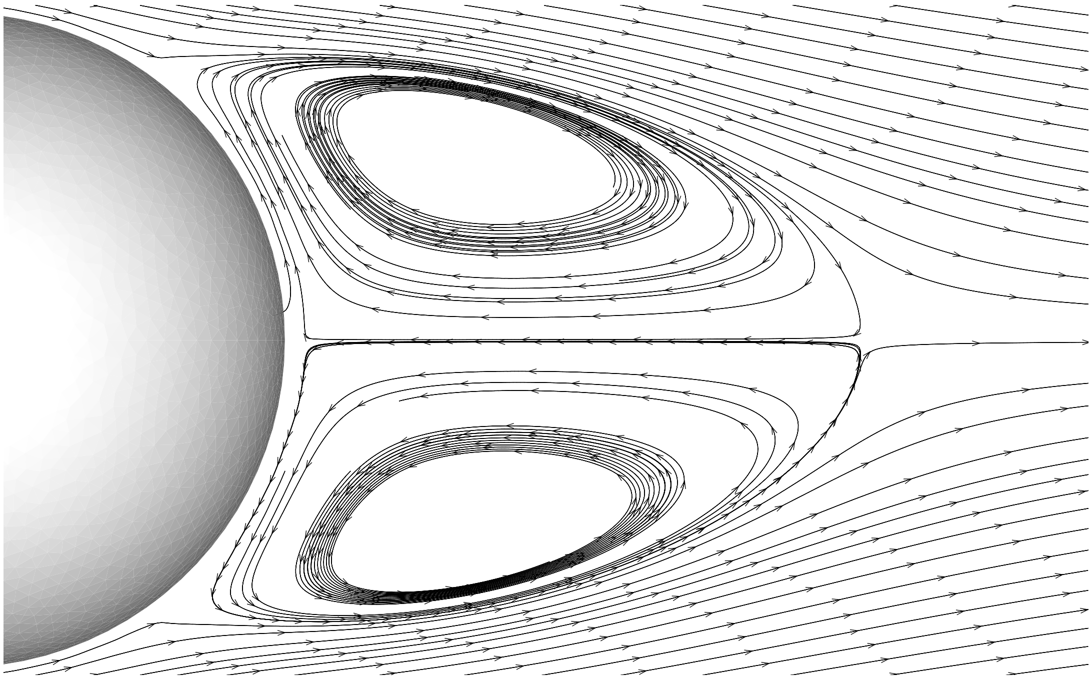

(a) Streamlines from the present method

(b) Visualization from experiment ($Re = 118$), Taneda

Figure 8.54 Comparison of streamlines for a sphere for $Re = 100$ with the experimental ones by Taneda (1956).

Figures 8.55 $\sim$ 8.57 show the streamlines, vorticity contours, and contours of the pressure coefficient at $Re = 50$ and 100. For the two Reynolds numbers the general characteristic feature of the flow remains the same with the changes only in separation location, the center of recirculating flow, and the length of wake. The separation point moves upstream with the increase of Reynolds number. At Reynolds number of 100, the opposite sign of vorticity exists between the surface of the sphere and the separation vortex.

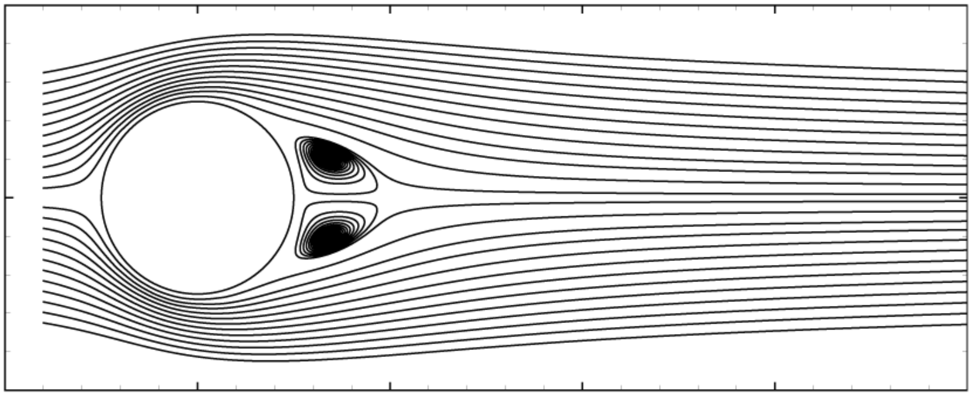

(a) $Re = 50$

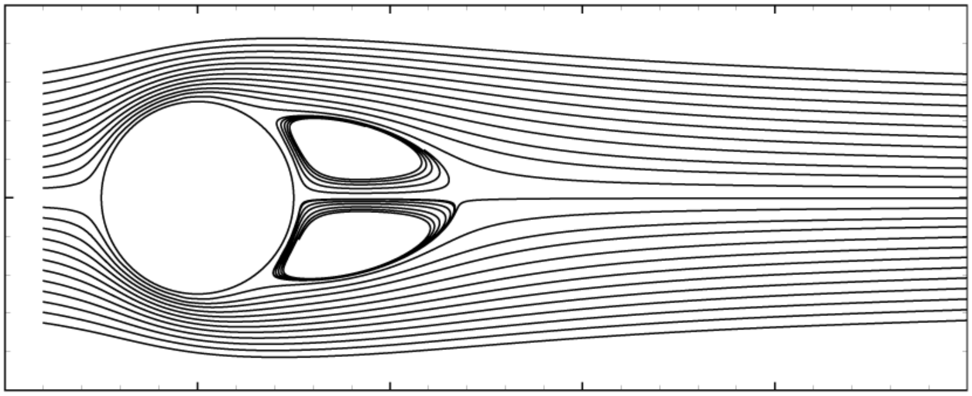

(b) $Re = 100$

Figure **8.55** Comparison of streamlines between two Reynolds numbers.

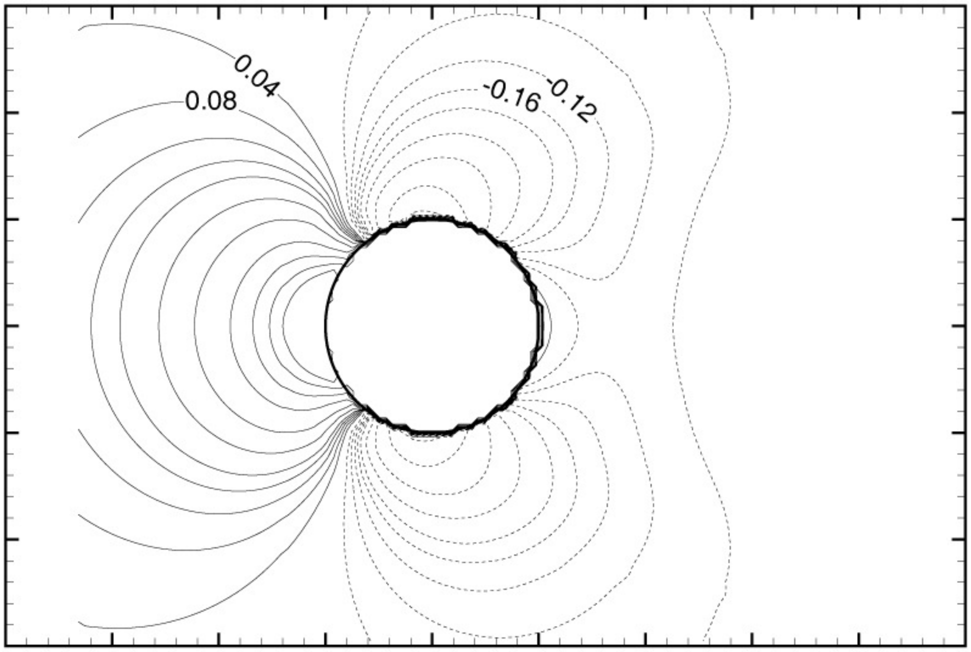

(a) $Re = 50$

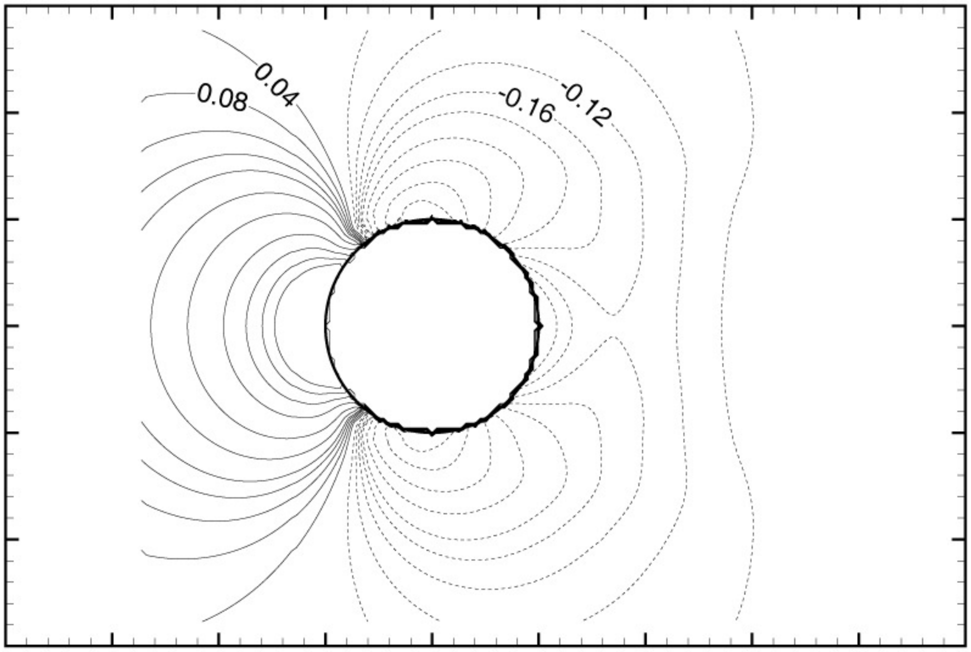

(b) $Re = 100$

Figure 8.56 Comparison of pressure coefficient contours between two Reynolds numbers.

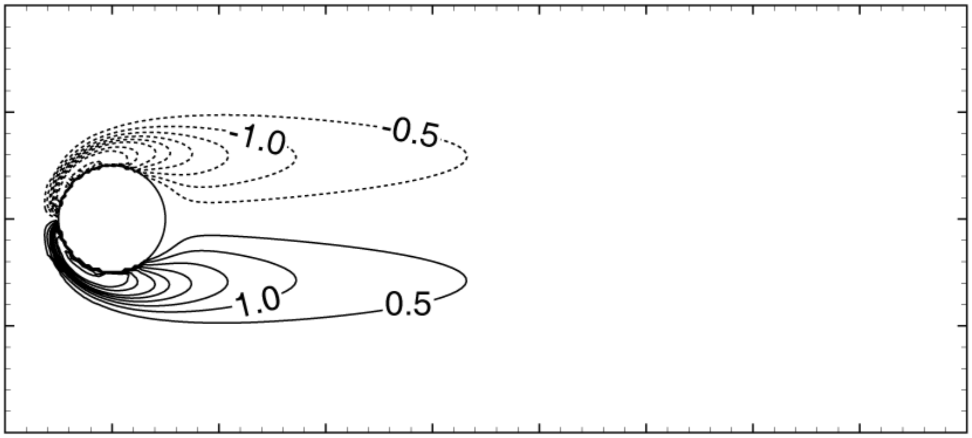

(a) $Re = 50$

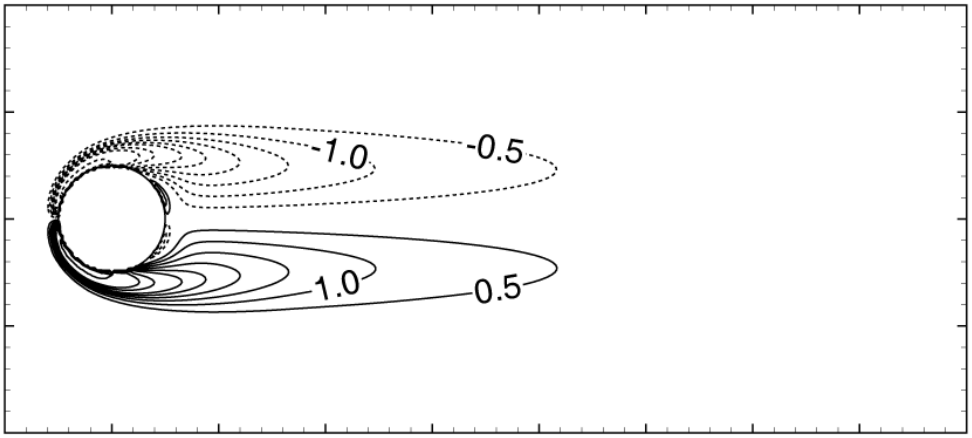

(b) $Re = 100$

Figure 8.57 Comparison of vorticity contours between two Reynolds numbers.

8.5.2.2 Rectangular wing

The present method is finally demonstrated on the flow past a three dimensional wing of rectangular planform. The NACA0012 section profile is employed for the illustration of the method. Figure 8.58 shows discretization of the rectangular wing. The ratio of span to chord is 1:1 for the figure. The panels on the side surfaces are constructed in the fully unstructured manner, where as the upper and lower surfaces of the wing have regular shape of triangles. The surfaces are firstly discretized into square rectangles, then the respective rectangles are divided into two triangles.

The simulation is performed for the rectangular wing with aspect ratio of 2 at angle of attack $\alpha = 7°$. The Reynolds number is 100 based on the wing chord length. The time step for the simulation is $\Delta t = 0.012$. The streamtraces around the tip and the pressure coefficient in the center plane of the wing are compared with the FLUENT results in Figure **8.59** . A stream trace starting below of the pressure side turns around the wing side, and forms into swirling flow downstream of the wing. It is clearly seen that the four stream traces are turning around each other by the tip vortex formation. It is seen from the pressure field in the center plane that the stagnation point is constituted near the leading edge of the wing. The pressure drop on the suction side is also illustrated in the figure.

Figure **8.60** shows the streamwise component of the vorticity, ω_x at several sreamwise planes, $x = 0.67, 0.8, 1.0$. The trailng edge is positioned at $x = 0.5$ when the angle of attack is zero. Figure **8.61** shows the tip vortex core position at the same streamwise planes plotted in Figure **8.60** . The coordinates of the core are extracted from the figure in such a manner that ω_x has a maximum value in each plane. The tip vortex core moves downward vertically and inside horizontally.

8.5.3 Features of vortex-in-cell method

An algorithm of VIC and panel method combination is developed and applied to the simulation of the viscous flow around impulsively started 2-D and 3-D objects. The main features of the present method are summarized as follows:

- The convection velocity of the vortex particles is efficiently computed on a regular Cartesian grid using an FFT based Poisson solver. The boundary of the grid compactly encloses the particles so as to reduce the domain size of the computation.
- The boundary conditions are enforced on the surface of the body for the tangential and normal components of the velocity. The tangential component of the slip is cancelled by the diffusion of vortex sheet, and the normal component is suppressed by the singularity which is linearly distributed

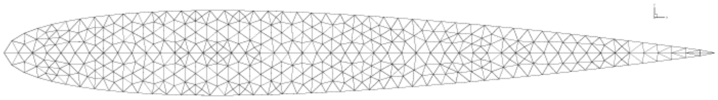

(a) Wing side discretization

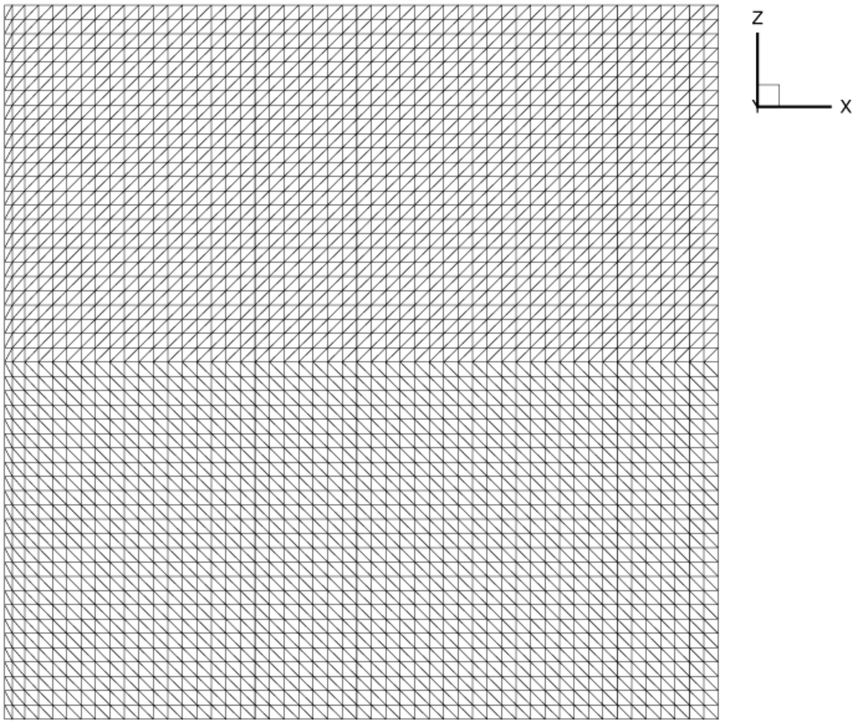

(b) Wing upper and lower surface discretization

Figure 8.58 Surface panel discretization of a rectangular wing. Number of the panels is 11,416.

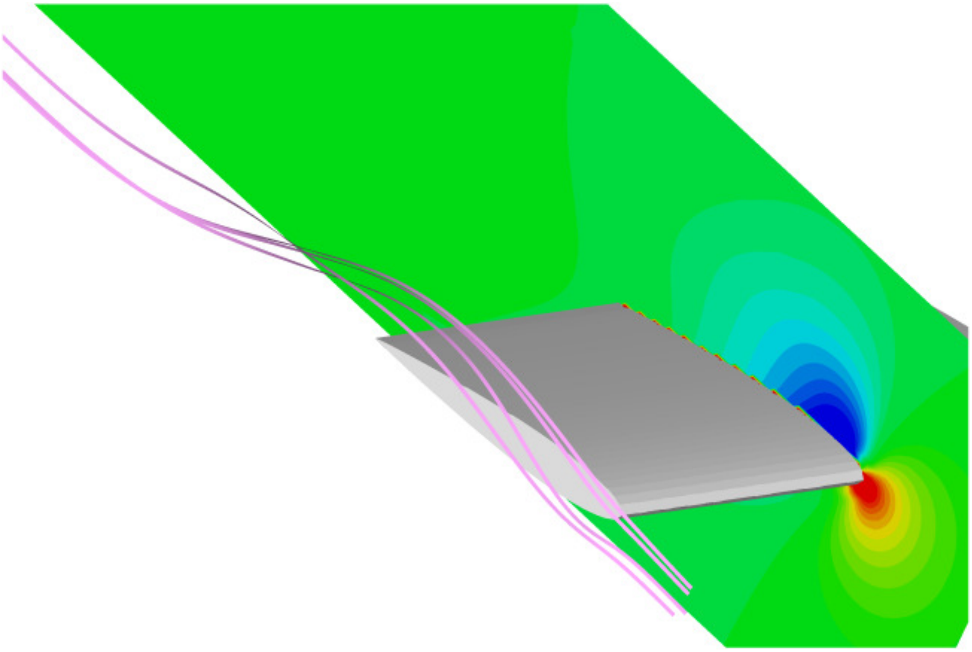

(a) Streamtraces and pressure coefficient, the present method

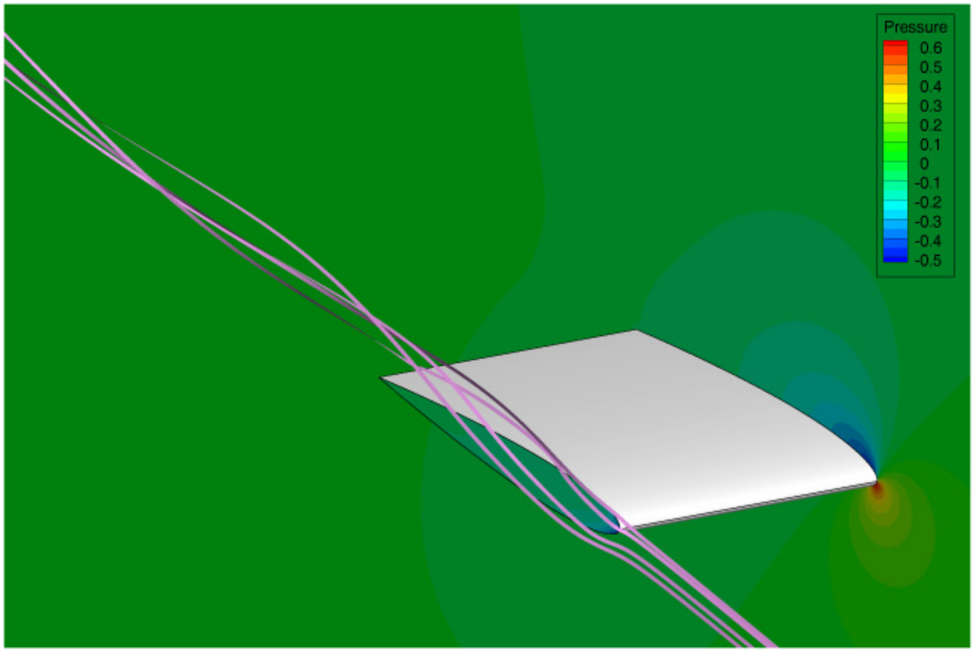

(b) Streamtraces and pressure coefficient, FLUENT

Figure 8.59 Comparison of streamtraces and pressure coefficient for a rectangular wing for $Re = 100$ with the results obtained by FLUENT.

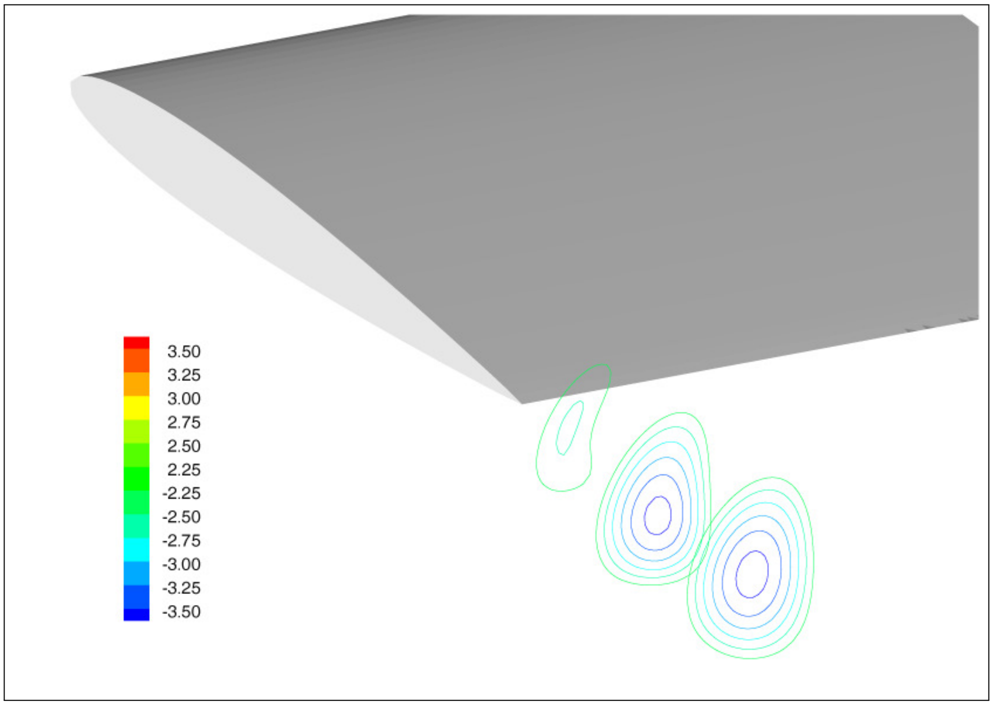

Figure 8.60 Streamwise vorticity contours at downstream locations $x = 0.67, 0.8$, and 1.0 at $t = 1.92$.

over a panel on the body. The use of panel method makes it possible for the application points of the two components of the boundary conditions to coincide on the center of the panel.

- The particle strength exchange (PSE) is modified to include the particles positioned inside of the body in the spirit of the immersed boundary nature of the method. The spurious slip resulting from the symmetric treatment near the body is corrected in the wall diffusion step for the no slip condition.

- The calculation of the pressure field is designed to use the solution method of integral equation approach, which is the same as the singularity distribution method for the no through flow condition. The matrix elements constructed and inverted once in the early stage of the method can be used throughout the method.

- The applicability of the present scheme is illustrated on the flow past 2-D and 3-D bodies in impulsive start. The method is in good agreement with other vortex method computation or the experimental work.

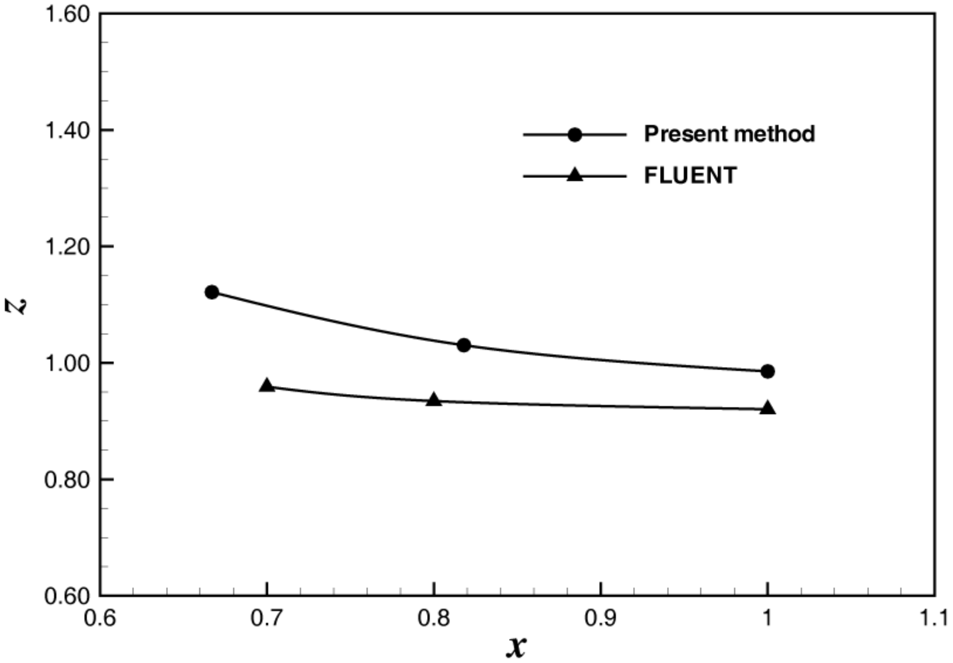

(a) Spanwise location of the center

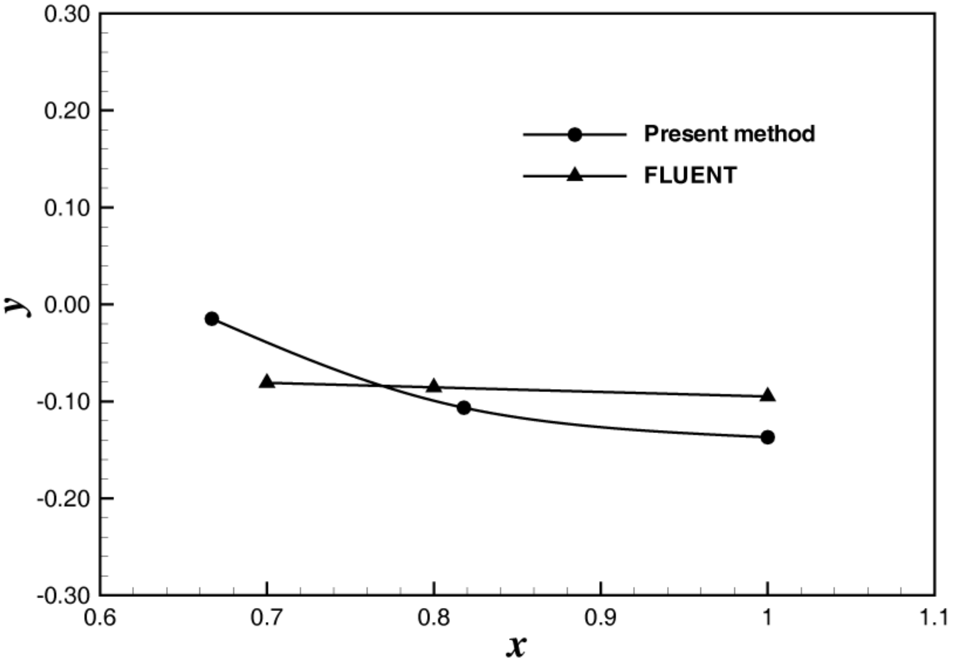

(b) Vertical location of the center

Figure 8.61 Location of the tip vortex center along downstream.

The proposed method is regarded as one possible solution of overcoming the leakage problem across a body boundary in the Cottet & Poncet (2003)'s method by the combination of vortex in cell method with a panel method. The panel method is formulated on the discretized surface panel in orde not to generate through flow component. This approach has an advantage in the computation of surface pressure as well as pressure field. The linear system of equations, constituted in the course of making normal boundary condition to be satisfied, can be applicable to the pressure calculation with the only change in the right hand side of the system.

8.6 Concluding Remarks

This course presents a vorticity-based integro-differential formulation for the numerical solution of unsteady incompressible flows. The integral approach that is a fundamental part of the present formulation is directly applicable for solving the integral equation for the pressure field as well. The present scheme includes a pressure calculation which is a distinctive feature, not previously treated in most vorticity-based methods. These aspects have been adapted for the vorticity-velocity-pressure formulation by an Eulerian description.

For the kinematics of flow and the physical interpretation of the velocity field ($\underline{q} = \underline{u}_w + \nabla\phi + \underline{U}_\infty$), a Lagrangian vortex method connected with the panel method has been presented. An iterative process was used in order to enforce the no-slip condition through the vorticity flux at the body boundary. For a thin body, we suggest the use of an image particle layer for the zero-vorticity flux condition on the solid boundary.

By applying the present scheme for the impulsively-started cylinder and the impulsively-started NACA0021 foil with angles of attack, we performed comparisons with existing results, and with the results of an Eulerian FVM.

Although the present work has mainly focused on comparative studies, future work would address (i) the treatment of turbulence models, (ii) the extension of the vortex method to three-dimensional flow problems, and (iii) the development of efficient numerical schemes associated with the solution procedure.

8.6.1 LES in vortex methods

The direct numerical simulation of turbulent flows is possible for low Reynolds number. Number of elements required for large Reynolds number of practical application is very large so that the actual simulation is restricted. With the current computer resource, the large eddy simulation is possible in which we take modeling for the small-scale (subgrid-scale) turbulence in the viscous wake and in the boundary layers.

The vortex method has been thought of as a natural approach to the simulation of turbulent flows. The use of vortex particles that convect with the flow in a Lagrangian manner has been considered as a way of minimizing numerical diffusion, which is an important matter in turbulent flow solution. The discretization of the vorticity field using a smoothing function

$$\underline{\omega}(\underline{x},t) = \sum_{i=1}^{N} \zeta_\epsilon(\underline{x}-\underline{x}_i)\,\underline{\alpha}_i \tag{8.94}$$

can be considered to be some kind of filtering (normally, particle filtering) operation in LES. The filtered voriticity transport equation

$$\frac{D\overline{\underline{\omega}}}{Dt} = \overline{\underline{\omega}}\cdot\nabla\overline{\underline{u}} + \nu\,\nabla^2\overline{\underline{\omega}} - \nabla\cdot\underline{\underline{T}} \tag{8.95}$$

differs from the laminar version in that vorticity stress term $\nabla\cdot\underline{\underline{T}}$ is added, where $T_{ij} = (\overline{\omega_i\,u_j} - \overline{\omega}_i\,\overline{u}_j) - (\overline{u_i\,\omega_j} - \overline{u}_i\,\overline{\omega}_j)$ is the subfilter scale vorticity stress.

If we take the vorticity version of the Smagorinsky model for that term, $-\nabla\cdot\underline{\underline{T}} = \nabla\cdot(\nu_t\,\nabla\overline{\underline{\omega}})$, the turbulent diffusion can be treated in a similar way to the particle strength exchange of the laminar diffusion. Cottet (1999) suggested a simple selective model that the eddy diffusivity ν_t comes into action in region of intense vortex activity, where the flow is strongly three dimensional.

$$\nu_t = \begin{cases} C_s^2\,\Delta^2\,|\overline{\underline{\omega}}|, & \text{for} \quad \beta_0 < \beta_m < \pi - \beta_0 \\ 0, & \text{otherwise} \end{cases} \tag{8.96}$$

The region of nonzero eddy diffusivity is where the angle β_m between the vorticity at a given grid point and the average neighboring vorticity becomes antialigned. The turbulent diffusion then becomes particle strength exchange with average eddy diffusivity,

$$\nabla \cdot (\nu_t \nabla \underline{\overline{\omega}}) = \frac{1}{2\,\epsilon^2} \sum_j (\nu_{t_i} + \nu_{t_j})\,(\underline{\alpha}_j - \underline{\alpha}_i)\,\eta_\epsilon(\underline{x}_i - \underline{x}_j) \tag{8.97}$$

The extension of the VIC algorithm developed in this work to the turbulent flow analysis is expected to be realized in future work.

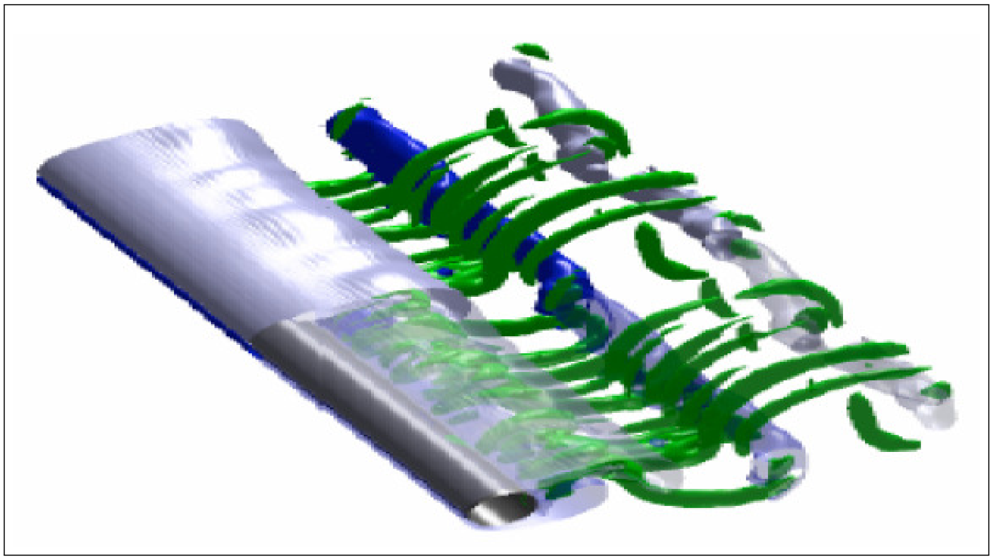

Figure 8.62 Turbulent flow past a cylinder by VIC method. Cylindrical grid: $256 \times 128 \times 128$ in a domain $4\pi \times 2\pi \times 2\pi$ filled with 25 % particles; CPU time: 8 min/RK4 iteration on alpha single processor, 3 hours/shedding cycle. From Cottet & Poncet (2003).

8.6.2 Interaction between flow and bubble

The vorticity transport equation for two-dimensional incompressible flow of a viscous fluid can be rewritten, without ignoring the external force, as

$$\frac{D\underline{\omega}}{Dt} = \nu\,\nabla^2 \underline{\omega} + \nabla \times \underline{f} \tag{8.98}$$

where $\underline{f}$ is the external force caused by all the bubbles in fluid. The external force is accounted for here the total force $\underline{f}_B$ acting on the bubble; $\underline{f} = -\underline{f}_B$.

Equation of motion for a single bubble yields the following trajectory equation for a bubble of changing volume:

$$\begin{aligned} m_B \frac{d\underline{u}_B}{dt} &= \rho V_B \frac{D\underline{u}}{Dt} - \frac{1}{2}\rho V_B \left(\frac{d\underline{u}_B}{dt} - \frac{D\underline{u}}{Dt} \right) + \frac{1}{2}\rho\,(\underline{u} - \underline{u}_B)\,\frac{dV_B}{dt} \\ &\quad + \frac{1}{2}\rho\,\pi\,R^2\,C_D\,|\underline{u} - \underline{u}_B|\,(\underline{u} - \underline{u}_B) \end{aligned} \tag{8.99}$$

where the forces with the gravitational acceleration are neglected in this study; the gravity and the buoyant force.

Recall that the force acting on the bubble is

$$\underline{f}_B = \underline{F}_U + \underline{F}_M + \underline{F}_V + \underline{F}_D \tag{8.100}$$

where

$\underline{F}_U$ = Unsteady force due to the acceleration of the undisturbed flow
$\underline{F}_M$ = Convential added mass force
$\underline{F}_V$ = Additional added mass force due to the volume variation
$\underline{F}_D$ = Drag force

The hydrostatic forces, *i.e.* the bouyancy and graivity force, are accounted for without directly producing any disturbace. Because the forces that are included Du/Dt term are not produced by the bubble motion, they must be negligible. Hence, Equation (8.99) is rewritten as

$$\rho V_B \frac{d\underline{u}_B}{dt} = \rho\,(\underline{u} - \underline{u}_B)\,\frac{dV_B}{dt} + \rho\,\pi\,R^2\,C_D\,|\underline{u} - \underline{u}_B|\,(\underline{u} - \underline{u}_B) \tag{8.101}$$

where ρ_B is neglected due to $\rho_B \ll \rho$. With the drag force $\underline{F}_D$ and the additional added mass force $\underline{F}_V$ due to volume variation, (8.101) accounted for the force acting on the fluid element which occupies the same volume and velocity of the bubble. These external forces can be considered as the disturbance exerted by the motion of the bubble.

Suppose now that the disturbance is separated into two parts, the disturbance induced by the translational motion of the bubble and the distubance induced

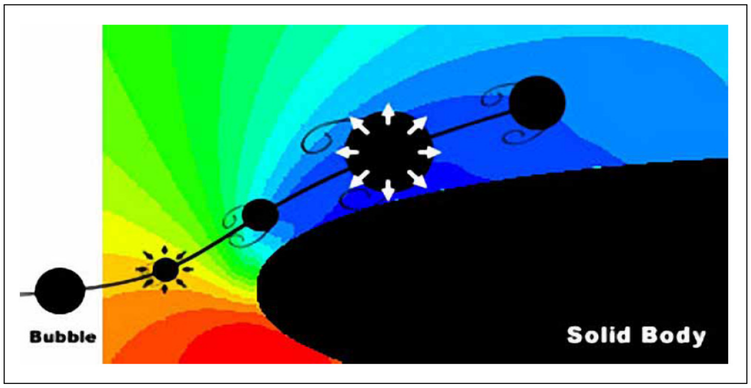

Figure **8.63** Schematic diagram of interaction between the motion of a single bubble and the ambient viscous flow.

by the volumetric motion as shown in Figure **8.63** .

$$\underline{f} = \underline{F}_V + \underline{F}_D \tag{8.102}$$

8.6.2.1 Disturbance by volumetric motion

The disturbance which is induced by the *pure* volumetric motion of the bubble, can be considered as mass source/sink in flow according to Eq. (8.101). According to *Lagally Theorem*, that is, the force on the bubble is proportional to the source strength and to the magnitude of the velocity $(\underline{u} - \underline{u}_B)$ induced at the location of the source by all mechanisms other than the source itself. The direction of the force coincides with that of the relative velocity vector. Thus, the force which is the volumetric motion of the bubble is defined as

$$\underline{F}_V = \rho\,(\underline{u} - \underline{u}_B)\,\frac{dV_B}{dt} = \rho\,\mathcal{Q}\,(\underline{u} - \underline{u}_B) \tag{8.103}$$

The strength of the mass source/sink becomes

$$\mathcal{Q} = \frac{dV_B}{dt} = 4\pi R^2 \dot{R} \tag{8.104}$$

Recall that the velocity potential ϕ is used to enforce the no-through-flow boundary condition,

$$\underline{u}' = U_\infty + \underline{u}_\omega + \nabla\phi \tag{8.105}$$

and that the velocity potential for the pure radial motion of the bubble is defined by

$$\phi_B \;=\; -\frac{1}{4\pi}\frac{Q}{r} \;=\; -\frac{R^2\dot{R}}{r} \tag{8.106}$$

Hence, with the velocity induced by the radial motion of the bubble, the flow velocity is rewritten as

$$\underline{u}'' \;=\; U_\infty \;+\; \underline{u}_\omega \;+\; \nabla\phi \;+\; \nabla\phi_B \tag{8.107}$$

where

$$\nabla\phi_B \;=\; \frac{R^2\dot{R}}{r^2}\,\underline{e}_r \tag{8.108}$$

The symbol $\underline{e}_r$ denotes the unit vector in the outward radial direction from the bubble.

Owing to the no-through-flow boundary condition, the normal component of the velocity on the body surface becomes zero as

$$\underline{n}\cdot\underline{u}'' \;=\; \underline{n}\cdot\left(U_\infty \;+\; \underline{u}_\omega \;+\; \nabla\phi \;+\; \nabla\phi_B\right) \;=\; 0 \tag{8.109}$$

Then, substituting Eqn. (8.109) into Eqn. (4.2), it is found that

$$\frac{1}{2}\phi - \oint_C \phi\left(\underline{n}\cdot\nabla G\right)\,d\ell \;=\; -\oint_C \left(\underline{n}\cdot\left(U_\infty + \underline{u}_\omega + \nabla\phi_B\right)\right) G\,d\ell \tag{8.110}$$

The velocity potential on the body surface is implicitly computed. The velocity at the field is adjusted by the velocity potential obatained by the above equation.

8.6.2.2 Disturbance by translational motion

Previous to computing the disturbance induced by the pure translational motion of the bubble, consider the definition of the hydrodynamic force $\underline{F}$ with the hydrodynamic impluse $\underline{I}$ (Lamb 1932, Saffman 1992); thus,

$$\underline{F} \;=\; -\rho\,\frac{\Delta\underline{I}}{\Delta t} \tag{8.111}$$

In two-dimensional case, the components of the hydrodynamic impluse (I_x, I_y) are defined as

$$I_x = \sum y_i \, \Gamma_i \,, \qquad I_y = -\sum x_i \, \Gamma_i \tag{8.112}$$

and then the components of the force (F_x, F_y) are

$$F_x = -\rho \frac{\Delta I_x}{\Delta t} \,, \qquad F_y = -\rho \frac{\Delta I_y}{\Delta t} \tag{8.113}$$

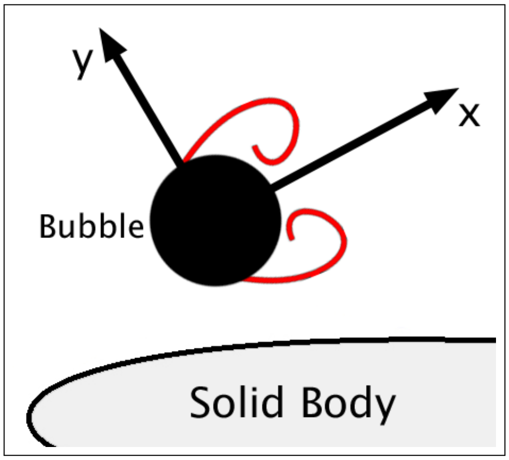

Figure **8.64** Local coordinates for the hydrodynamic impulse of the bubble

Also, the drag force $\underline{F}_D$ acting on a sphere in creeping flow at very low Reynolds numbers is defined as (Batchelor 1973)

$$\underline{F}_D \;=\; -\,\rho \frac{\Delta I_x}{\Delta t} \;=\; 12\,\pi \mu R \,(\underline{u} - \underline{u}_B) \tag{8.114}$$

or equivalently

$$\Delta I_x \;=\; -\,12\,\pi \nu R \,(\underline{u} - \underline{u}_B)\,\Delta t \tag{8.115}$$

From these definitions, it is considered that the vorticity generated by the translational motion of the bubble, which is exerted by the only drag force (the effect exerted by the lift force is neglected in this study). Then, it can be modeled that a symmetrical pair of two-dimensional vorticity of finite size on the bubble surface is generated monotonically during Δt.

$$y_{up}\,\Gamma_{up} \;+\; y_{dn}\,\Gamma_{dn} \;=\; -\,12\,\pi\,\nu\,R\,(\underline{u} - \underline{u}_B)\,\Delta t \tag{8.116}$$

The vorticity strength is obtained as $|\Gamma| = 6\pi\nu\,|\underline{u} - \underline{u}_B|\,\Delta t$ at $|y| = R$. The magnitude of the induced vorticity is rewritten with with non-dimensional value as

$$|\Gamma^*| = \frac{6\pi}{Re}\,|\underline{u}^* - \underline{u}_B^*|\,\Delta t^* \tag{8.117}$$

with Reynolds number $Re = U_\infty L/\nu$ for the flow. The vorticity induced by the bubble (Figure **8.65**) is computed by differentiating directly over the Lagrangian control points, without requiring the interpolation onto the grid. In fact, the actual vortices shedding behind a sphere would be of ring type. Therefore an axisymmetric ring vortex model equivalent to the drag forces is more realistic than the present model taken herein. Such a three dimensional numeric modelling is beyond of the present workscope, even through there still exists inconsistency on the bubble interactions, in the respect of overall two dimensional analysis.

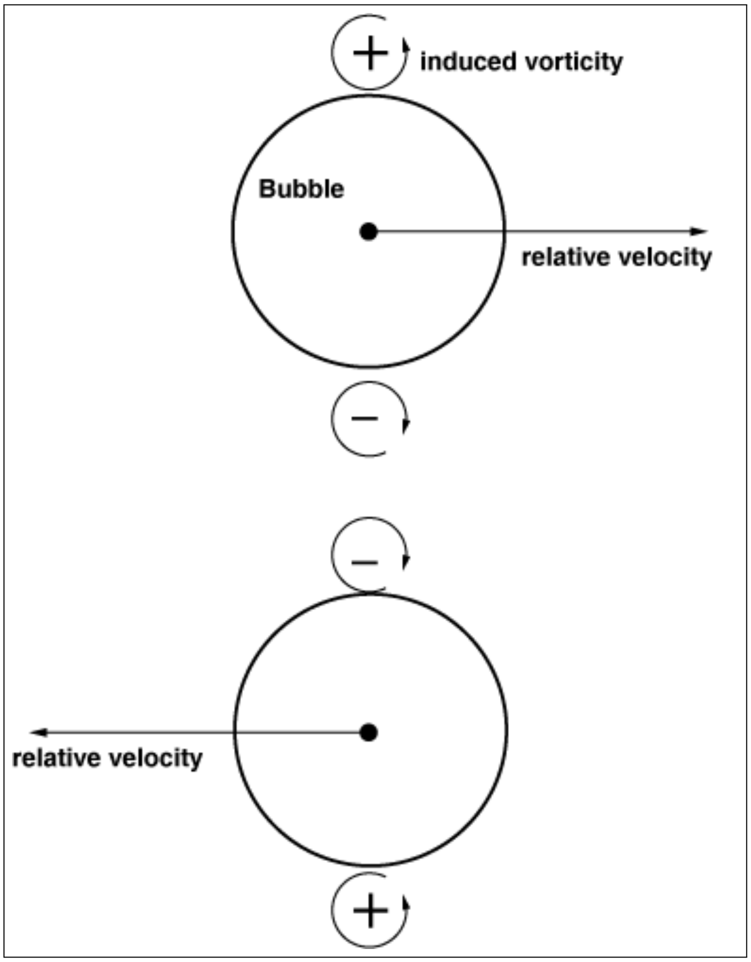

Figure **8.65** Schematic of the vorticity generation

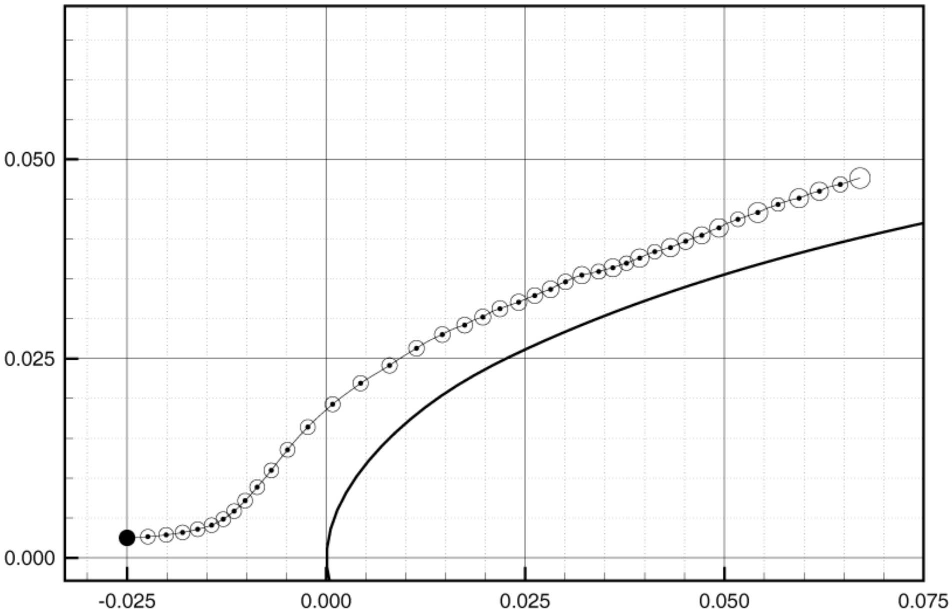

(a) Cavitation number $C_a = 1.0$

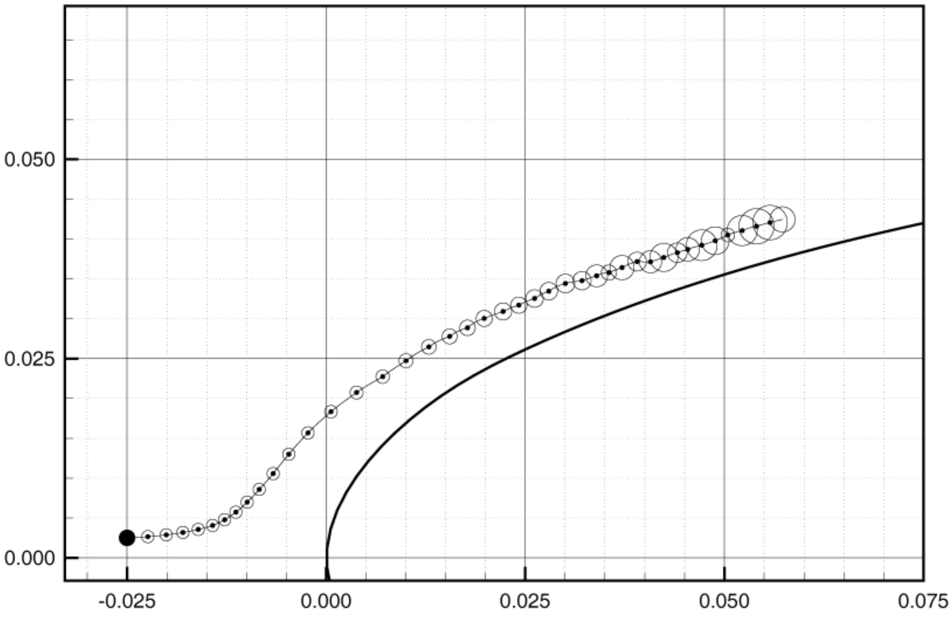

(b) Cavitation number $C_a = 0.1$

Figure 8.66 Bubble behavior for two different cavitation numbers. Initial bubble radius $R_o = 1,000\mu m$